Universität Hamburg
Department Physik

Spurious Dispersion Effects at FLASH

Dissertation
zur Erlangung des Doktorgrades
des Department Physik
der Universität Hamburg

vorgelegt von
Eduard Prat
aus Figueres (Catalunya)

Hamburg
2009

Gutachter der Dissertation:	Prof. Dr. Jörg Roßbach Prof. Dr. Shaukat Khan
Gutachter der Disputation:	Prof. Dr. Jörg Roßbach Prof. Dr. Peter Schmüser
Datum der Disputation:	16. Juli 2009
Vorsitzender des Prüfungsausschusses:	Dr. Georg Steinbrück
Vorsitzender des Promotionsausschusses:	Prof. Dr. Robert Klanner
Dekan der Fakultät für Mathematik, Informatik und Naturwissenschaften:	Prof. Dr. Heinrich H. Graener

Abstract

The performance of the Free-Electron Laser (FEL) process imposes stringent demands on the transverse trajectory and size of the electron beam. Since transverse dispersion changes off-energy particle trajectories and increases the effective beam size, dispersion must be controlled.

This thesis treats the concept of dispersion in linacs, and analyses the impact of dispersion on the electron beam and on the FEL process. It presents generation mechanisms for spurious dispersion, quantifying its importance for FLASH (Free-electron Laser in Hamburg) and the XFEL (European X-ray Free-Electron Laser). A method for measuring and correcting dispersion and its implementation in FLASH is described. Experiments of dispersion effects on the transverse beam quality and on the FEL performance are presented.

Zusammenfassung

Der Freie-Elektronen-Lasers (FEL) Prozess stellt strenge Anforderungen an die transversale Trajektorie und Größe des Elektronenstrahls. Da die transversale Dispersion die Trajektorie der Teilchen mit Impulsabweichung verändert und die effektive Strahlgröße erhöht, muss die Dispersion kontrolliert werden.

Diese Doktorarbeit behandelt das Konzept der Dispersion in Linearbeschleunigern (linacs), und untersucht den Einfluss dispersiver Effekte auf den Elektronenstrahl und den FEL-Prozess. Sie bennent Ursachen Quellen für Störddispersion und quantifiziert ihre Bedeutung für FLASH (Freie-Elektronen-Laser in Hamburg) und den XFEL (Europäische Röntgenlicht-Freie-Elektronen-Laser). Eine Methode für die Messung und Korrektur der Dispersion und ihr Einsatz bei FLASH werden beschrieben. Experimente über den Effekt der Dispersion auf die transversale Qualität des Strahls und auf die Leistung des FELs werden vorgestellt.

Contents

1 Introduction **1**

2 Free-Electron Lasers **3**
2.1 From Synchrotron Radiation to FEL 3
2.2 FEL Characterization 5
2.2.1 Increase of Gain Length by 3D Effects 8
2.2.2 Numerical Estimation of 3D-effects 8
2.3 FLASH 9
2.4 XFEL 11

3 Dispersion in Linacs **13**
3.1 Single Particle Beam Transport 13
3.1.1 Matrix Formalism 13
3.1.2 Dispersion Functions 15
3.1.3 Beam Offsets and Angles 15
3.2 Effects on the Electron Beam Distribution 17
3.2.1 Statistical Effects 18
3.3 Effects on the FEL Process 21

4 Dispersion Generation Mechanisms **23**
4.1 Dispersion in Single Elements 23
4.1.1 Dispersion in Dipole Magnets 23
4.1.2 Dispersion in Quadrupole Magnets 24
4.1.3 Dispersion in RF Accelerator Cavities 25
4.1.4 Dispersion in Sextupoles and Higher Multipole Magnets 25
4.2 Dispersive Sections at FELs 26
4.2.1 Bunch Compressors 26
4.2.2 Collimator Sections 26
4.2.3 Design Dispersion at FLASH and the XFEL 27
4.3 Spurious Dispersion Sources 30
4.3.1 Dipole Field Errors 30
4.3.2 Trajectory Errors 31
4.3.3 Element Misalignments 31

4.3.4 Quadrupole and Sextupole Field Errors at Dispersive Sections . . . 32
4.3.5 Other Sources . . . 33
4.3.6 Dispersion Propagation . . . 33
4.4 Sensitivities for FLASH and the XFEL . . . 33

5 Dispersion Measurement and Correction 37
5.1 Dispersion Measurement . . . 37
5.1.1 RF Steering Compensation . . . 38
5.1.2 Dispersion Derivation . . . 39
5.1.3 Dispersion Measurement Errors . . . 40
5.1.4 Examples of Measurements at FLASH . . . 42
5.2 Dispersion Correction Algorithm . . . 44
5.3 Dispersion Tool at FLASH . . . 46
5.3.1 Example of Simulations . . . 47
5.3.2 Examples of Measurements . . . 47

6 Transverse Beam Quality at FLASH 51
6.1 Introduction . . . 51
6.2 Beam Size and Emittance Measurements at FLASH . . . 52
6.2.1 Transverse Beam Diagnostics . . . 52
6.2.2 Emittance Calculation . . . 53
6.2.3 Optics Matching . . . 54
6.2.4 Saturation of Photomultipliers in the Undulator . . . 55
6.3 Beam Tilt at the First Bunch Compressor . . . 57
6.3.1 Measurements . . . 57
6.3.2 Simulations . . . 61
6.3.3 Discussion . . . 64
6.4 Dispersion Effects in the Undulator . . . 65
6.4.1 Dispersion Generation . . . 65
6.4.2 Dispersion Correction . . . 67
6.5 Electromagnetic Fields in TESLA Modules . . . 68
6.5.1 Coupler Kicks . . . 68
6.5.2 Transverse Wakefields . . . 70
6.5.3 Modeling in *elegant* . . . 72
6.5.4 Impact of Orbit Bumps Through TESLA modules . . . 73
6.6 Conclusion . . . 74

7 Dispersion Effects on FEL Performance at FLASH 77
7.1 FEL Simulations with *Genesis 1.3* . . . 77
7.2 SASE Sensitivity to Transverse Trajectory . . . 78
7.3 SASE Sensitivity to Electron Energy Offset . . . 80
7.3.1 Measurements . . . 80
7.3.2 Simulations . . . 82

7.4 Dispersion Impact on the SASE Spectrum 85
7.4.1 Simulations with a Gaussian Electron Beam 86
7.4.2 Measurements 89
7.5 Conclusion 93

8 Conclusion **95**

A C-shape at the First Bunch Compressor of FLASH **97**
A.1 Effects of ACC1 phase 99
A.2 A Possible Explanation: A Horizontal Solenoid Misalignment 100
A.3 Conclusion 101

B Second-Order Dispersion Terms for a Dipole Magnet **103**

C Orbit and Dispersion Tool at FLASH **105**
C.1 User Interface 105
C.1.1 Input Data 105
C.1.2 Action Buttons 109
C.1.3 Output Results 110
C.1.4 Other Available Options 110
C.2 ODCA 111

List of Tables

2.1 Main parameters of FLASH and the XFEL. 12

4.1 Required amount of error per type and section to generate 10 mm of dispersion in the FLASH undulator. 34
4.2 Required amount of error per type and section to generate 10 mm of dispersion in the XFEL undulator. 35

6.1 Amplitude at BPM9ACC1 for all the bumps for the beam tilt experiment. 58
6.2 Results of projected emittance measurements at FLASH. . . 76

7.1 Summary of measurements on SASE energy sensitivity to relative electron energy offset. 82
7.2 Dispersion impact on the wavelength spectrum for different initial transverse offsets. 89

List of Figures

1.1 Overview of the peak brilliances for different synchrotron light sources 2

2.1 Schematic view of a planar hybrid undulator magnet 4
2.2 Radiation pulse energy growth and schematic microbunching as a function of the undulator length for an FEL 6
2.3 Pierce parameter and 1D gain length for design FLASH parameters as a function of the electron energy 7
2.4 1D and 3D gain length for FLASH design parameters 9
2.5 Schematic layout of FLASH 10
2.6 Schematic layout of the XFEL 11

3.1 Coordinates system used to described particle trajectories . . 14
3.2 Horizontal dispersion for two different initial positions 16
3.3 Simulation results and a measurement of the c-shape effect at FLASH 18
3.4 Example of beam size and emittance increase due to dispersion as a function of the relative momentum deviation 20
3.5 Example of dispersion effects on the beam distribution 21
3.6 Increase of the gain length as a function of dispersion for FLASH design parameters 22

4.1 Design trajectory and dispersion in the bunch compressors of FLASH 27
4.2 Design dispersion at the collimator section of FLASH 28
4.3 Design dispersion along FLASH 28
4.4 Design dispersion along the XFEL 29
4.5 Trajectory and dispersion through a bunch compressor in which the last bending magnet has a field error 30
4.6 Trajectory and dispersion generation of a horizontally misaligned quadrupole 31
4.7 Dispersion at the FLASH collimator with quadrupole and sextupole field errors 32

5.1 Schematic view of FLASH 37
5.2 Sketch of the RF steering correction 38
5.3 Example of a dispersion measurement at a single BPM 39
5.4 Dispersion uncertainties as a function of trajectory uncertainties 41
5.5 Dispersion measurement from ACC1 - Day 1 43
5.6 Dispersion measurement from ACC1 - Day 2 43
5.7 Horizontal dispersion response matrix for 1 GeV at FLASH . 45
5.8 Scheme for dispersion correction procedure 47
5.9 Example of simulated horizontal dispersion correction at FLASH (from ACC1) 48
5.10 Example of a horizontal dispersion correction at FLASH (from ACC1) 49
5.11 Example of a vertical dispersion correction at FLASH (from ACC456) 49

6.1 Locations of OTR monitors, wirescanners (WS), and dedicated areas for emittance measurements at FLASH. 52
6.2 Sketch of the undulator section of FLASH 53
6.3 Beam size measurements at the wirescanner 5UND4 with and without attenuation filters 56
6.4 Example of beam with an x-y tilt 57
6.5 Sketch of the beam tilt experiment 58
6.6 Dispersion measurements for the beam tilt experiment 59
6.7 Measured beam tilts for the beam tilt experiment 60
6.8 Measured emittances for the beam tilt experiment 60
6.9 Simulated and measured orbit differences for the beam tilt experiment 62
6.10 Simulated and measured dispersions for the beam tilt experiment 62
6.11 Simulated and measured beam tilts for the beam tilt experiment 63
6.12 Simulated and measured vertical emittance increases for the beam tilt experiment 63
6.13 Simulated and measured images for the beam tilt experiment 64
6.14 Measured and simulated horizontal dispersion in the undulator for the dispersion generation experiment 65
6.15 Measured and simulated beam profiles at the wirescanner 5UND6 for the dispersion generation experiment 66
6.16 Horizontal dispersion in the undulator before and after dispersion correction 67
6.17 Beam profile measurement at wirescanner 5UND2 before and after dispersion correction 68
6.18 Overview of a TESLA 9-cell RF cavity 69
6.19 Induced electric-field map for the coupler regions of a TESLA cavity 70

6.20 Comparison between transverse kicks generated by structure and coupler wakefields 72
6.21 Sketch of the experiment on the impact of horizontal bumps through ACC23 73
6.22 Measurements and simulations of emittance increase for different bumps through ACC23 74

7.1 Electron beam properties at the undulator entrance 78
7.2 Sketch of the experiment on SASE sensitivity to electron trajectory 79
7.3 Measurements and simulations of SASE sensitivity to the incoming trajectory 79
7.4 Measured dispersion in the undulator for the different conditions of the experiment on SASE sensitivity to electron energy offset 81
7.5 Measured SASE energy as a function of electron energy offset for the different conditions of the experiment on SASE sensitivity to electron energy offset 82
7.6 Measured and reconstructed dispersion along the undulator before and after correction for the experiment on SASE sensitivity to electron energy offset 84
7.7 Measurements and simulations of SASE energy as a function of electron energy offset before and after dispersion correction 84
7.8 Energy and current distribution along the bunch of the electron slices which produce FEL radiation 85
7.9 Dispersion effects on the wavelength spectrum for an initial zero offset along the bunch 87
7.10 Dispersion effects on the wavelength spectrum for an initial offset of 100 µm along the bunch 87
7.11 Dispersion effects on the wavelength spectrum for an initial offset of 250 µm along the bunch 87
7.12 Dispersion effects on the wavelength spectrum for an initial linear *x-energy* correlation 88
7.13 Dispersion effects on the wavelength spectrum for an initial quadratic *x-energy* correlation 89
7.14 Radiation spectrum measurements for different dispersion scenarios 90
7.15 Trajectory offset and angle along the longitudinal position of the bunch for the different dispersion conditions at the entrance of the undulator 91
7.16 Measurements and simulations of dispersion effects to the radiation wavelength spectrum 92

A.1 Simulated and measured c-shaped beam 97

A.2 Sketch of the simulations on the c-shape experiment 98
A.3 Simulated dispersion from ACC1 and from the GUN for the c-shape experiment 98
A.4 Simulations and measurements of the c-shape effect for different ACC1 phases 99
A.5 Measured effects on the c-shape of moving horizontally and vertically both iris and mirror positions 100
A.6 Measured effects on the c-shape of manipulating the vertical trajectory 101

C.1 Main GUI of the *Orbit and dispersion tool* 106
C.2 *Golden orbit and dispersion* GUI of the *Orbit and dispersion tool* 108
C.3 *RF settings* GUI of the *Orbit and dispersion tool* 109
C.4 *BPM details* GUI of the *Orbit and dispersion tool* 111
C.5 ODCA GUI 113

Chapter 1

Introduction

One of the major applications of accelerator facilities is the utilization of the synchrotron radiation, a powerful diagnostic tool used in different disciplines such as material science, biology, physics, chemistry, and medicine. Synchrotron radiation facilities offer a broad radiation spectrum, ranging from the infrared to the hard x-ray regime.

The figure of merit of many experiments and therefore used to compare different synchrotron light facilities is the *brilliance*[1] (or spectral brightness). As showed in Figure 1.1, the peak brilliance of Free-Electron Lasers (FELs) driven by linear accelerators (or linacs) like FLASH (Free-electron LASer in Hamburg) and the XFEL (European X-ray Free-Electron Laser) is several orders of magnitude higher than that of conventional synchrotron radiation facilities.

This thesis deals with dispersion effects at linac-based FEL facilities. Although most of the presented work has been done for FLASH, the results can be extrapolated to other facilities such as the XFEL. Chapter 2 characterizes the FEL process and presents FLASH and the XFEL.

Dispersion is the momentum dependence of the deflections exerted by a magnetic field to a charged particle. Inside a bunch of electrons, dispersion causes different trajectories for particles with different energies. As a consequence, the transverse space occupied by the beam increases. Chapter 3 characterizes the dispersion in linacs and introduces its effect on the distribution of electrons and on the FEL performance. Chapter 4 describes the potential dispersion sources which are generated by the elements of an accelerator lattice (i.e. magnets and accelerator cavities) and presents sensitivities studies for FLASH and the XFEL.

Dispersion needs to be controlled to avoid its negative impact to the

[1] The brilliance is defined as the number of photons emitted by the source per unit of time into a unit of solid angle, per unit of surface of the source, and into a unit bandwidth of frequencies around the given one ([photons/(sec·mrad^2·mm^2·0.1%bandwidth)]).

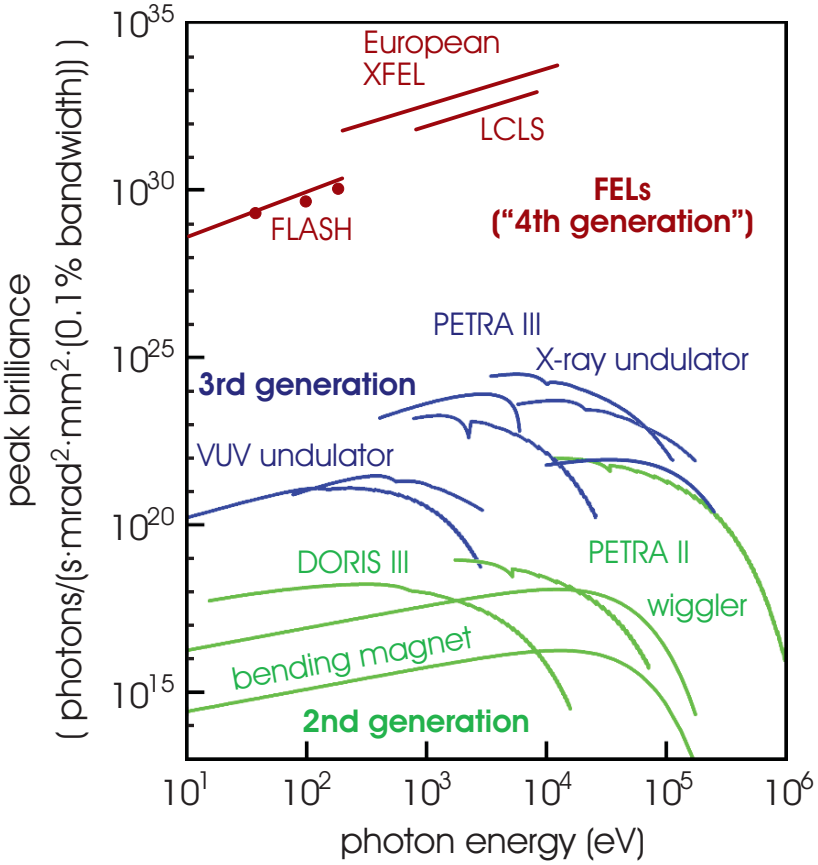

Figure 1.1: Overview of the peak brilliances for different synchrotron light sources. Brown spots show experimental performance of FLASH.

FEL process. A procedure to measure and correct dispersion and its implementation at FLASH are presented in Chapter 5.

The last two chapters are dedicated to studying the impact of the dispersion at FLASH. Chapter 6 is focused on analyzing how the dispersion deteriorates the transverse beam quality. Studies of the impact of the RF electromagnetic fields in TESLA modules, which also worsens the transverse beam quality, are also presented. Chapter 7 presents studies of the dispersion effect on the FEL performance.

Chapter 2

Free-Electron Lasers

2.1 From Synchrotron Radiation to FEL

In the 1960's some electron storage rings designed and built for nuclear and subnuclear physics started to be used parasitically as sources of photons for experiments in atomic, molecular and solid state physics. These machines are nowadays referred to as *first-generation* light sources.

Later, *second-generation* facilities were designed and optimized to serve exclusively as light sources using the synchrotron radiation emitted in bending magnets. Examples of these *second generation* machines are the BESSY I ring in Berlin (Germany), the two National Synchrotron Light Source rings in Brookhaven (New York, USA), the SuperACO ring in Orsay (France), and the Photon Factory in Tsulcuba (Japan).

In the 1990's *third-generation* light sources started to operate. These facilities were characterized by the reduction of the beam *emittance*[1] and by the extensive use of insertion devices (*wigglers* and *undulators*). These improvements provided more brilliant, quasi-monochromatic and tunable synchrotron radiation. Examples of this generation of sources are the European Synchrotron Radiation Facility (ESRF) in Grenoble (France), the Advanced Light Source in Berkeley (California, USA) , the Spring 8 in Japan, and the Swiss Light Source in Villigen (Switzerland).

An undulator is an array of magnets which produces a vertical magnetic field with a sinusoidal dependence along the electron trajectory. The resulting Lorentz force on the drifting electrons modifies their straight trajectory into a zig-zag one, producing a large number of bends with intense radiation emission (see Figure 2.1). The fundamental wavelength of the radiation emitted in an undulator is given by:

$$\lambda_l = \frac{\lambda_u}{2\gamma^2}(1 + \frac{K^2}{2}) \tag{2.1}$$

[1]The transverse emittance ε_t is a parameter that characterizes the transverse phase-space area occupied by the beam. It will be presented in Chapter 3.

Here λ_u is the undulator period length, γ is the Lorentz factor and K is the *undulator parameter*:

$$K = \frac{eB\lambda_u}{2\pi m_e c} \tag{2.2}$$

where B is the peak magnetic field, m_e and e are the mass and the charge of the electron, and c the speed of light.

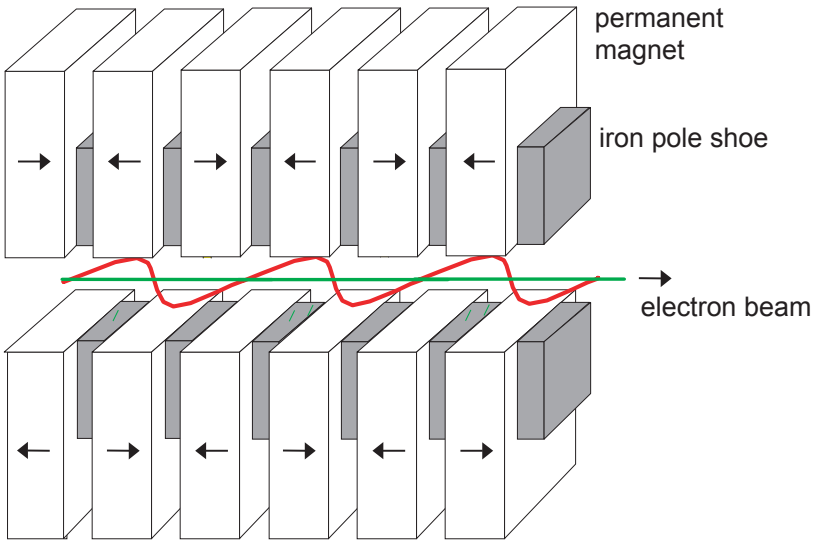

Figure 2.1: Schematic view of a planar hybrid undulator magnet with alternating polarity of the magnetic field and of the sine-like trajectory of the electrons. The magnetic field is produced by permanent magnets that are placed between iron pole shoes. The distance between two equal poles is called the undulator period λ_u, which typically is a few cm of length. Figure from [Doh08].

In Free-Electron Lasers (FELs), considered as the *fourth-generation* light sources, there is a constructive interference between the fields radiated by the different electrons of the bunch, so that FELs produce radiation with full spatial coherence (i.e. laser-like) of extremely high peak brilliance. One of the primary advantages of FELs is that, in contrast to conventional lasers, the radiation wavelength can be varied by simply changing the electron energy (according to equation 2.1).

The generation of coherent radiation is possible if there is a concentration of the electrons in slices which are shorter than the optical wavelength λ_l (a process called *microbunching*). In the undulator, the copropagating radiation overtakes the electrons in one undulator period by λ_l. Due to the periodicity of the system there is a continuous energy exchange between the electron and the photon beam. Depending on the relative phase of the

electrons to the plane wave of the photons, some electrons gain energy from the radiation while others lose energy to the radiation, hence the energy of a long electron bunch is periodically modulated at λ_l. Since electrons with higher energies oscillate with shorter trajectories and particles with lower energies have longer path lengths, the energy modulation turns into the desired density modulation or microbunching.

Without micro-bunching all the electrons in a bunch slice can be treated as individually radiating charges with the power of the spontaneous emission, so the emitted beam power is proportional to the number of electrons in the slice N_e. With microbunching all the electrons radiate almost in the same phase and as a consequence, the beam emits coherently (proportional to N_e^2) at the expense of the beam kinetic energy. This leads to an amplification of many orders of magnitude with respect to the spontaneous emission in the undulator. The exponential growth eventually stops as the beam loses enough energy and can not fulfill the resonance condition 2.1. Both radiation intensity and microbunching reach a maximum saturation level. Figure 2.2 shows the radiation pulse energy growth and schematic microbunching as a function of the undulator length for an FEL.

In order to extract significant radiation power beyond the nominal saturation level, the undulator strength parameter can be tapered to maintain the resonant condition as the electron beam loses energy [Hua01]. In this case, the exponential growth stops because the maximum microbunching is reached and the microbunches become longitudinally *over-focused*.

The microbunching process requires high electron beam intensities (i.e. small beam sizes, small emittances and high currents) and an extremely small energy spread. Compared to storage rings, a linac can produce extremely short electron bunches with very low emittance and energy spread. Due to this fact linacs are much more suitable than circular accelerators to drive the FEL process. Transverse dispersion causes an increase of the effective beam size and emittance which can therefore deteriorate the FEL process and even prevent it.

An FEL can amplify an input seed signal with a wavelength $\lambda \approx \lambda_l$ or the spontaneous radiation produced by the shot-noise. In the last case FEL radiation is obtained by the SASE (Self-Amplified Spontaneous Emission) process [Kon81] [Bon84].

2.2 FEL Characterization

The FEL power *gain length* L_G is the length which is needed to increase the radiation power by a factor of e. In the one-dimensional (1D) model which assumes that the electron beam has a uniform transverse spatial distribution with zero emittance and energy spread, the power gain length can be

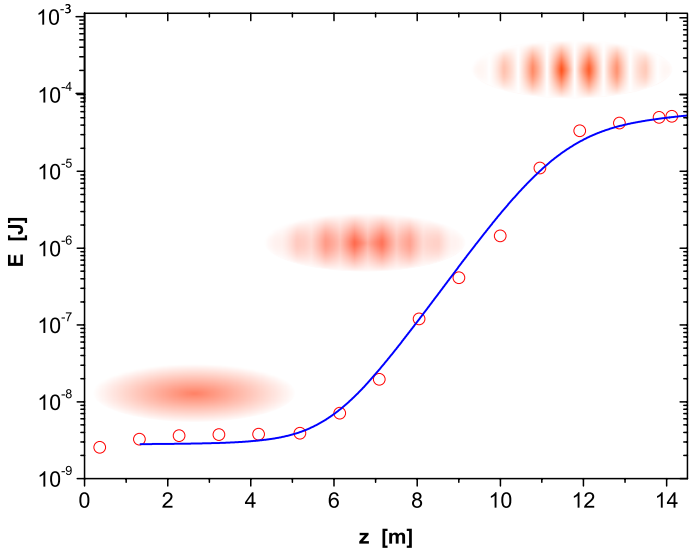

Figure 2.2: Radiation pulse energy growth and schematic microbunching as a function of the undulator length for an FEL. The open circles are data obtained at the SASE FEL of the TESLA Test Facility [Avy02]. At saturation (z $\geq$ 12 m) the microbunches are fully developed and no further increase in radiation power is possible. Figure from [Doh08].

expressed as follows:

$$L_{G_0} = \frac{1}{4\pi\sqrt{3}} \cdot \frac{\lambda_u}{\rho_{FEL}} \tag{2.3}$$

ρ_{FEL} is the (dimensionless) *FEL* or *Pierce parameter*:

$$\rho_{FEL} = \left[\frac{\lambda_u^2 \cdot I \cdot K^2 \cdot [JJ]^2}{64\pi^2 \cdot I_A \cdot \gamma^3 \cdot \sigma_t^2}\right]^{1/3} \propto \frac{I^{1/3}}{\gamma \cdot \sigma_t^{2/3}} \tag{2.4}$$

where $[JJ]$ is the Bessel function factor (a constant value for a given undulator[2]), I_A is the Alfvén current ($I_A \simeq 17$ kA), I is the peak current of the electron beam, and σ_t its transverse beam size:

$$\sigma_t = \sqrt{\sigma_x \sigma_y}$$

In the 1D approximation, the FEL saturation radiation power is about ρ_{FEL} times the electron beam power:

$$P_{sat} \approx \rho_{FEL} \cdot P_{beam}$$

[2] $[JJ]$ is 1 in circular undulators. For planar undulators it is a function of K; for $K \approx 1$ $[JJ]$ is of the order of 1.

The relative bandwidth at saturation is approximately ρ_{FEL}. For short wavelength FELs ρ_{FEL} typically stays between 10^{-3} and 10^{-4}, so the radiation produced by an FEL has a very narrow bandwidth.

Taking into account that the electron current is inversely proportional to the longitudinal beam size (i.e. $I \propto \sigma_l^{-1}$), a crucial parameter for the FEL process is the electron beam density in the 3-dimensional space. We can define the total size of the electron beam σ_{3D} as:

$$\sigma_{3D} = (\sigma_l \sigma_x \sigma_y)^{\frac{1}{3}}$$

From this definition and equations 2.3 and 2.4 the following proportions can be derived:

$$\begin{aligned} L_{G_0} &\propto \sigma_{3D} \\ \rho_{FEL} &\propto \sigma_{3D}^{-1} \end{aligned} \tag{2.5}$$

From the above relations it can be seen that high-peak currents and low transverse beam sizes are required for high-gain FELs. Typical values for high-gain FELs like FLASH or the XFEL are peak currents of the order of few kA and beam sizes below the 100 µm level. For instance, the design values for FLASH are: I = 2.5 kA, $\sigma_t = 60 \div 90$ µm. Figure 2.3 shows ρ_{FEL} and L_{G_0} for the design parameters of FLASH as a function of the electron energy, which can presently vary from 450 MeV up to 1 GeV. ρ_{FEL} stays in the order of 10^{-3} and the 1D gain length below the 1 m level.

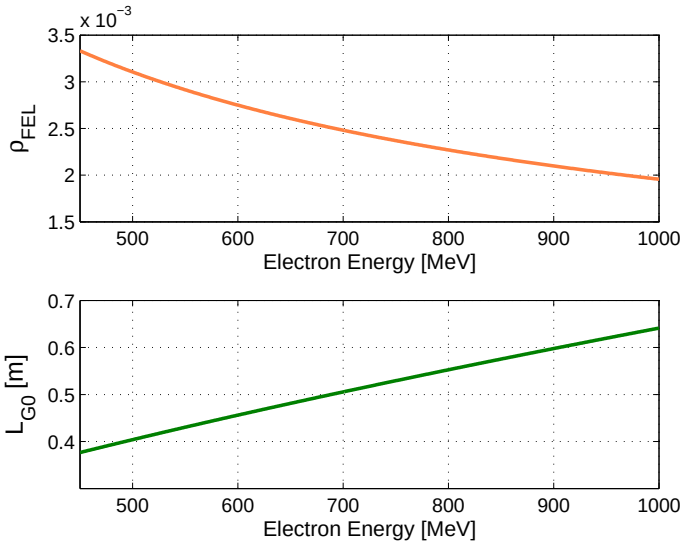

Figure 2.3: Pierce parameter and 1D gain length for design FLASH parameters as a function of the electron energy.

2.2.1 Increase of Gain Length by 3D Effects

For real beams the following effects contribute to the increase of the gain length:

- A finite *energy spread* induces a longitudinal velocity spread which leads to a significant increase of the gain length. For an RMS (Root Mean Square) energy spread equal to $0.5 \cdot \rho_{FEL}$ the gain length is about 25 % larger than L_{G_0} ($L_G \approx 1.25 L_{G_0}$) [Doh08].

- A non-zero transverse velocity $v_x \approx c \cdot x'$ is equivalent to an additional energy spread of the beam. If $\langle x'^2 \rangle = \frac{\rho_{FEL}}{2\gamma^2}$, the real gain length is increased by 25 % with respect to L_{G_0} [Doh08].

- *Optical diffraction* can also decrease the power gain of a realistic FEL. The Rayleigh length L_R is defined as the distance over which the beam cross section has increased by a factor of two from its minimum value and can be calculated with the following expression:

  $$L_R = 4\pi\sigma_t^2/\lambda_l$$

  To avoid a weak overlap between the electron and the photon beam L_R should not be much smaller than L_G. Assuming that L_G is as small as possible, L_G should be approximately L_R [Doh09].

- The amplification process in the FEL depends strongly on a good *transverse overlap* between the electron and the photon beam. As a consequence, the deviation of the electrons with respect to the design trajectory must be stringently controlled. Detailed studies of the electron beam trajectory impact on the FEL performance at FLASH will be presented in Chapter 7.

  In addition, in order to keep the beam size as constant as possible along the undulator, focusing is needed and the beam must be properly matched in the undulator entrance.

More detailed information about FEL theory can be found in [Sal99], [Hua07] and [Doh08].

2.2.2 Numerical Estimation of 3D-effects

M. Xie [Xie95] has expressed the real gain length of an FEL as:

$$L_G = L_{G_0}(1 + \eta) \tag{2.6}$$

The correction factor η has been obtained by three-dimensional numerical studies. This parametrization takes into account the increase of the gain

length due to energy spread, emittance (i.e. transverse velocity) and optical diffraction. Figure 2.4 shows the 1D and 3D gain length (obtained using equation 2.6) for the design FLASH parameters (with an estimated energy spread $\Delta p = 1$ MeV). The correction factor η is also plotted.

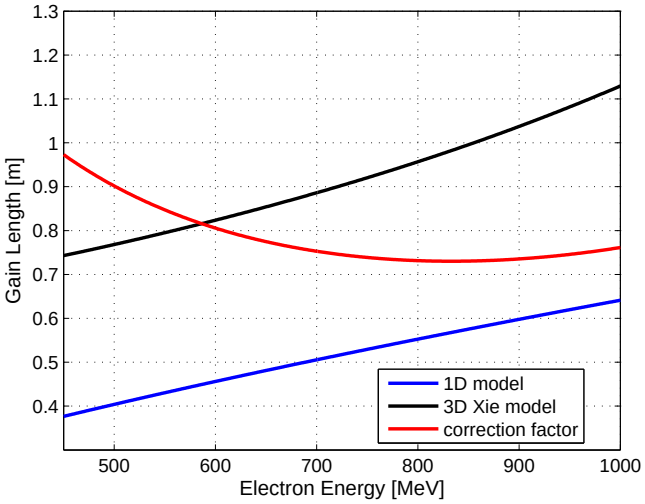

Figure 2.4: 1D and 3D gain length for FLASH design parameters. The correction factor to the 1D gain length is also plotted.

2.3 FLASH

FLASH, based on the TTF[3], is a user facility at DESY and a pilot facility for the XFEL and the International Linear Collider (ILC) projects. It generates SASE-FEL radiation with a wavelength ranging from the vacuum ultraviolet to the soft x-ray regime. FLASH demonstrated SASE operation at a wavelength of 32 nm in 2005 [Ayv06], at 13 nm in 2006 [Ros06] [Ack07] and at 6.5 nm (design value) in 2007 [Sch08].

A schematic layout of FLASH is shown in Figure 2.5. FLASH operates in pulsed mode with a *macropulse* repetition rate of up to 5 Hz. Each macropulse is 0.8 ms long. Within each macropulse there can be up to 800 bunches separated by 1 µs.

Electron bunches are generated in a laser-driven RF gun with a nominal bunch charge of 1 nC. The electron beam energy can be presently increased up to 1 GeV in six TESLA accelerating modules, each of them containing eight superconducting cavities. This maximum energy corresponds to a radiation wavelength of 6.4 nm. A further energy upgrade is planned in late 2009.

[3]TESLA Test Facility [Ros96] [TTF02].

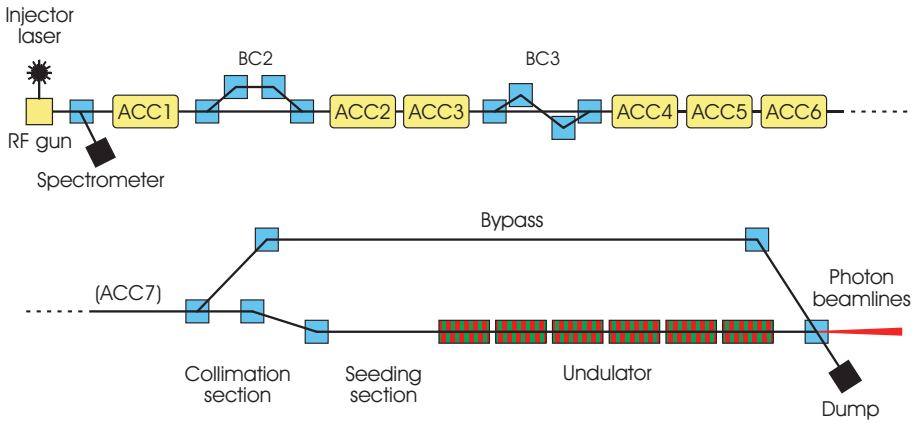

Figure 2.5: Schematic layout of FLASH (not to scale). Total length is about 250 m. The elements shown include acceleration structures (yellow), FEL undulators (green/red), and main dipole magnets (blue).

The electron bunches are longitudinally compressed in two bunch compressor chicanes to reach the peak current necessary for the SASE process. The first bunch compressor (BC2) [Lim96] is located after the first accelerating section ($E = 127$ MeV) and can reduce the bunch length by up to about a factor of 10. The second bunch compressor (BC3) [Stu04] is placed after the accelerator modules ACC23 ($E = 450$ MeV) and can further compress the beam by about a factor of 4. In total, the bunch compression system of FLASH can reduce the initial bunch length after the gun of 2 mm down to 50 µm (RMS values), corresponding to a final design peak current of 2.5 kA. A third-harmonic cavity which will optimize the longitudinal compression is foreseen to be installed in late 2009.

After the modules that provide the final acceleration ($E = 1$ GeV) there is a collimation section that protects the undulator from radiation damage. This is done by removing electrons with energy deviation larger than $\pm 3\,\%$ and with large betatron amplitudes [Bal03].

The undulator section consists of six permanent magnet undulators with a length of 4.5 m each. The gap is fixed at 12 mm, the peak magnetic field is 0.486 T, and the undulator length is $\lambda_u = 27.3$ mm [Pfl03]. A pair of quadrupoles placed between each of the six modules provide the focusing required to keep the beam size in the whole section both small and constant as possible.

A dipole magnet after the undulator section deflects the electron beam into a dump [Mas99], while the FEL radiation propagates to the experimental hall. In order to facilitate machine commissioning and to perform accelerator component experiments the beam can bypass the collimator and undulator sections.

2.4 XFEL

The XFEL will be a multi-user facility providing photon radiation in a wavelength regime from 0.1 nm to 5 nm in three FEL beam lines and hard X-rays in two spontaneous radiation beam lines. The project is in an advanced planning and technical preparation stage and its civil construction as a European/International facility near DESY in Hamburg started in 2008.

A schematic layout of the XFEL is shown in Figure 2.6. Like FLASH, the XFEL operates in a pulsed mode. In this case the repetition rate is 10 Hz and there can be up to about 3000 micropulses within each macropulse.

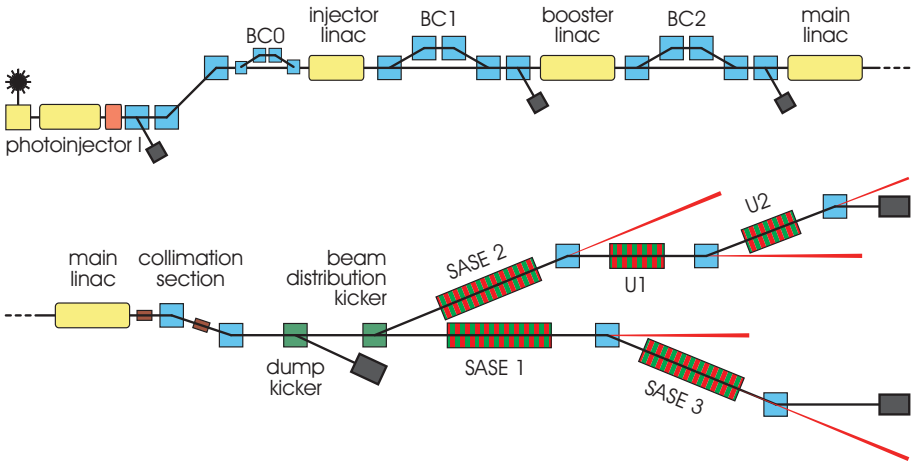

Figure 2.6: Schematic layout of the XFEL (not to scale). Total length is about 3 km. The elements shown include 1.3 GHz RF sections (yellow), the 3.9 GHz acceleration structure (red), undulators (green/red), and main dipole magnets (blue).

In the injector section electron bunches are extracted from a solid cathode by a laser beam and accelerated by an RF gun up to an energy of about 130 MeV. In the following section (0.4 km) the electrons are longitudinally compressed in three different stages to generate the high-density bunches required for the SASE process. The longitudinal beam size is compressed by a factor of 100 (from 2 mm to 0.02 mm), leading to a peak current of 5 kA. The energy at the end of the bunch compression section is about 2.0 GeV. A third-harmonic RF system placed in the injector section is used to optimize the final longitudinal charge distribution.

In the main linear accelerator (1.2 km) the electrons are further accelerated to energies of up to 20 GeV. At the end of the linac there is a beam transport section with collimation and stabilization feedback, after which the individual electron bunches are fed into one or the other of two electron beam lines by the beam distribution system. The linac and the beam transport line are housed in a 2.1 km long underground tunnel.

Although the baseline operating point will be at 0.1 nm (corresponding to an electron energy of 17.5 GeV), independent wavelength tuning by undulator gap variation is foreseen.

Further details of the XFEL facility can be found in the technical design report [Agh07].

Table 2.1: Main parameters of FLASH and the XFEL.

Item	FLASH	XFEL
Maximum electron energy [GeV]	1.0	17.5 (20)
Minimum radiation wavelength [nm]	6.4	0.1
Bunch charge [nC]	1	1
Repetition rate [Hz]	5	10
Maximum RF pulse flat-top length [ms]	0.8	0.65
Maximum number of bunches	800	3250 (3000)
Maximum average beam power [kW]	4	600
Peak current [kA]	2.5	5.0
Design emittance [µrad]	2.0 (projected)	1.4 (slice)
Slice energy spread at undulator [MeV]	0.5	1
Number of accelerator modules	6	100
Number of accelerator cavities	48	820
Number of undulators	1	5
Linac length [m]	150	1600
Facility length [m]	300	3400
Brilliance (*)	10^{29}	10^{33}
ρ_{FEL}	$\sim 10^{-3}$	$\sim 10^{-4}$

(*) [photons/(sec·mrad^2·mm^2·0.1%bandwidth)]

Chapter 3

Dispersion in Linacs

Dispersion is the momentum dependence of charged particle deflections in a magnetic field. The force exerted to a particle under the presence of a magnetic field $\vec{B}$ is the so-called Lorentz force:

$$\vec{F} = e \cdot \vec{v} \times \vec{B} \tag{3.1}$$

where $\vec{v}$ and e are the velocity and the charge of the particle. According to the Lorentz force, an electron experiences a deflection with a radius of curvature ρ given by:

$$\frac{1}{\rho} = \frac{eB}{p} \tag{3.2}$$

where p is the momentum of the particle. The above equation 3.2 shows that the deflection exerted by a magnetic field is inversely proportional to the particle momentum. Since the deflection is momentum-dependent, particles with different momentums will follow different trajectories.

3.1 Single Particle Beam Transport

3.1.1 Matrix Formalism

To characterize a particle state a coordinate system which moves along the trajectory of a reference particle with the design momentum p_0 is used (see Figure 3.1). The coordinates which describe the motion are:

$$\vec{X}(s) = (x(s), x'(s), y(s), y'(s), \xi(s), \delta(s)) \tag{3.3}$$

where s is the longitudinal position along the accelerator, x and y refer to the horizontal and the vertical transverse displacements, $x' = dx/ds$ and $y' = dy/ds$ are the horizontal and the vertical slopes, ξ is the longitudinal displacement, and δ is the relative momentum deviation ($\delta = (p - p_0)/p_0 = \Delta p/p_0$).

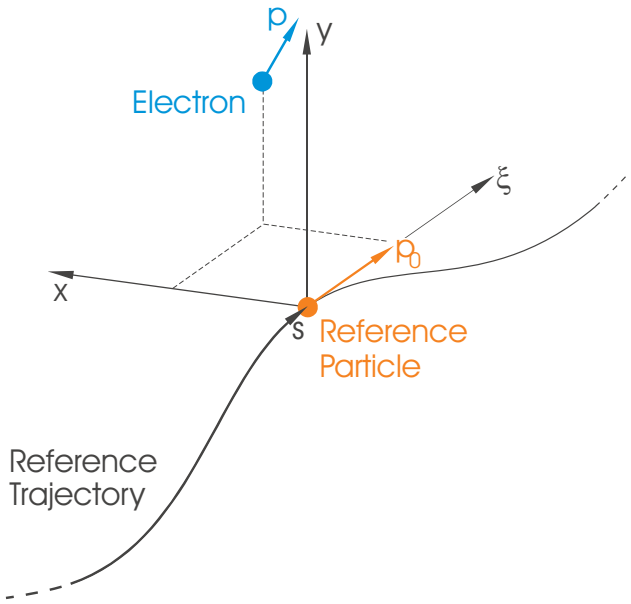

Figure 3.1: Coordinates system used to described particle trajectories.

The first-order transformation of the particle coordinates from an initial position s_0 to a position s can be described by a matrix formalism [Bro82] [Ros92]:

$$\vec{X}(s) = \boldsymbol{R}(s_0, s) \cdot \vec{X}(s_0) \tag{3.4}$$

The elements placed in the 6th column of $\boldsymbol{R}(s_0, s)$ are called dispersion terms and describe the linear momentum-dependent part of the electron motion. They are defined as the derivative of each of the phase-space coordinates at the position s with respect to the relative momentum deviation at s_0. The first four terms characterize the linear part of the transverse dispersion, henceforth referred to as *dispersion*.

Up to now only linear transformations have been considered. The matrix formalism can be extended to higher order contributions [Bro82]:

$$\begin{aligned} X_i(s) = &\sum_j R_{ij}(s_0, s) X_j(s_0) + \sum_{jk} T_{ijk}(s_0, s) X_j(s_0) X_k(s_0) + \\ &+ \sum_{jkl} U_{ijkl}(s_0, s) X_j(s_0) X_k(s_0) X_l(s_0) + \cdots \end{aligned} \tag{3.5}$$

where $\boldsymbol{T}$ and $\boldsymbol{U}$ describe the second and the third-order transport.

3.1.2 Dispersion Functions

The dispersion functions describe the change in phase-space coordinates at s due to a momentum change at s_0. The first and second-order horizontal dispersion functions can be expressed using the matrix formalism (up to second order) as follows:

$$\begin{aligned} D_x(s_0,s) &= R_{16}(s_0,s) + T_{116}(s_0,s)x(s_0) + T_{126}(s_0,s)x'(s_0) + \\ &+ T_{136}(s_0,s)y(s_0) + T_{146}(s_0,s)y'(s_0) + \\ &+ T_{156}(s_0,s)\xi(s_0) + T_{166}(s_0,s)\delta(s_0) \end{aligned}$$

$$\begin{aligned} D'_x(s_0,s) &= R_{26}(s_0,s) + T_{216}(s_0,s)x(s_0) + T_{226}(s_0,s)x'(s_0) + \\ &+ T_{236}(s_0,s)y(s_0) + T_{246}(s_0,s)y'(s_0) + \\ &+ T_{256}(s_0,s)\xi(s_0) + T_{266}(s_0,s)\delta(s_0) \end{aligned} \tag{3.6}$$

$$D_{xx}(s_0,s) = T_{166}(s_0,s) \qquad D'_{xx}(s_0,s) = T_{266}(s_0,s)$$

The vertical dispersion functions (D_y, D'_y, D_{yy}, and D'_{yy}) can be written accordingly replacing the horizontal matrix elements from the above equation with their corresponding vertical elements (i.e. replacing the matrix indexes 1-2 with 3-4).

Concerning the linear dispersion functions, as it can be seen from equation 3.6, while the first-order matrix terms (R_{16} and R_{26} for the horizontal plane) always create dispersion, a second-order matrix term generates dispersion only when the particle coordinate related to the term is not zero (for instance, the term T_{116} contributes to D_x only when x is not zero). These first and second-order dispersion matrix terms will be given in Chapter 4 for different magnets types and accelerator cavities.

In linacs, since none of the dispersion sources upstream of the initial position s_0 contribute to $D(s_0,s)$, dispersion can differ significantly depending on the location of s_0, as shown in the example in Figure 3.2. That is not the case in circular accelerators, where all the sources in the lattice contribute to $D(s_0,s)$ (independently of the location of s_0). As a consequence, in rings there is not the need to define the dispersion as a function of an initial position s_0 and therefore it is usually defined as a closed periodic function $D = D(s)$.

3.1.3 Beam Offsets and Angles

The electron transverse motion along the accelerator can be characterized as the sum of a *betatron* or momentum-independent part plus a *dispersive* or momentum-dependent part.

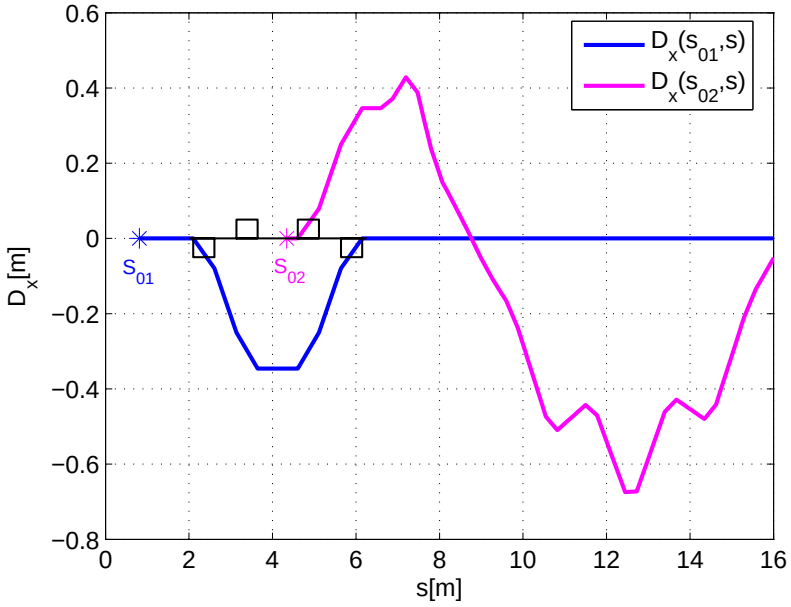

Figure 3.2: Horizontal dispersion $D_x(s_0, s)$ along the first bunch compressor section of FLASH and downstream for two different initial positions. If the initial position is upstream of the bunch compressor (s_{01}) the dispersion after the bunch compressor is closed (i.e. $D_x = D'_x = 0$). If the initial position is within the bunch compressor (s_{02}), the resulting dispersion downstream of the section is not zero.

The transverse coordinates of an electron can be obtained as follows:

$$\begin{aligned} x(s) &= x_\beta(s) + x_D(s) \\ x'(s) &= x'_\beta(s) + x'_D(s) \end{aligned} \tag{3.7}$$

where the subindex β refers to the betatron component of the motion and the subindex D refers to the dispersive component of the motion. Up to second order, the variation of x_D and x'_D from s_0 to s can be computed as follows:

$$\begin{aligned} \Delta x_D &= x_D(s) - x_D(s_0) = D_x(s_0, s) \cdot \delta(s_0) + D_{xx}(s_0, s) \cdot \delta^2(s_0) \\ \Delta x'_D &= x'_D(s) - x'_D(s_0) = D'_x(s_0, s) \cdot \delta(s_0) + D'_{xx}(s_0, s) \cdot \delta^2(s_0) \end{aligned} \tag{3.8}$$

where $\delta(s_0)$ is the initial relative momentum of the particle, and $D_x(s_0, s)$, $D'_x(s_0, s)$, $D_{xx}(s_0, s)$ and $D'_{xx}(s_0, s)$ are the first and second-order dispersion functions from s_0 to s.

3.2 Effects on the Electron Beam Distribution

How the dispersion will affect the transverse beam distribution depends on the momentum distribution of the beam along the accelerator. In circular accelerators, the combination of radiation damping and quantum excitation gives an equilibrium which results in a stable momentum distribution of the bunch along the lattice [Wal92] [Cha99]. On the contrary, in linacs the beam momentum distribution can change significantly along the accelerator[1]. As a consequence, the dispersion in linacs can have a different effect depending on the position of the dispersion sources along the lattice.

Example: C-shape at FLASH

In the screen of the first bunch compressor (BC2) of FLASH, where there is a strong nominal horizontal dispersion (about -35 cm), the beam can present a characteristic *c-shape*: the head and the tail of the bunch are vertically separated but in the same horizontal position (see Figure 3.3).

This effect is observed when the accelerator module ACC1 runs at on-crest operation, which means that the head and the tail have approximately the same energy at BC2. However, the head and the tail have different energies upstream of ACC1. Therefore, a vertical dispersion source between the gun and ACC1 would cause the c-shape effect.

Figure 3.3 shows simulation results and a measurement of a c-shaped beam (bottom plot). The top plots correspond to the simulation case in which the vertical dispersion is created upstream of ACC1, which produces the c-shape effect at BC2. The middle plots correspond to the simulation case in which the vertical dispersion is created downstream of ACC1, for which no effect is observed at BC2. In both cases the dispersion is generated by a kick of $3{\cdot}10^{-4}$ Tm. The image at the top of BC2 (left side), as well as the longitudinal phase-space at the place where the dispersion is created (right), are plotted.

To explain this effect in terms of dispersion in a circular accelerator would be paradoxical, since the head and the tail would need to have the same energy according to the horizontal dispersion but would need to have different energies according to the vertical dispersion.

Detailed studies on the c-shape effects at FLASH will be presented in Appendix A.

[1] For instance due to Coherent Synchrotron Radiation (CSR) effects at the bunch compressors.

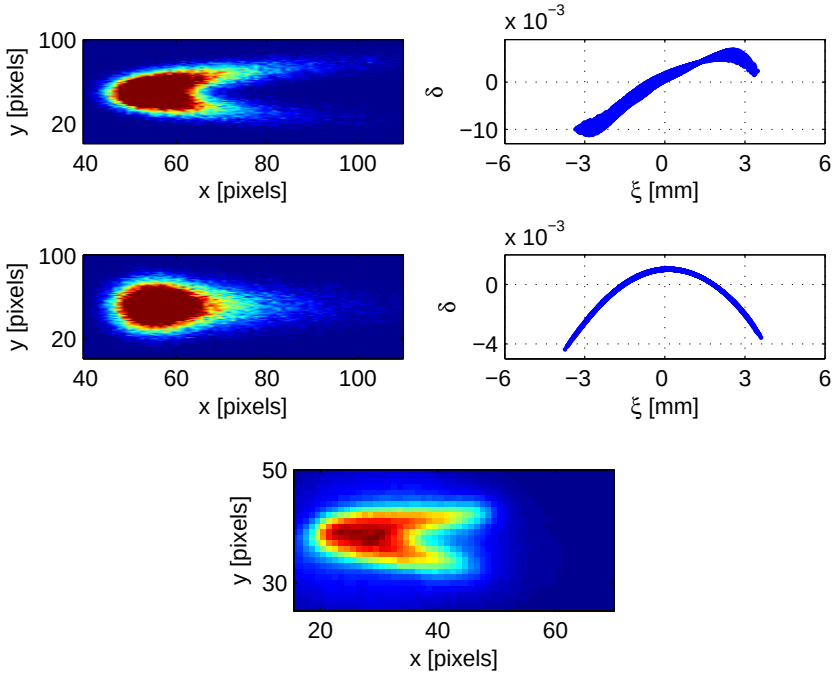

Figure 3.3: Simulation results and a measurement (bottom plot) of the c-shape effect at FLASH. The top plots correspond to the simulation case in which a vertical dispersion source is introduced upstream of ACC1. Middle plots show the simulation case in which the vertical dispersion is generated downstream of ACC1. In each case the beam image in the screen of BC2 (left) and the relative momentum distribution at the point where the dispersion is created (right) are plotted.

3.2.1 Statistical Effects

Second Moments and Emittance

This section is restricted to the two-dimensional (2D) transverse phase-space distribution. Although we will only refer to the beam distribution in the horizontal plane, an equivalent treatment is valid for the vertical direction.

The RMS *beam size* σ_x, the RMS *beam divergence* σ'_x, and the RMS *beam coupling term* $\sigma\sigma'_x$ can be obtained from the second moments of the particle distribution:

$$\begin{aligned} \sigma_x &= \sqrt{\langle (x - \langle x \rangle)^2 \rangle} \\ \sigma'_x &= \sqrt{\langle (x' - \langle x' \rangle)^2 \rangle} \\ \sigma\sigma'_x &= \langle (x - \langle x \rangle) \cdot (x' - \langle x' \rangle) \rangle \end{aligned} \tag{3.9}$$

The *beam matrix* is defined as:

$$\sigma_{xx} = \begin{pmatrix} \sigma_x^2 & \sigma\sigma'_x \\ \sigma\sigma'_x & \sigma'^2_x \end{pmatrix} \tag{3.10}$$

The 2D RMS *emittance* is the area in the phase-space $x - x'$ occupied by the fraction of the beam distribution which is determined by its second-order moments. The emittance allows characterizing the transverse beam distribution with a single quantity, integrating the three parameters from equation 3.9. It can be obtained using the following expression:

$$\varepsilon_x = \sqrt{det(\sigma_{xx})} = \sqrt{\sigma_x^2 \cdot \sigma'^2_x - (\sigma\sigma'_x)^2} \tag{3.11}$$

The beam matrix is related to the emittance and the so-called *Twiss parameters* (i.e. the optical functions β, α and γ) according to the following expression:

$$\sigma_{xx} = \varepsilon_x \begin{pmatrix} \beta_x & -\alpha_x \\ -\alpha_x & \gamma_x \end{pmatrix} \tag{3.12}$$

or equivalently:

$$\begin{aligned} \sigma_x^2 &= \varepsilon_x \beta_x \\ \sigma'^2_x &= \varepsilon_x \gamma_x \\ \sigma\sigma'_x &= -\varepsilon_x \alpha_x \end{aligned} \tag{3.13}$$

Betatron and Dispersive Components

In the presence of dispersion electrons with different energies follow different trajectories and as a consequence, the second moments of the beam distribution are increased. Assuming that the betatron and dispersive components of the motion are uncorrelated, the beam size, divergence and coupling can be expressed as:

$$\begin{aligned} \sigma_x^2 &= \sigma_{\beta_x}^2 + \sigma_{D_x}^2 = \varepsilon_{\beta_x}\beta_x + \langle x_D^2 \rangle \\ \sigma'^2_x &= \sigma'^2_{\beta_x} + \sigma'^2_{D_x} = \varepsilon_{\beta_x}\gamma_x + \langle x'^2_D \rangle \\ \sigma\sigma'_x &= \sigma\sigma'_{\beta_x} + \sigma\sigma'_{D_x} = -\varepsilon_{\beta_x}\alpha_x + \langle x_D x'_D \rangle \end{aligned} \tag{3.14}$$

where the subindex β refers to the betatron components and the subindex D to the dispersive components of the beam size, the beam divergence, and the beam coupling term respectively. x_D and x'_D are the beam offsets and angles computed in equation 3.8. The beam size, the divergence and the coupling term will be equal to their betatronic values only without dispersion. With dispersion the *effective* values will increase according to equation 3.14.

Liouville's theorem states that the betatron emittance ε_{β_x} remains constant if the energy is constant and in the absence of coupling and stochastic effects. The *normalized* emittance $\varepsilon_{Nx_\beta} = \dfrac{p}{m_0 c} \cdot \varepsilon_{\beta_x}$ stays constant also

during acceleration. The *effective* emittance ε_x (calculated from the measurements of the transverse beam sizes) will be equal to the pure betatron emittance ε_{x_β} only in the absence of dispersion. In the presence of dispersion the emittance increase due to dispersion can be obtained using equations 3.11 and 3.14:

$$\frac{\varepsilon_x}{\varepsilon_{\beta_x}} = \sqrt{1 + \frac{\langle x_D^2\rangle\gamma_x + \langle x_D'^2\rangle\beta_x + 2\langle x_D x_D'\rangle\alpha_x}{\varepsilon_{\beta_x}}} \tag{3.15}$$

Figure 3.4 shows, for a certain amount of dispersion, how the effective beam size and emittance increase as a function of the relative momentum deviation. Figure 3.5 shows an example of how the particle distribution can be affected due to dispersion. In these examples, $\delta(s)$ is taken as constant along s.

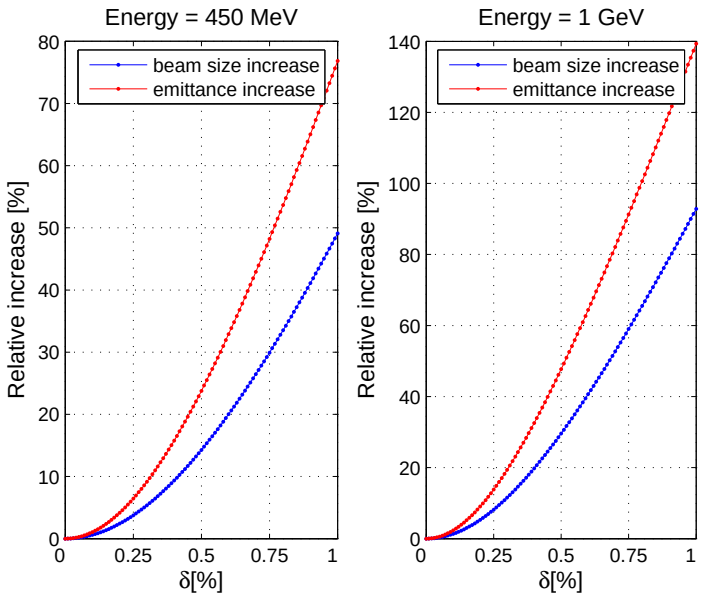

Figure 3.4: Example of beam size and emittance increase due to dispersion as a function of the relative momentum deviation δ. The considered dispersion is $D_x = 10$ mm and $D_x' = 1$ mrad. Left plot corresponds to an energy of E = 450 MeV, right plot to E = 1 GeV. The Twiss parameters are $\beta_x = 3.6$ m (design average value for FLASH undulator) and $\alpha_x = 0.5$. Normalized emittance is $\varepsilon_{Nx_\beta} = 2.00$ µm (design value for FLASH).

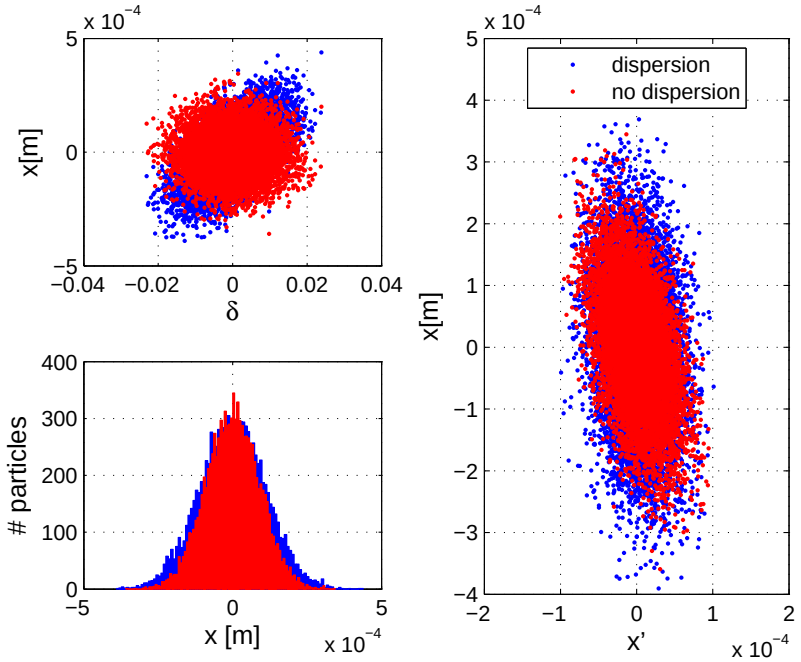

Figure 3.5: Example of dispersion effects on the beam distribution. Gaussian beams with 10^4 particles are plotted. The figure shows horizontal position versus relative momentum deviation (upper left plot), horizontal position histogram (lower left plot) and horizontal phase-space (right plot) without dispersion and with dispersion ($D_x = 10$ mm and $D'_x = 1$ mrad). Beam properties are: E = 450 MeV, δ =0.67 %, $\beta_x = 3.6$ m, $\alpha_x = 0.5$, $\varepsilon_{Nx_\beta} = 2.00$ µm. Due to the dispersion the beam size increases 24 % (from 90 µm to 112 µm) and the normalized emittance goes up to 2.78 µm (an increase of 39 %).

3.3 Effects on the FEL Process

Increase of Gain Length

Dispersion causes an increase of the effective transverse beam size and emittance which turns into an increase of the gain length L_G. The increase of the gain length due to dispersion using the parametrization described in Section 2.2.2 has been calculated for FLASH design parameters. This takes into account the increase of the gain length due to energy spread, emittance, and optical diffraction. The results are shown in Figure 3.6. To keep the increase of the gain length due to dispersion below 10 %, the average dispersion in the undulator must be smaller than 1.8 cm.

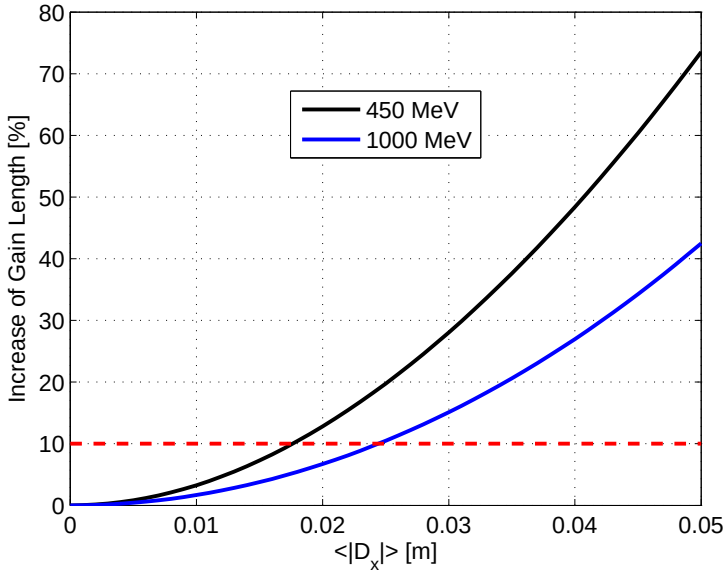

Figure 3.6: Increase of the gain length as a function of dispersion (average absolute value) for FLASH design parameters: $\varepsilon_{N_\beta} = 2.00$ µm, $\langle\beta\rangle = 3.6$ m, Δp = 1.0 MeV, I = 2500 A. The figure shows the results for two different electron energies: 1 GeV and 450 MeV. To keep the contribution of the dispersion below 10 % for all the energies, dispersion must be smaller than 1.8 cm.

Intra-bunch Trajectory Deviations

In general, the longitudinal slices of the beam that produce FEL radiation have different energies. Without dispersion, all the slices follow the same trajectory and can potentially radiate. With dispersion, the slices with an momentum offset travel off-axis so that they do not generate FEL radiation. In most of the cases the introduction of dispersion results in a reduction of the total FEL power (less slices radiate) and in the narrowing of the radiation spectrum (only the on-momentum slices radiate). Studies dedicated to the impact of dispersion to the SASE spectrum are presented in Chapter 7.

Chapter 4

Dispersion Generation Mechanisms

4.1 Dispersion in Single Elements

4.1.1 Dispersion in Dipole Magnets

A pure dipole magnet generates a homogeneous field B. The radius of the curvature ρ for a particle with charge e with momentum p is given by:

$$\frac{1}{\rho} = \frac{\varphi}{l} = \frac{eB}{p} \tag{4.1}$$

where l and φ are the length and the deflection angle of the dipole magnet. The above relation shows that the deflection given by a dipole magnet depends linearly on the momentum of the particle, i.e. particles with more energy are less bent than particles with lower energy.

The first-order dispersion matrix terms at the end of a horizontal dipole sector magnet of length l and radius ρ are given by [Ros92]:

$$\begin{aligned} R_{16} &= \rho(1 - \cos\varphi) \\ R_{26} &= \sin\varphi \end{aligned} \tag{4.2}$$

where $\varphi = l/\rho$ is the bending angle of the magnet. If φ is small enough, equation 4.2 can be simplified:

$$\begin{aligned} R_{16} &\simeq 0 \\ R_{26} &\simeq \varphi \end{aligned} \tag{4.3}$$

The second-order dispersion matrix terms of a dipole magnet are not zero due to the fringe fields. We have to distinguish between a *dipole sector magnet* (with the magnet ends perpendicular to the beam trajectory) and a *rectangular dipole magnet* (i.e. magnet built straight with the magnet

end plates not perpendicular to the electron trajectory but parallel to each other). A dipole sector magnet has weak focusing in the plane of the bending, while a rectangular dipole focuses the beam in the contrary plane of the bending. As a consequence, for a horizontal dipole sector magnet the terms T_{116}, T_{126}, T_{216} and T_{226} are non-zero. On the other hand, for a horizontal rectangular dipole magnet the terms T_{336}, T_{346}, T_{436} and T_{446} are not zero. Moreover, for both types of dipole magnets the second-order terms T_{166} and T_{266} are non-zero. Appendix B presents the expressions used to calculate the second-order matrix elements for a sector dipole magnet.

4.1.2 Dispersion in Quadrupole Magnets

A pure quadrupole magnet produces a linear field in the deviation from its axis. The field components of a horizontally focusing quadrupole can be parametrized as follows:

$$B_y = -gx \qquad \text{and} \qquad B_x = -gy \tag{4.4}$$

where g is the constant gradient of the magnet. The strength k of a quadrupole magnet of length l can be obtained from:

$$kl = \frac{1}{f} = \frac{eg}{p} \tag{4.5}$$

where f is the focal length of the quadrupole magnet. We see from the above equation that the focusing of a quadrupole magnet depends linearly on the particle momentum.

All dispersive elements of the first-order matrix R are zero for a quadrupole magnet. However, the momentum dependence of its focusing translates into the following non-zero second-order dispersion terms [Bro82]:

$$\begin{aligned}
T_{116} &= \frac{1}{2}\varphi \sin\varphi \\
T_{126} &= \frac{1}{2}\left(\frac{1}{\sqrt{|k|}} \sin\varphi - l\cos\varphi\right) \\
T_{216} &= \frac{\sqrt{|k|}}{2}(\varphi\cos\varphi + \sin\varphi) \\
T_{226} &= \frac{1}{2}\varphi \sin\varphi \\
T_{336} &= -\frac{1}{2}\varphi \sin\varphi \\
T_{346} &= \frac{1}{2}\left(\frac{1}{\sqrt{|k|}} \sinh\varphi - l\cosh\varphi\right) \\
T_{436} &= -\frac{\sqrt{|k|}}{2}(\varphi\cosh\varphi + \sinh\varphi) \\
T_{446} &= -\frac{1}{2}\varphi \sinh\varphi
\end{aligned} \tag{4.6}$$

$$\text{with} \qquad \varphi = l\sqrt{|k|} \tag{4.7}$$

4.1.3 Dispersion in RF Accelerator Cavities

A high gradient standing wave linear accelerator provides axisymmetric transverse focusing due to the presence of strong alternating gradient transverse electromagnetic fields arising from the backward RF wave. It can be shown that for a pure π-mode standing-wave cavity, the matrix which describes the passage of the electron through the entire cavity is [Ros93] [Ros94]:

$$\begin{pmatrix} \cos\alpha - \sqrt{2}\sin\alpha & \sqrt{8}\frac{\gamma_i}{\gamma'}\sin\alpha \\ -\frac{3\gamma'}{\sqrt{8}\gamma_f}\sin\alpha & \frac{\gamma_i}{\gamma_f}[\cos\alpha + \sqrt{2}\sin\alpha] \end{pmatrix} \tag{4.8}$$

$$\text{with} \qquad \alpha = \frac{1}{\sqrt{8}}\ln(\frac{\gamma_f}{\gamma_i})$$

where γ_f and γ_i are the final and the initial beam energies and γ' is the gradient in the particle energy averaged over a period of the structure:

$$\gamma' = \frac{e\overline{E}_{RF}}{mc^2}$$

with $\overline{E}_{RF}$ being the average accelerating gradient.

From equation 4.8 the *equivalent quadrupole strength* of an RF accelerator cavity can be derived:

$$k_{cav}l = \frac{3\gamma'}{\sqrt{8}\gamma_f}\sin\alpha \tag{4.9}$$

As it can be observed from above equation, k_{cav} becomes important for high accelerating gradients at low beam energies.

As in the case of a quadrupole magnet, the terms T_{116}, T_{126}, T_{216}, T_{226}, T_{336}, T_{346}, T_{436}, and T_{446} are not zero for an RF cavity. Equation 4.6 can be used to obtain these second-order dispersion terms (replacing k with k_{cav}).

4.1.4 Dispersion in Sextupoles and Higher Multipole Magnets

A pure sextupole magnet generates a quadratic field in the deviation from its axis. As in the quadrupole case, we can define the sextupole strength m:

$$m = \frac{eg'}{p} \tag{4.10}$$

where g' is the second derivative of the magnetic field which for a sextupole magnet is ideally constant. Due to the chromatic dependence of the sextupole strength on the momentum a sextupole magnet creates third-order dispersion.

The strength for a magnet of 2n poles can be generally defined:

$$s = \frac{eg^{(n-2)'}}{p} \tag{4.11}$$

where $g^{(n-2)'}$ is the (n-1) derivative of the magnetic field of the multipole. Since s depends linearly on the particle momentum, a magnet of 2n poles generates dispersion of order n.

4.2 Dispersive Sections at FELs

4.2.1 Bunch Compressors

Bunch compressors are used in FELs to compress the beam longitudinally. They consist of several bending magnets (typically 4 or 6) with drift spaces in between. There are two bunch compressors at FLASH. The first one (BC2) is an 18 degrees four-bending-chicane and the second one (BC3) is a 3.8 degrees six-bending-chicane. Figure 4.1 shows the design absolute trajectory and dispersion (with a reversed sign) through both bunch compressors of FLASH. Both trajectory and dispersion are *closed* at the end of the bunch compressors (i.e. $x = x' = D_x = D'_x = 0$).

4.2.2 Collimator Sections

Collimator sections are used in FELs to protect the undulator from radiation damage. The collimator section of FLASH is a *dog-leg* made of two dipole magnets with a horizontal bending angle of 3.5 degrees. The apertures were chosen in order to remove electrons with an energy deviation larger than 3 % [Bal03].

If the collimator section would consist only of two horizontal dipole magnets and a drift space in between, the outgoing dispersion would be:

$$\begin{aligned} D_x &\simeq L\varphi \\ D'_x &= 0 \end{aligned} \tag{4.12}$$

where L is the length of the drift and φ is the collimator angle.

Two quadrupole magnets with the same strength can be used to suppress the first-order dispersion of the collimator. They must be focusing in the bending plane of the dipole magnets.

Let us call the dipole and the quadrupole magnets of the collimator section D1, D2, Q1, and Q2. If L_1 is the distance between D1 and Q1, $L2$

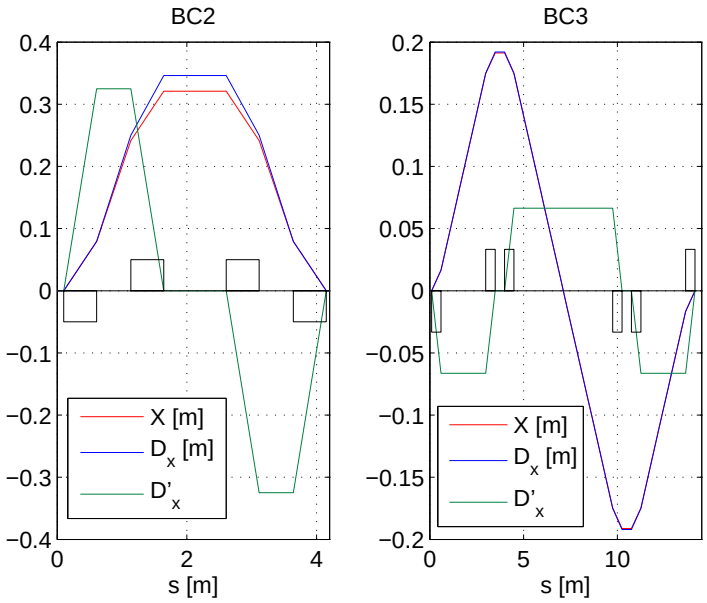

Figure 4.1: Design absolute trajectory (X) and dispersion (with reversed sign) in the bunch compressors of FLASH.

- the distance between Q1 and Q2, and L_3 - the distance between Q2 and D2 ($L_3 = L_1$ for symmetry), it can be shown that the required strength of the magnets does not depend on the collimator angle and is approximately [Pan54]

$$\frac{-1}{f} = kl \simeq \frac{2L_1 + L_2}{L_1 L_2} \tag{4.13}$$

Moreover, sextupole magnets are used to suppress the second-order dispersion generated in the quadrupole magnets of the collimator.

Figure 4.2 shows the evolution of the first and second-order dispersion along the collimator section of FLASH. Two horizontally focusing quadrupoles (Q3ECOL and Q5ECOL) and one vertically focusing quadrupole (Q4ECOL) are used. Q3ECOL and Q5ECOL bring the linear dispersion (D_x) to zero in the symmetry point of the collimator (center of Q4ECOL). Q4ECOL is not needed for dispersion suppression but allows controlling the focusing in the vertical plane. On the other hand, two sextupoles of opposite polarity (S2ECOL and S6ECOL) are used to bring the second-order dispersion (D_{xx}) to zero. More detailed information about the suppression of dispersion in the FLASH collimator is in [Bal05].

4.2.3 Design Dispersion at FLASH and the XFEL

Figure 4.3 shows the nominal dispersion for FLASH. There is only non-zero horizontal dispersion in the bunch compressors and the collimator section.

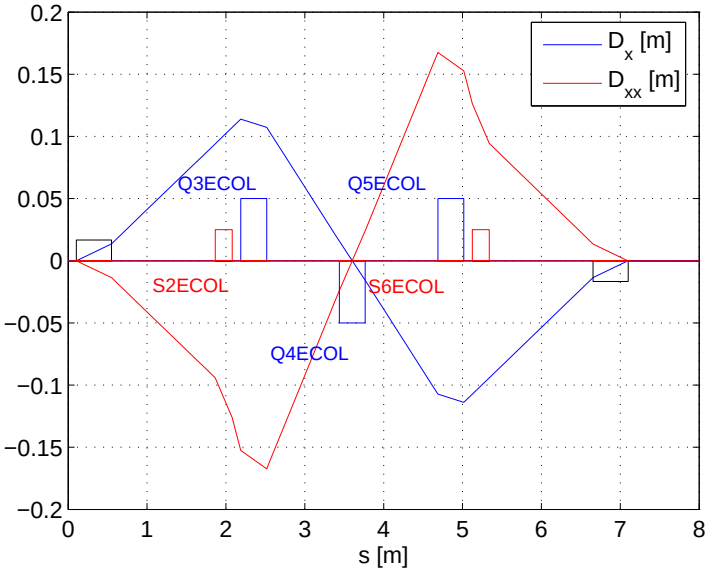

Figure 4.2: Design dispersion at the collimator section of FLASH.

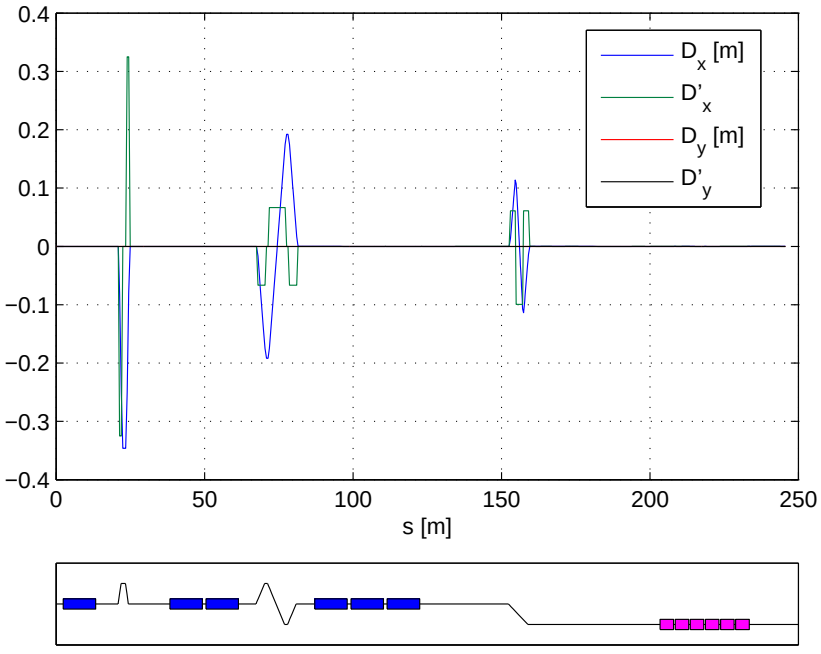

Figure 4.3: Design dispersion along FLASH.

Figure 4.4 shows the design dispersion for the XFEL. The upper plot corresponds to the whole lattice. The rest of the plots correspond to the specific regions with non-zero dispersion: *dog-leg* of the injector section, bunch compression system, collimation and distribution sections. It should be noted that the distribution section refers to the one which goes through the undulators SASE1 and SASE3 (the distribution section corresponding to the undulator SASE2 has been omitted). Except for the arcs in the distribution sections, all the design dispersion for the XFEL is in the vertical plane.

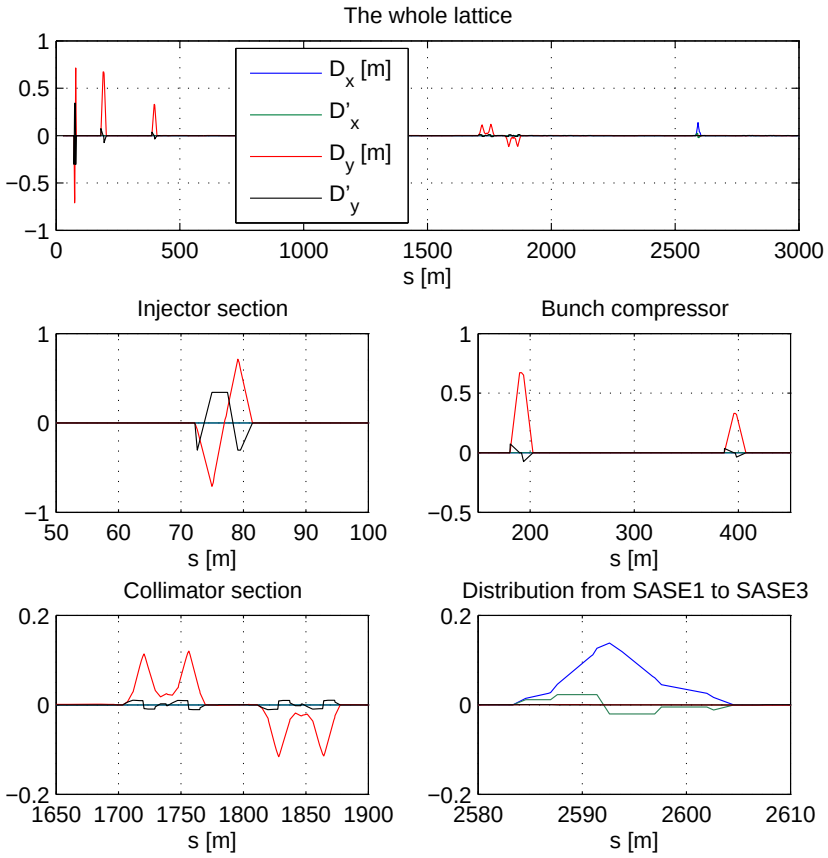

Figure 4.4: Design dispersion along the XFEL.

4.3 Spurious Dispersion Sources

4.3.1 Dipole Field Errors

According to equation 4.1, a dipole field error ΔB of a magnet with length l will produce the following additional deflection:

$$\frac{\Delta\varphi}{l} = \frac{e\Delta B}{p} \tag{4.14}$$

The resulting spurious dispersion is the difference between the dispersion of the magnet with the field error and the nominal dispersion of the dipole:

$$\begin{aligned} D_x &= R_{16}(\varphi_0 + \Delta\varphi) - R_{16}(\varphi_0) \\ D'_x &= R_{26}(\varphi_0 + \Delta\varphi) - R_{26}(\varphi_0) \end{aligned} \tag{4.15}$$

Assuming a sector dipole magnet, the elements of above equation can be calculated using equation 4.2.

In addition to the dispersion generation, the trajectory will be distorted (i.e. the trajectory will not be closed after the bunch compressor or the collimator section).

Figure 4.5 shows an example of spurious dispersion generation due to a dipole field error in the last bending magnet at the second bunch compressor of FLASH. A drift space is assumed downstream.

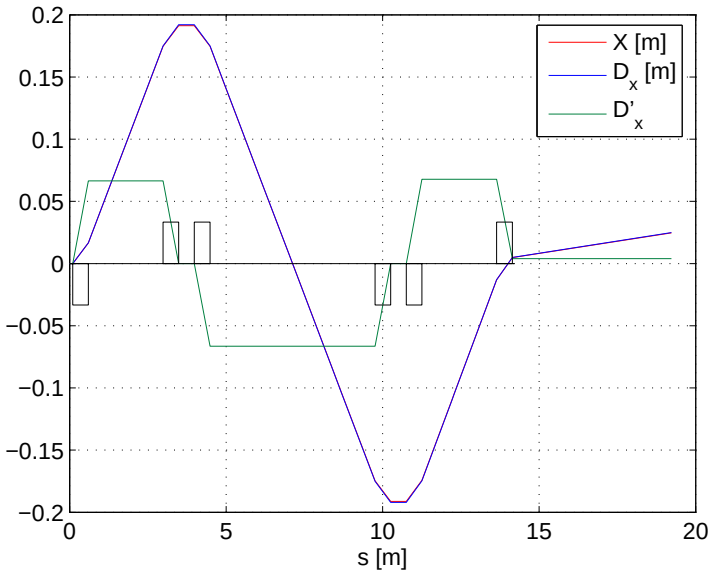

Figure 4.5: Trajectory and dispersion (with reversed sign) through a bunch compressor in which the last bending magnet has a field error.

4.3.2 Trajectory Errors

Due to the non-zero dispersion terms of the second-order matrix T of some lattice elements (i.e. dipoles in the contrary plane of the bending, quadrupoles, and RF cavities), a particle traveling with a certain transverse trajectory offset and angle $(x_0, x_0'; y_0, y_0')$ through such elements will generate the following amount of dispersion:

$$\begin{aligned} D_x &= T_{116} \cdot x_0 + T_{126} \cdot x_0' \\ D_x' &= T_{216} \cdot x_0 + T_{226} \cdot x_0' \\ D_y &= T_{336} \cdot y_0 + T_{346} \cdot y_0' \\ D_y' &= T_{436} \cdot y_0 + T_{446} \cdot y_0' \end{aligned} \tag{4.16}$$

4.3.3 Element Misalignments

An element misalignment $(\Delta x, \Delta y)$ is equivalent to a trajectory offset error (x_0, y_0). To get the dispersion generated by an element misalignment equation 4.16 can be used with $x_0' = y_0' = 0$ and replacing (x_0, y_0) with $(\Delta x, \Delta y)$.

Figure 4.6 shows the trajectory and the dispersion generated (with a reversed sign) of a quadrupole with a horizontal offset.

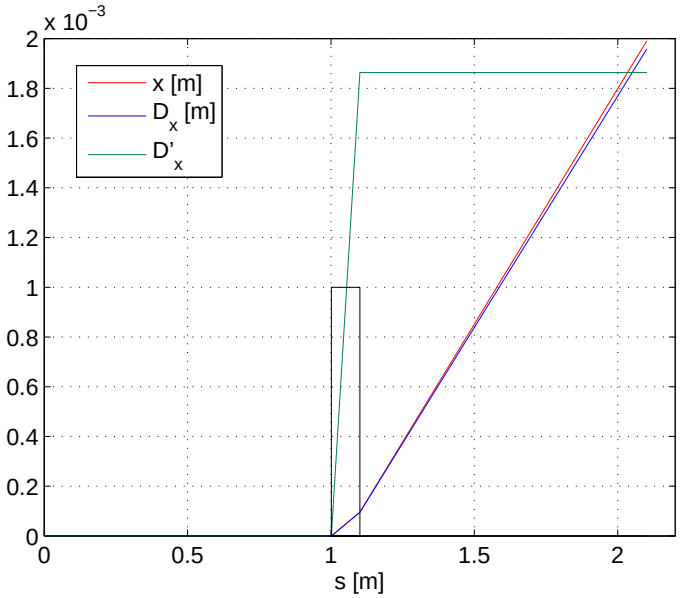

Figure 4.6: Trajectory and dispersion (with reversed sign) generation of a horizontal misaligned quadrupole.

4.3.4 Quadrupole and Sextupole Field Errors at Dispersive Sections

If the strength of the quadrupole magnets used to cancel the dispersion in the collimator sections differs from the nominal value, the first and second-order dispersion are non-zero after the collimator. If the field of the sextupole magnets has an error, the second-order dispersion will be non-zero after the collimator section. In the case of a quadrupole or sextupole field error in a dispersive section, the on-axis beam trajectory is not affected. Figure 4.7 shows the generated spurious dispersion after the collimator section of FLASH due to a field error of a quadrupole and a sextupole magnet. A drift space is assumed downstream of the collimator.

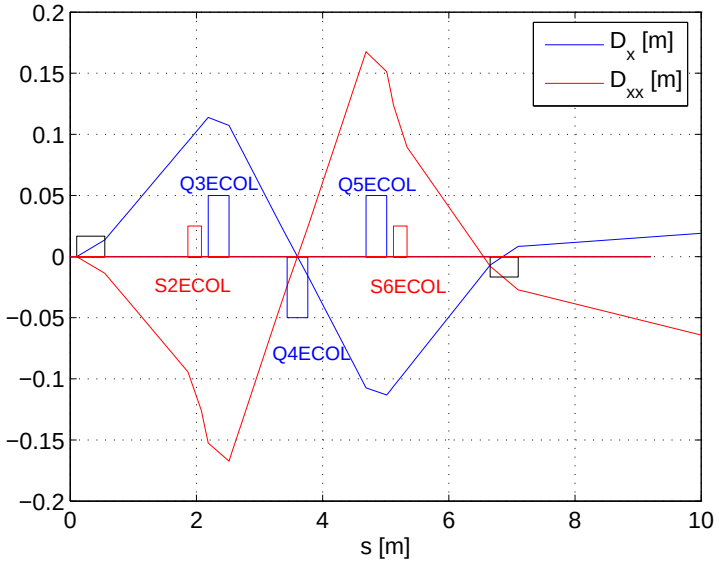

Figure 4.7: Dispersion at the FLASH collimator with quadrupole and sextupole field errors.

In general, any quadrupole or sextupole field in a dispersive section generates first and second-order dispersion. For instance, due to field impurities, the interior bending magnets of the bunch compressors can have a field gradient, which would create non-zero dispersion in the plane of the bending. That happened during the commissioning of the LCLS [1] injector, in which the field of the bunch compressor magnets included a significant quadrupole component generating a large horizontal dispersion beyond the bunch compressor [Emm07].

[1] The Linac Coherent Light Source (LCLS) is a SASE X-ray free-electron laser project presently under construction at the Stanford Linear Accelerator Center (SLAC) [Art02].

4.3.5 Other Sources

In general, any spurious dipole field component in the lattice will be a source of dispersion. This includes for instance the kick produced by the RF couplers of the accelerator modules. The dispersion generated by a dipole field which generates a deflection of an angle φ_{err} and a radius of curvature ρ_{err} can be calculated using equation 4.2:

$$\begin{aligned} D_x &= \rho_{err}(1 - \cos\varphi_{err}) \\ D'_x &= \sin\varphi_{err} \end{aligned} \tag{4.17}$$

4.3.6 Dispersion Propagation

To linearly transport the dispersion functions from s_1 up to s_2 (with $s_2 > s_1$), the following expression is used:

$$\begin{aligned} D_x(s_0, s_2) &= D_x(s_0, s_1)R_{11}(s_1, s_2) + \\ &\quad + D'_x(s_0, s_1)R_{12}(s_1, s_2) + D_x(s_1, s_2) \\ D'_x(s_0, s_2) &= D_x(s_0, s_1)R_{21}(s_1, s_2) + \\ &\quad + D'_x(s_0, s_1)R_{22}(s_1, s_2) + D'_x(s_1, s_2) \end{aligned} \tag{4.18}$$

If no dispersion is generated between s_1 and s_2:

$$\begin{aligned} D_x(s_0, s_2) &= D_x(s_0, s_1)R_{11}(s_1, s_2) + D'_x(s_0, s_1)R_{12}(s_1, s_2) \\ D'_x(s_0, s_2) &= D_x(s_0, s_1)R_{21}(s_1, s_2) + D'_x(s_0, s_1)R_{22}(s_1, s_2) \end{aligned} \tag{4.19}$$

D_y and D'_y can be transported accordingly.

4.4 Sensitivities for FLASH and the XFEL

Simulations have been performed with the program *elegant* [ELE] in order to analyze which of the dispersion generation mechanisms are more important for FLASH and the XFEL. Tables 4.1 and 4.2 show the magnitude of random error required to generate 10 mm of dispersion (RMS) in the undulator section for different imperfections at both accelerators. All the errors are considered separately (i.e. uncorrelated). Presented numbers correspond to average results over 200 seeds. No trajectory correction is performed.

FLASH

For FLASH one case with errors in the entire lattice (starting downstream of the first accelerator module) and one case with imperfections only in the collimator section are considered. All the dipole magnets at FLASH are in the horizontal direction. Since the focusing of horizontal bending magnets is in the vertical direction, only a misalignment of the dipoles in the vertical

Table 4.1: Required amount of error per type and section to generate 10 mm of dispersion in the FLASH undulator.

Error	Entire lattice	Collimator
Quadrupole misalignment	x: 17 µm y: 18 µm	x: 76 µm y: 49 µm
Quadrupole field error	1.31 %	1.31 %
Quadrupole component in dipoles	$4.1{\cdot}10^{-3}$ m^{-2}	-
Vertical dipole misalignment	215 µm	220 µm
Dipole field error	0.13 %	9.2 %
Cavity misalignment	x: 2.0 mm y: 1.8 mm	- -

plane generates dispersion. It should be noted that quadrupole field errors create horizontal dispersion only in the collimator section.

The numbers from Table 4.1 indicate that for FLASH quadrupole misalignments (equivalent to beam trajectory offsets) are the most important spurious dispersion source, and that the collimator section is a critical point in terms of dispersion generation.

XFEL

For the XFEL errors in four different sections have been considered: bunch compressors section (between BC1 and BC2), main linac, collimation section, and one of the undulator sections (SASE1).

From Table 4.2 it can be seen that the amount of errors required to generate 10 mm of dispersion in the undulator section is much lower for the XFEL than for FLASH (for all the different considered imperfections). As in the case of FLASH, the most important dispersion sources are the quadrupole misalignments. The bunch compressor is the most critical section concerning quadrupole misalignments, dipole field errors, and quadrupole field components in dipole magnets.

Table 4.2: Required amount of error per type and section to generate 10 mm of dispersion in the XFEL undulator.

Error	Bunch compressors	Main linac	From collimator to undulator	Undulator SASE 1
Quadrupole misalignment	x: 4 µm y: 5 µm	x: 7 µm y: 8 µm	x: 6 µm y: 6 µm	x: 0.8 mm y: 0.7 mm
Quadrupole field error	-	-	0.5 %	-
Quadrupole component in dipoles	$4.0{\cdot}10^{-4}$ m^{-2}	-	$3.0{\cdot}10^{-3}$ m^{-2}	-
Dipole field error	0.07 %	-	5.5 %	-
Cavity misalignment	x: 280 µm y: 250 µm	x: 2.3 mm y: 2.0 mm	- -	- -

Chapter 5

Dispersion Measurement and Correction

5.1 Dispersion Measurement

Dispersion measurement is based on measuring the orbit for different beam energies[1]. The gradient of the accelerator modules along the machine is scanned and the orbit changes downstream are analyzed.

At FLASH, for the dispersion measurement the energy variation can be done at three different places: ACC1, ACC23, and ACC456 (see Figure 5.1). The beam trajectory for the different energies is measured in BPMs (Beam Position Monitors). FLASH has about 40 BPMs with single bunch resolution between ACC1 and the undulator section. Button-type BPMs are installed in the undulator section and before the first bunch compressor [Noe04] [Lun07]. Stripline BPMs, typically built inside quadrupoles, are found in the rest of the warm parts of the machine [Noe04]. Cavity or reentrant cavity BPMs are mounted in the end of each cryomodule [Lor97] [Sim08]. Information about BPMs resolution and calibration at FLASH can be found in [Bab06] and [Bab07] respectively.

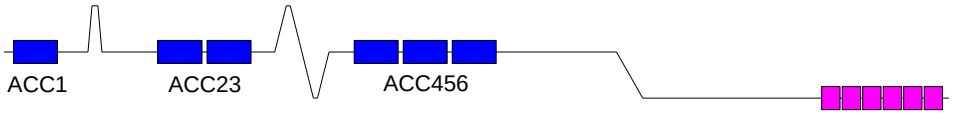

Figure 5.1: Schematic view of FLASH. For dispersion measurements, the electron energy can be varied at ACC1, ACC23 and ACC456.

[1]For our electron energy range the relative momentum deviation $\delta = \Delta p/p_0$ is practically equal to the relative energy deviation $\Delta E/E_0$.

5.1.1 RF Steering Compensation

As it has been seen in Chapter 4, an RF cavity can be treated as a quadrupole magnet with an equivalent strength that increases with the RF gradient. A beam traveling off-axis through an RF cavity will experience a kick proportional to the accelerator gradient. In addition, the deflections caused by the couplers of the accelerator module (even when the beam goes on-axis) depend linearly on the RF gradient of the module. Due to both effects, when the RF gradient of an accelerator module is changed, the beam experiences a transverse kick proportional to the gradient change.

An orbit correction has to be performed in order to compensate this deflection - otherwise this effect would distort the dispersion measurement. Two correctors in each direction are used to restore the orbit in two BPMs just downstream of the module (see Figure 5.2). In principle, the magnets between the BPMs have to be scaled with beam energy while restoring offset and angle at the second BPM [Cas98], but in most practical situations this effect can be neglected.

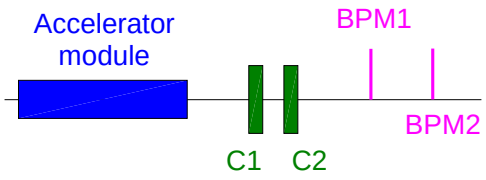

Figure 5.2: Sketch of the RF steering correction during a dispersion measurement.

At FLASH the RF steering effect is only significant at the first cavities of ACC1. The RF kick generated at the first cavity of ACC1 when the gradient is changed by 1 MV/m can be calculated as an example. For this, the RF kick produced by the coupler is neglected and a cavity misalignment of 1 mm is assumed:

$$RF_{kick} = k_{cav} l \cdot \Delta_{cavity} \approx 25 \text{ µrad}$$

where k_{cav} has been calculated using equation 4.9 assuming that the electrons are accelerated from 5 to 20 MeV in the first cavity of ACC1. For the rest of the accelerator modules, since the electron energy is big enough, the RF steering effect is practically negligible.

5.1.2 Dispersion Derivation

The horizontal and vertical-orbit readings downstream of the second BPM used for RF steering correction can be expressed up to second order as:

$$\begin{aligned} x(s) &= x_0(s) + D_x(s_0, s) \cdot \delta(s_0) + D_{xx}(s_0, s) \cdot \delta^2(s_0) \\ y(s) &= y_0(s) + D_y(s_0, s) \cdot \delta(s_0) + D_{yy}(s_0, s) \cdot \delta^2(s_0) \end{aligned} \tag{5.1}$$

where $\delta = \Delta p/p_0$ is the relative momentum (or energy) deviation induced in the accelerator module, s_0 is the position of the second BPM used for the RF steering correction after the module, and s the position of any other BPM. The horizontal and vertical trajectories (x_0 and y_0) as well as the first and second-order dispersion functions (D_x, D_y, D_{xx}, D_{yy}) are obtained making a second-order polynomial fit to the BPM data in a least-squares sense[2](see Figure 5.3).

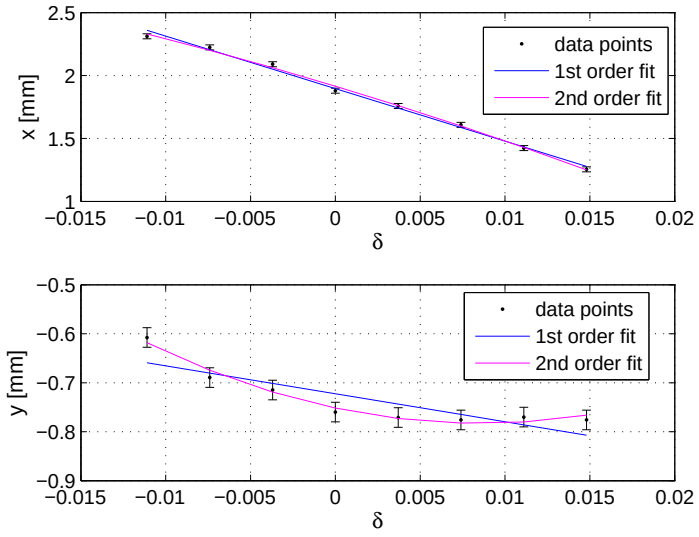

Figure 5.3: Example of a dispersion measurement at a single BPM at FLASH. Upper plot: horizontal plane. Lower plot: vertical plane. Measurement points as well as first and second-order fits are indicated.

In our case the linear dispersion functions (D_x and D_y) are defined as the first-order terms of the second-order polynomial fit. In this way, the slope at $\delta = 0$ is obtained - instead of the slope of the whole set of data that would be obtained doing a linear fit. The interest is focused on measuring

[2]The best fit in the least-squares sense is that instance of the model for which the sum of squared residuals has its least value, a residual being the difference between the measured value and the value given by the model. Information about how to fit data in a least-squares sense can be found for instance in [Pre92].

and correcting the dispersion close to $\delta = 0$, since the total energy range for the dispersion measurement is usually significantly bigger than the energy spread of the beam.

The measured dispersion is the one which is generated between s_0 and s. Therefore, when selecting the second BPM used for RF trajectory compensation (i.e. s_0), one chooses the region where the measured dispersion is generated (downstream of s_0). Typically the correction is applied just downstream of the accelerator module, so the measured dispersion is the one created from downstream of the module up to the rest of the machine. To measure the dispersion generated in some specific part of the lattice, the trajectory compensation should be done exactly in front of that region.

5.1.3 Dispersion Measurement Errors

Uncertainties in the dispersion measurement include both statistical and systematic errors. Although both types of errors are estimated, the measurements presented in this thesis only consider statistical errors.

Statistical Errors

Let's call σ_{x_i} the orbit uncertainties of each measurement step. Assuming that the relative energy deviations per each measurement step δ_i are well known, the statistical uncertainty of the dispersion measurement σ_{D_x} can be calculated as follows [Pre92]:

$$\sigma_{D_x} = \sqrt{\frac{\sum_i \frac{1}{\sigma_{x_i}^2}}{\sum_i \frac{1}{\sigma_{x_i}^2} \cdot \sum_i \frac{\delta_i^2}{\sigma_{x_i}^2} - (\sum_i \frac{\delta_i}{\sigma_{x_i}^2})^2}} \tag{5.2}$$

The dispersion error depends on the trajectory uncertainties, the total energy range of the measurement, and the number of steps into which the measurement is divided. Figure 5.4 shows dispersion uncertainties versus trajectory errors for different energy ranges and number of steps. As it can be seen from the figure, increasing the total energy range of the measurement is more efficient than simply increasing the number of steps.

At FLASH, the orbit is measured for different number of shots - typically between 20 and 50 times. The average and the standard deviation of the whole set of measurements give respectively the final orbit and its corresponding uncertainty. Trajectory measurement errors depend on the BPM resolution and the beam orbit jitter. BPM resolution stays typically between 5 µm and 20 µm for all the different BPM types [Bab06]. Trajectory jitter comes from different sources like the laser or the different RF stations.

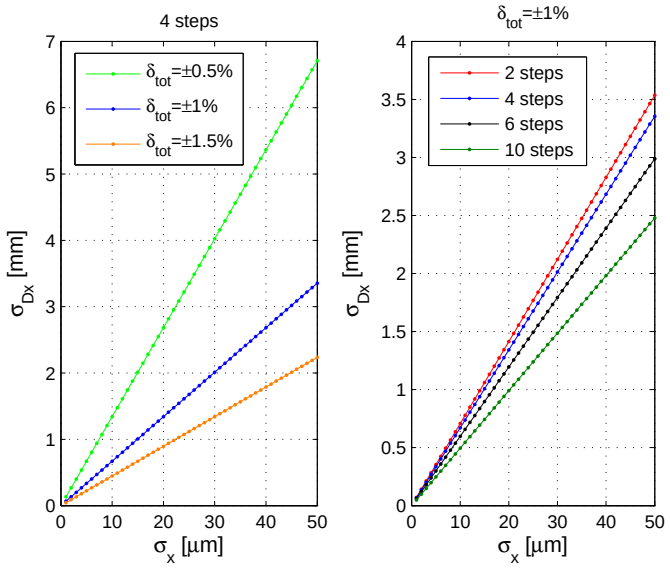

Figure 5.4: Dispersion uncertainties σ_{D_x} as a function of trajectory uncertainties σ_x. Left plot: evolution for different energy ranges (the number of steps is fixed at 4). Right plot: evolution for different number of measurement steps (the total energy range is $\pm 1\,\%$).

The final trajectory error stays usually between 20 µm and 50 µm, which is dominated by the trajectory jitter. For a typical measurement $\delta_{tot} \sim \pm 1\,\%$ and $\#_{steps} \geq 3$. Therefore, dispersion statistical uncertainties are usually in the order of 1-3 mm (see Figure 5.4). It should be noted that δ_{tot} usually cannot be bigger than $\sim \pm 1\,\%$ due to beam losses, limiting the dispersion measurement accuracy.

Systematic Errors

The following systematic errors can contribute to the distortion of the dispersion measurement:

- **RF steering.** This effect is only significant at ACC1 and is compensated by an orbit correction (see subsection 5.1.1).
- **Calibration errors for δ.** At FLASH the energy can be obtained using three different methods: from the RF probes of the cavities (this is used for the dispersion measurement), from the *energy server* which uses the collimator section as a magnetic spectrometer, and by calculating the electron energy from the FEL radiation spectrum measured with the radiation spectrometer of FLASH [Nic05].

  Recent studies compared the values obtained from all methods for

three different energies [Kam09]. The error of the relative momentum deviation δ as measured by the probe signals can be estimated as:

$$\text{err} = \delta_{true} - \delta$$

where δ_{true} is the relative momentum deviation measured with the magnetic or the radiation spectrometer. For typical dispersion measurements with $\delta = 1\%$, the estimated error is 0.10 % according to the energy server and 0.24 % according to the radiation spectrometer.

- **BPM calibration errors.** BPM calibration errors are in the order of 5 % [Bab09]. Therefore, dispersion measurement error due to BPM calibration errors is approximately 5 %.
- **BPMs nonlinearities.** The linear range for a zero beam offset in the orthogonal plane is roughly 1/3 of the beam pipe [Bab07]. Therefore, the most critical part in FLASH is the undulator, in which the diameter of the beam pipe (9 mm) is smaller than in the other regions (mostly 44 mm). As measured with correctors, the linear range in the undulator is usually ±1 mm [Bab09a]. For a typical measurement with $\delta = \pm$ 1 %, this allows measuring correctly the dispersion up to values of ±100 mm (provided that the on-energy beam travels on-axis and that the BPM offset is zero)[3], which in most of the cases is sufficient for the measurement of spurious dispersion at FLASH.
- **Trajectory and energy drifts.** A trajectory or beam energy drift during the dispersion measurement would distort the result. Taking into account that the dispersion measurement is usually done in less than one minute, these effects can be usually neglected.

The systematic errors are dominated by BPM calibration errors and are overall estimated by about 6 %.

5.1.4 Examples of Measurements at FLASH

Figures 5.5 and 5.6 show two examples of dispersion measurement along FLASH done on two different days. Both measurements were done changing the energy at ACC1, and the measurement in Figure 5.6 was done under SASE conditions. The first measurement (Figure 5.5) shows an RMS dispersion of 36 mm in the horizontal plane and more than 400 mm in the vertical one, while the RMS dispersion in the undulator for the second measurement (Figure 5.6) was about 200 mm in the horizontal plane and 26 mm in the vertical one. These two measurements serve as an example to illustrate that spurious dispersion depends on the operating conditions of the machine. As a consequence, it is obvious that dispersion must be measured and corrected frequently.

[3] $D = \Delta x/\delta = \pm 1$ mm/± 1 % = ± 100 mm

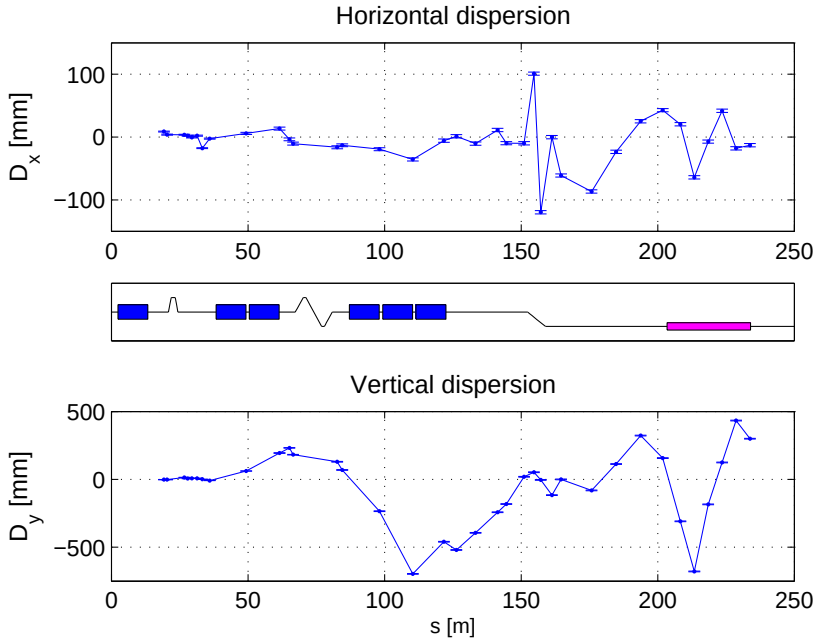

Figure 5.5: Dispersion measurement from ACC1 - Day 1.

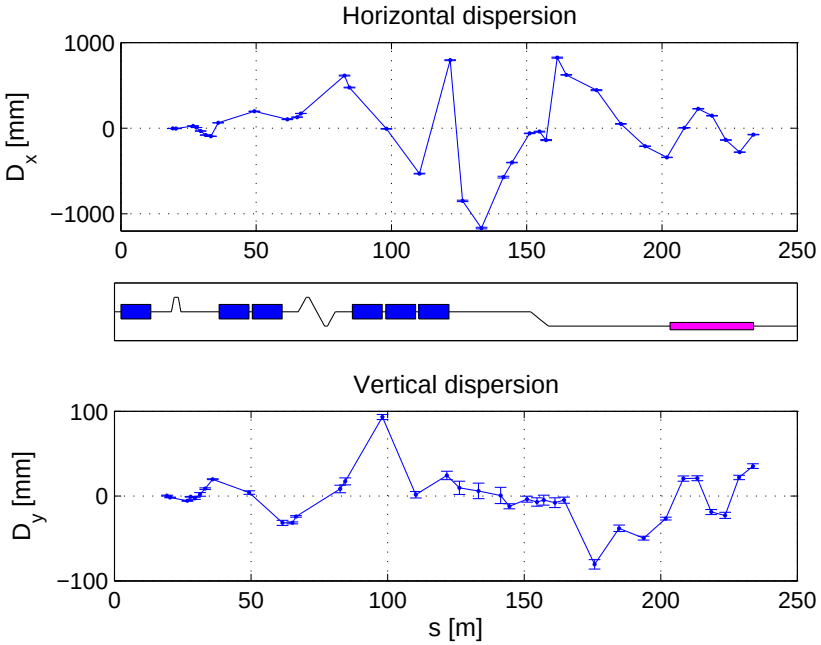

Figure 5.6: Dispersion measurement from ACC1 - Day 2 (SASE conditions).

5.2 Dispersion Correction Algorithm

The algorithm presented in this section can simultaneously correct both trajectory and dispersion using dipole correctors and quadrupole movers [Clo78] [Rau91] [Kei04]. In addition, the quadrupoles in the collimator section can be used to correct the horizontal dispersion. At FLASH there are about 30 corrector coils per plane along the machine (from ACC1 up to the undulator) as well as 15 quadrupole movers in the collimator and undulator sections which are used to perform the correction.

The optimal settings are calculated using the orbit and dispersion response matrices, the terms of which are defined as the shift of the orbit or dispersion due to a change of the corrector strength:

$$OR_{i,j} = \frac{\Delta u_i}{\Delta \Theta_j} \qquad DR_{i,j} = \frac{\Delta D_i}{\Delta \Theta_j} \tag{5.3}$$

where Δu_i and ΔD_i is the change of the orbit and the dispersion at the BPM i, and $\Delta\Theta_j$ is the change of the strength of the corrector j.

The induced orbit and dispersion due to a change in corrector strength is given by:

$$\begin{pmatrix} \hat{OR} \\ \hat{DR} \end{pmatrix} \cdot \vec{\Delta\Theta} = \begin{pmatrix} \vec{u}_{ind} \\ \vec{D}_{ind} \end{pmatrix} \tag{5.4}$$

where $\vec{\Delta\Theta}$ is the vector of corrector strengths, and $\vec{u}_{ind}$ and $\vec{D}_{ind}$ are respectively the induced orbit and dispersion.

The goal is to find a set of corrector strength which minimizes in a least-squares sense the difference between the final orbit and the dispersion with respect to some desired values (i.e. with respect to the *golden* values):

$$(1-w) \cdot \|\vec{u}_{meas} + \vec{u}_{ind} - \vec{u}_{gold}\|^2 + w \cdot \|\vec{D}_{meas} + \vec{D}_{ind} - \vec{D}_{gold}\|^2 = \min \tag{5.5}$$

where the subindex *meas* refers to the measured values and the subindex *gold* refers to the final desired orbit and dispersion. w is a factor between 0 and 1 that defines the relative weight for the orbit and the dispersion correction. For $w = 0$ only the orbit is corrected; for $w = 1$ only the dispersion is corrected; for $w = 0.5$ orbit and dispersion are corrected with the same weight.

The algorithm uses SVD (Singular Value Decomposition) to find a corrector set that minimizes equation 5.5. SVD is a well-known technique which allows a fine balancing of the competing demands of minimizing the trajectory, the dispersion, and the corrector strengths simultaneously. SVD identifies redundant corrector magnets combinations so that they can be removed from the correction algorithm. Details about the SVD can be found in [Pre92].

Orbit and Dispersion Response Matrices

The orbit and the dispersion response for a corrector coil or quadrupole mover depend on the optics of the machine. One possibility to obtain them is to directly measure the orbit and dispersion variations at the BPMs when the corrector currents are changed or the quadrupole movers are displaced. This would minimize the impact of most of the machine unknowns and imperfections - such as energy uncertainty, quadrupole and corrector field errors, etc. However, this is not very practical since it requires a significant amount of time for performing the measurements, cycling the magnets after their response is measured, etc.

A more convenient way to obtain the response matrices is to calculate them from the quadrupole currents and the estimated energy along the machine. In this case, energy uncertainties, quadrupole and corrector field errors, and magnet calibration errors will deteriorate the agreement between the real and the calculated matrices. Moreover, any real effect which is not taken into account in the calculation will affect negatively the results.

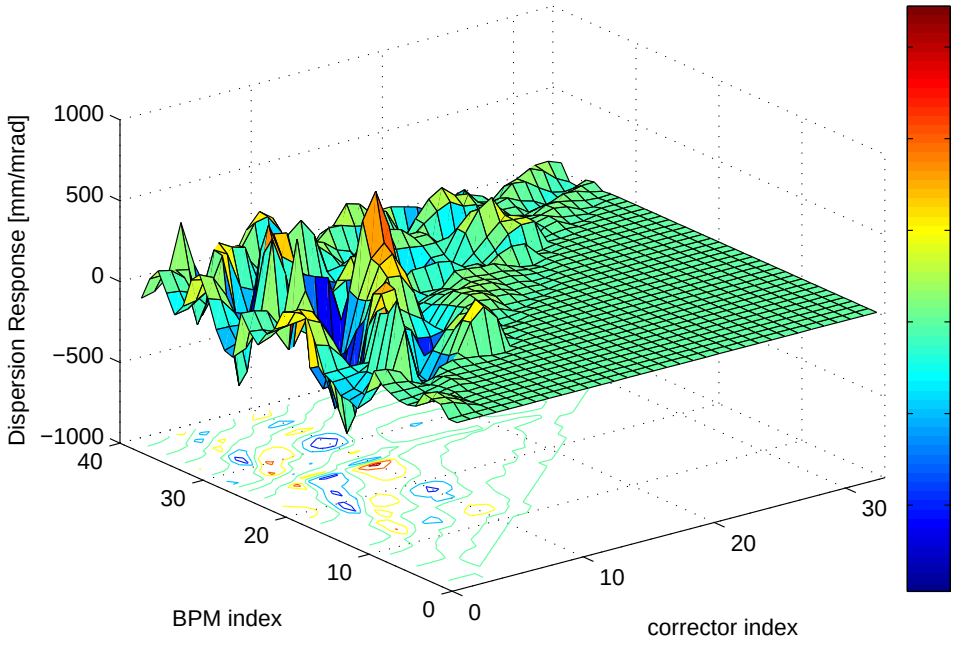

Figure 5.7: Horizontal dispersion response matrix for 1 GeV at FLASH. Values are calculated using the design optics for this energy.

The corrector responses can be obtained like in a measurement, tracking a particle and observing the orbit and dispersion response at the BPMs due to a change of a corrector strength. Alternatively, they can also be obtained

in a simpler way directly from the transfer matrices between the correctors and the BPMs:

$$\begin{aligned} OR_{x_{i,j}} &= \frac{\Delta x_i}{\Delta \Theta_j} = R_{12_{j\to i}} & OR_{y_{i,j}} &= \frac{\Delta x_i}{\Delta \Theta_j} = R_{34_{j\to i}} \\ DR_{x_{i,j}} &= \frac{\Delta D_{x_i}}{\Delta \Theta_j} = T_{126_{j\to i}} & DR_{y_{i,j}} &= \frac{\Delta D_{y_i}}{\Delta \Theta_j} = T_{346_{j\to i}} \end{aligned} \tag{5.6}$$

Figure 5.7 shows the design horizontal dispersion response for FLASH corresponding to an electron energy of 1 GeV.

The difference between the calculated and the measured response matrices can be used to determine possible machine imperfections like magnet field errors and BPM calibration errors. This has been done using programs like CALIF [Cor93] [4] or LOCO [Saf97] [5].

5.3 Dispersion Tool at FLASH

The whole dispersion correction process consists of four steps (see Figure 5.8):

1. Measure the orbit for different energies.
2. Derive average orbit and dispersion.
3. Apply correction algorithm using the orbit and dispersion response matrices.
4. Set the currents to the correctors and the displacements to the quadrupole movers.

In a real machine, these four steps have to be iterated to overcome optics imperfections, correctors calibration errors and BPM imperfections.

Based on the procedure shown in Figure 5.8, a software application to measure and correct both the orbit and the dispersion has been developed at FLASH. More detailed information can be found in Appendix C.

Using this application, the dispersion measured from all accelerator modules (ACC1, ACC23 or ACC456) can be kept below 5 mm (RMS) in both planes. This limitation is determined by the dispersion measurement error (usually between 1 mm and 3 mm, as previously said) and the response matrices errors, which depend on the optics.

The speed of the convergence is a qualitative indicator of how close our model is with respect to the real machine. It depends on the optics imperfections and on the corrector and BPM calibration errors. The convergence

[4] For instance at HERA at DESY [Hof02].

[5] For instance at PEP-II at the Stanford Linear Accelerator Center(SLAC) [Ste04].

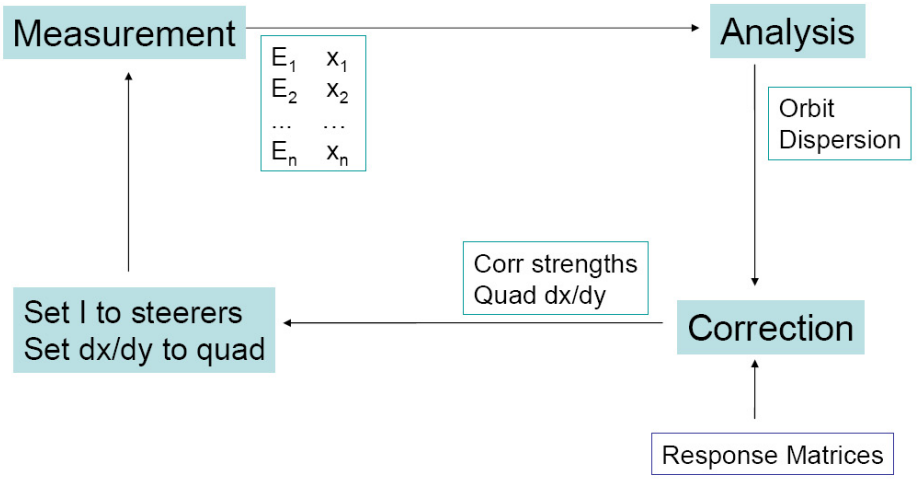

Figure 5.8: Scheme for dispersion correction procedure.

for the dispersion correction is usually reached with four or five iterations, in which typically between 50 and 75 % of the proposed corrections by the algorithm are applied.

5.3.1 Example of Simulations

Figure 5.9 shows an example of a simulation of a global correction (i.e. correction in all BPMs) using all the available correctors in the machine. The simulation takes into account the following machine imperfections: 100 µm quadrupole misalignment, 1 % of dipole and quadrupole field errors, a BPM noise of 20 µm, and BPM offsets of 100 µm (all numbers RMS). The upper and middle plots show orbit and dispersion along the machine before and after correction. The lower plot displays the change in corrector strengths and quadrupole mover positions required to perform the correction.

In this example the RMS dispersion is reduced from 37 mm to 11.5 mm. Local correction in the undulator using the correctors downstream of the collimator yields a final RMS dispersion of less than 5 mm in both planes.

5.3.2 Examples of Measurements

Figure 5.10 shows an example of a correction of horizontal dispersion measured from ACC1. The beam was dumped upstream of the collimator section. The orbit was kept constant downstream of the BC3 and the RMS dispersion was reduced from 30 mm to 5 mm. Correction in the other plane gave similar results.

Figure 5.11 shows an example of a dispersion measurement and a correction in the vertical plane. The beam energy was varied in ACC456. The

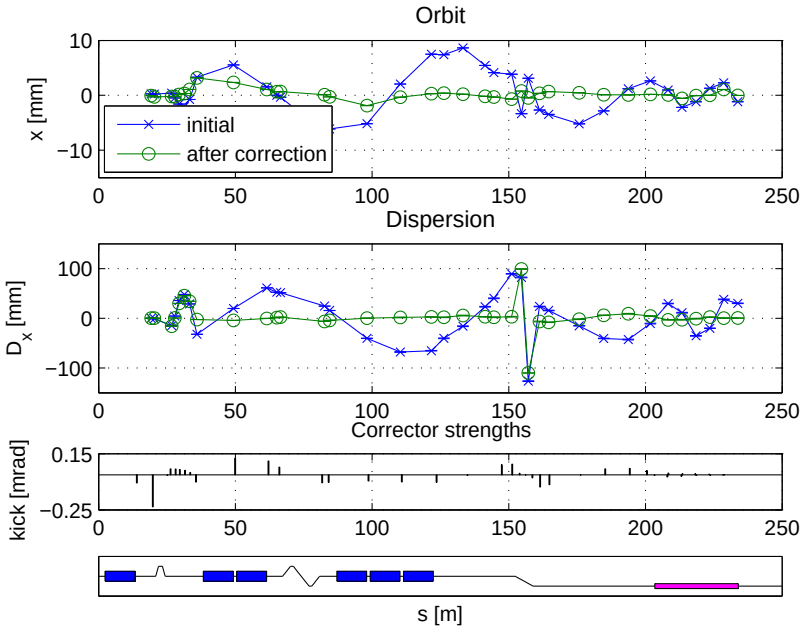

Figure 5.9: Example of simulated horizontal dispersion correction at FLASH (from ACC1).

dispersion in the undulator was corrected while keeping the orbit constant (in order to not lose SASE). The RMS dispersion was reduced from 17 mm to 4 mm after four iterations.

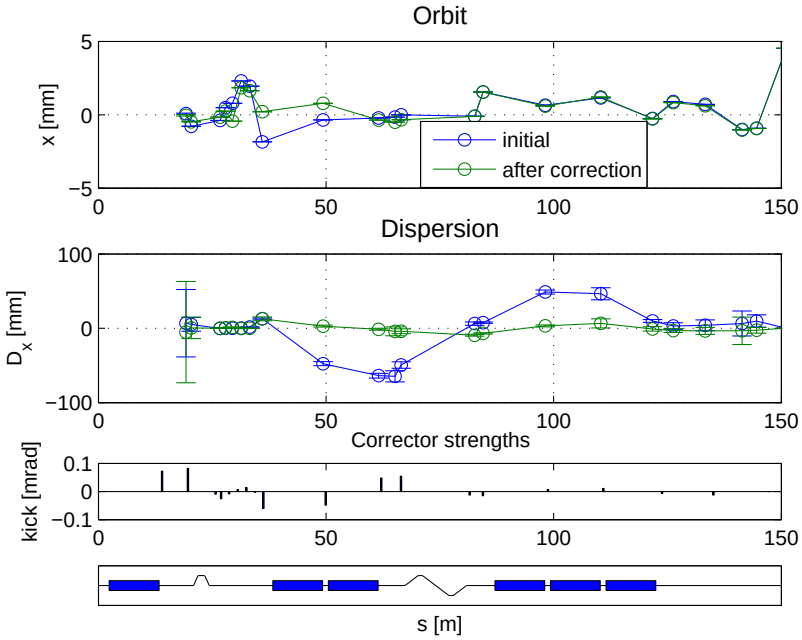

Figure 5.10: Example of a horizontal dispersion correction at FLASH (from ACC1).

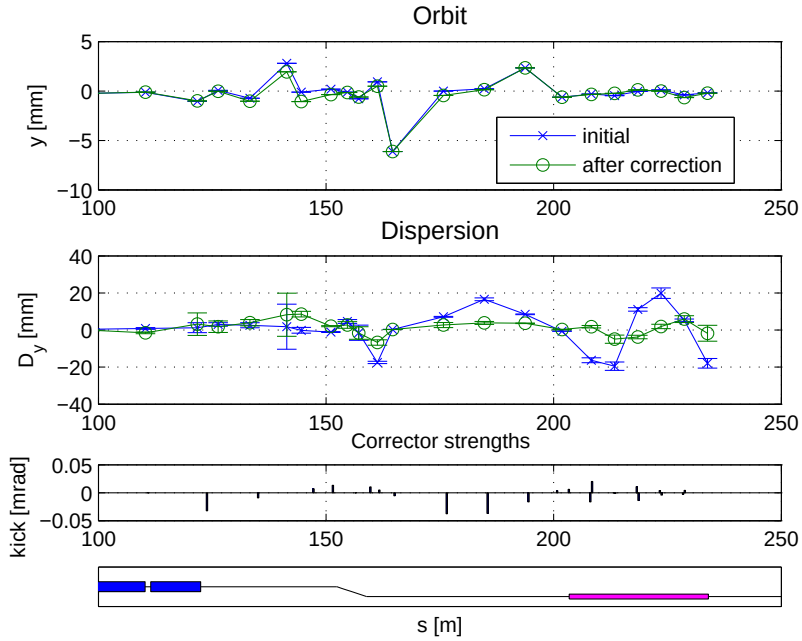

Figure 5.11: Example of a vertical dispersion correction at FLASH (from ACC456).

Chapter 6

Transverse Beam Quality at FLASH

6.1 Introduction

As discussed in Chapter 2, the FEL process requires a high transverse electron beam quality. Small beam sizes and emittances are needed in the undulator section, for which both optimization in the injector and beam quality preservation along the linac are required. The following Section 6.2 describes how the transverse beam distribution is characterized at FLASH.

In the injector area, the laser, the gun (gradient, phase, solenoid), and the electron trajectory have to be adjusted and controlled to have optimal initial conditions. Studies on how vertical trajectory deviations in the injector section turn into dispersion and degrade the beam quality are presented in Section 6.3.

Concerning the transport from ACC1 up to the undulator area, different effects can contribute to the deterioration of the beam quality: dispersion, transverse wakefields of the RF modules and other components like collimators, coupler kicks of the accelerator modules, and other collective effects like coherent synchrotron radiation (CSR) in the bunch compressors[1] and transverse space charge. Among all the effects which degrade the transverse beam distribution, this chapter treats the aspects related directly to beam steering:

- **Dispersion.** As described in Chapter 3, dispersion causes an increase of the effective beam size and emittance. Analysis of the impact of the dispersion on the transverse beam quality in the undulator is presented in Section 6.4.

[1] Information about measurements and analysis of CSR effects at FLASH can be found in [Beu07].

- **Electromagnetic fields in TESLA RF modules.** Coupler kicks and wakefields of the TESLA modules are potential sources for the degradation of the transverse beam quality. Detailed studies on these effects are presented in Section 6.5.

6.2 Beam Size and Emittance Measurements at FLASH

6.2.1 Transverse Beam Diagnostics

Transverse beam profiles are measured using optical beam profile monitors and wirescanners. There are presently 27 optical beam profile monitors mounted along the FLASH linac. Three of them, located in the RF gun area where the electron beam energy is low (∼5 MeV), detect the light emitted by Ce:YAG screens. The other 24 monitors are based on optical transition radiation (OTR). Twelve of the OTR monitors are combined with wirescanners. Detailed information about the OTR screens can be found in [Hon03] and [Cat05]. In addition, there are seven wirescanner stations in the undulator section [Hah08]. Moreover, there is a synchrotron radiation monitor installed behind the third dipole of the first bunch compressor which can be used to measure the transverse beam projections at the entrance of the third dipole [Ger07].

Figure 6.1 shows the location of OTR and wirescanner stations from the first accelerator module down to the undulator section, as well as the dedicated locations for emittance measurements at FLASH. Figure 6.2 shows a sketch of the undulator section, indicating the wirescanner stations.

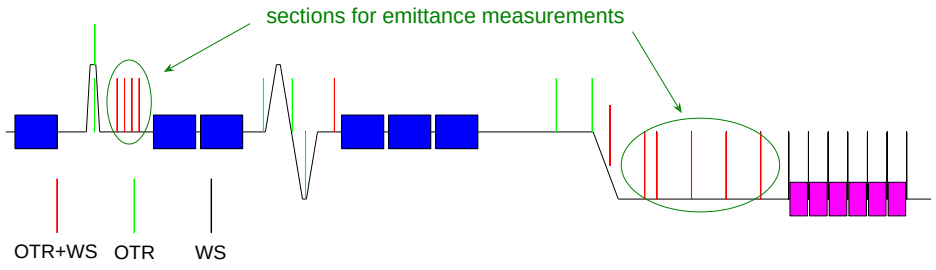

Figure 6.1: Locations of OTR monitors, wirescanners (WS), and dedicated areas for emittance measurements at FLASH.

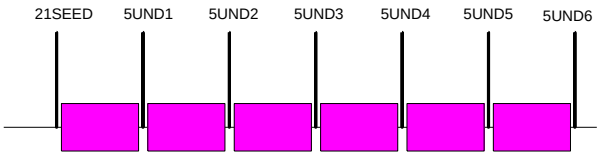

Figure 6.2: Sketch of the undulator section of FLASH.

6.2.2 Emittance Calculation

For the emittance determination only the equations in the horizontal plane are described (considerations in the vertical plane are equivalent). The beam matrix (equation 3.10) can be transported from an initial position s_0 to s according to the following equation:

$$\sigma_{xx}(s) = R_x(s_0, s) \cdot \sigma_{xx}(s_0) \cdot R_x^T(s_0, s) \tag{6.1}$$

where $R_x(s_0, s)$ is the horizontal transfer matrix between s_0 and s:

$$R_x(s_0, s) = \begin{pmatrix} R_{11}(s_0, s) & R_{12}(s_0, s) \\ R_{21}(s_0, s) & R_{22}(s_0, s) \end{pmatrix} \tag{6.2}$$

From equations 6.1 and 3.10 the beam size at a certain position s_i can be expressed as follows:

$$\begin{aligned} \sigma_x^2(s_i) =& R_{11}^2(s_0, s_i) \cdot \sigma_x^2(s_0) + R_{12}^2(s_0, s_i) \cdot \sigma_x'^2(s_0) + \\ & 2 \cdot R_{11}(s_0, s_i) \cdot R_{12}(s_0, si) \cdot \sigma\sigma_x'(s_0) \end{aligned} \tag{6.3}$$

By measuring the beam size at least at three different positions s_i, the beam size, the beam divergence, and the beam coupling term can be reconstructed at s_0 if the transfer matrices between s_0 and s_i are known. The emittance and the Twiss parameters can be then obtained using equations 3.11 and 3.12. It is preferable to measure the beam sizes at more than three different locations and then to find a solution for the beam matrix elements which fits the measured data in a least-squares sense.

The statistical errors of the emittance and Twiss parameters are obtained by error propagation of the beam size measurement statistical uncertainties. Systematic errors include energy uncertainties, optics errors, and the mismatch between the real and the design optics. The optics mismatch is quantified with the so-called *mismatch parameter* [Min03]:

$$M = \frac{1}{2}(\beta\gamma_d - 2\alpha\alpha_d + \gamma\beta_d) \tag{6.4}$$

where the subscript d denotes the design values. For a matched beam the mismatch parameter is $M = 1$. It should be noted that the error bars of the

emittance measurements presented in this thesis only consider the statistical errors of the beam size measurements.

A detailed description of the emittance measurement procedure and error analysis can be found in [Loe05].

There are two dedicated places for measurements of projected emittance at FLASH (see Figure 6.1). The first one is after the first bunch compressor (∼130 MeV) and consists of a FODO lattice [2] with four OTR screens and wirescanner stations, referred to as the *BC* section. The second one is placed between the collimator and the undulator (full beam energy). In this location, referred to as the *seed* section, there is a FODO lattice with four OTR and wirescanner stations. In addition, a fifth station placed upstream of the FODO lattice can be used for the emittance measurements. The seven wirescanner stations placed between the undulator segments allow multi-monitor emittance measurements in this section.

For the measurements with OTR screens, emittance values corresponding to the 90 % of the beam intensity are obtained in addition to the emittances of the entire beam. The intensity cut is performed in the (two-dimensional) image by removing the lowest intensity tails.

6.2.3 Optics Matching

The matching of the Twiss parameters is very important for accurate emittance measurements and for ensuring that the optics are close to the design values. To match the Twiss parameters to the design values, first an initial emittance measurement is performed. From this measurement the Twiss parameters at the first screen or the wirescanner are obtained. The Twiss parameters are then back-tracked upstream and a new optics is calculated to obtain the matched Twiss parameters. When starting with a mismatched beam, two or three iterations are usually necessary to obtain a well matched beam, because not only the error of the measured emittance may be large but also the error of the Twiss parameters.

Matching in the undulator is more complicated than in the BC or the seed section. This is because the calculation of the emittance and Twiss parameters in the undulator is numerically not well-conditioned. For typical operation settings the condition number[3] in the undulator section is an order of magnitude larger than at the BC [Bal07]. This means that the same error of the measured beam sizes leads to errors one order of magnitude bigger in

[2] A FODO lattice is a periodic sequence of focusing (F) and defocussing (D) quadrupole magnets, with drift spaces or dipole magnets (0) between them.

[3] The condition number of a matrix measures the sensitivity of the solution of a system of linear equations to errors in the data. It is defined as the maximum ratio of the relative error in the solution divided by the relative error in the data. In our case the data are the beam size measurements and the solutions are the second moments of the beam (i.e. the beam size, the beam divergence and the beam coupling term). Information on how to calculate the condition number can be found for instance in [Pre92].

the determination of the second moments of the beam (used for calculation of emittance and Twiss parameters).

6.2.4 Saturation of Photomultipliers in the Undulator

Three different wires can be used for each of the seven wirescanner stations in the undulator section: 50 µm tungsten, 10 µm tungsten and 10 µm carbon.

The interaction of the electron bunch with the wire produces highly energetic radiation, which is detected with scintillation counters. The output light power going out from the scintillator is roughly proportional to $d^2 \cdot Z^2 \cdot A^{-1}$, where d is the wire diameter, and Z and A are the atomic and mass number of the wire material[4]. Therefore, the input light power going to the photomultiplier for the 50 µm tungsten wire is 25 times larger than for the 10 µm tungsten wire and about 250 larger than for the 10 µm carbon wire. Due to this fact, the photomultiplier has a non-linear response when tungsten wires are used, leading to an increase of the measured beam sizes and therefore to an increase of the calculated emittance. See Figure 6.15 for an illustration of the effect.

Grey filters with an attenuation factor of 32 were installed in front of the photomultipliers in order to overcome this problem. To check the functionality of the filters, the beam size was measured at one station (WSUND4), using the three different wires with and without the filters. From the measurements shown in Figure 6.3 [Cas07] it can be observed:

1. The beam sizes measured by the different wires are similar when the filters are installed.

2. Without the filters, the beam size obtained from the tungsten wires is bigger than the one from the carbon wire. For instance, the horizontal beam size is up to three times bigger with the 50 µm tungsten wire, which is equivalent to a factor of nine in terms of emittance.

3. The beam size measured with the carbon wire is similar with and without the filters.

These results show that without the filters the beam size measured by the tungsten wires is artificially increased, and that the attenuation filters work as expected. As a consequence, all three available wires can be used for future beam size and emittance measurements in the undulator as long as the gray filters are in place.

[4]The energy loss of one electron hitting the wire is mainly due to bremsstrahlung and proportional to $d \cdot Z^2 \cdot A^{-1}$. Taking into account that the wire diameter is smaller than the beam size, one assumes that the number of electrons hitting the wire is proportional to the wire diameter. Consequently, the energy loss of the whole electron bunch is approximately proportional to $d^2 \cdot Z^2 \cdot A^{-1}$. Finally, it is assumed that the number of particles going into the scintillator, and therefore the light power going out from it, is proportional to the energy loss of the electron bunch (i.e. proportional to $d^2 \cdot Z^2 \cdot A^{-1}$).

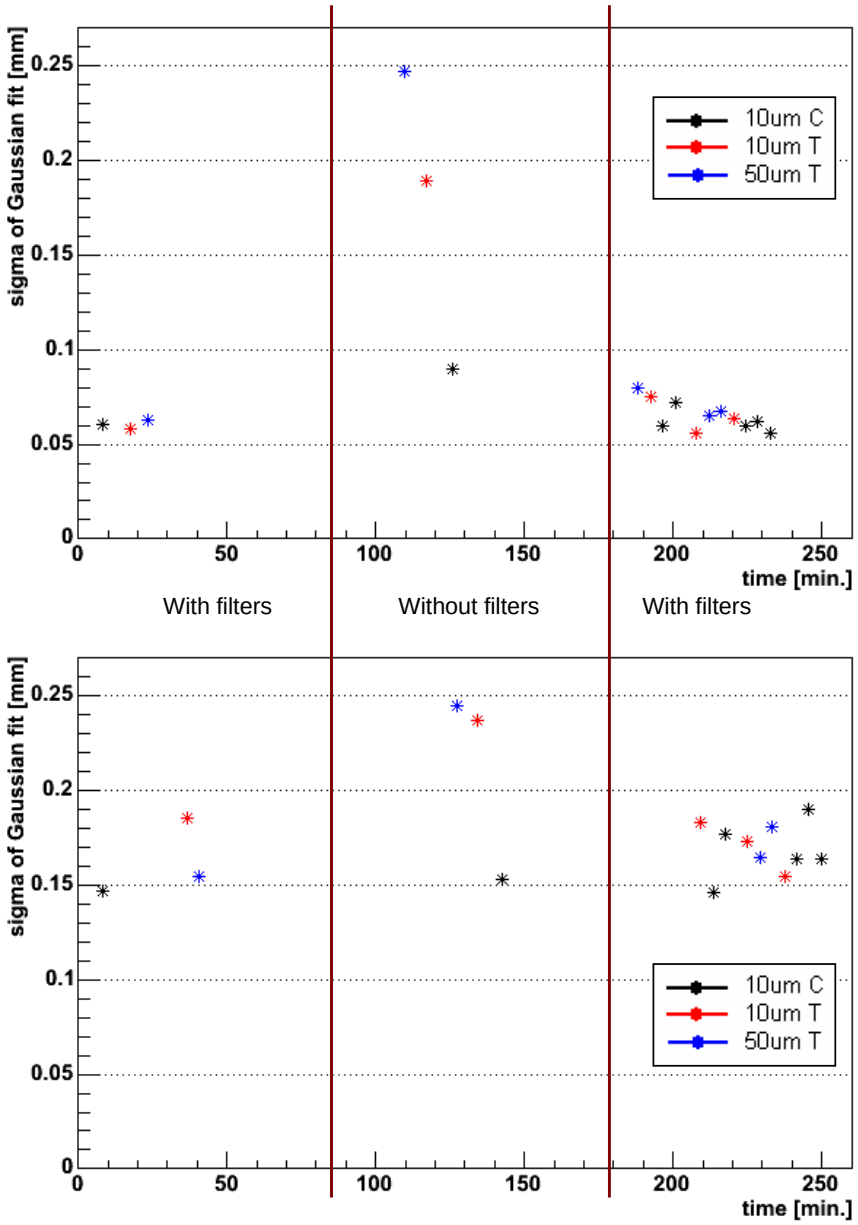

Figure 6.3: Beam size measurements at one of the wirescanners stations (5UND4) for the three available wires as a function of time. Upper plot corresponds to the horizontal plane, lower one to the vertical plane. Two vertical lines divide the plots into three areas. The left and right areas correspond to the measurements with attenuation filters; the center area corresponds to the measurements without filters.

6.3 Beam Tilt at the First Bunch Compressor

When the electron beam is accelerated some degrees off-crest (typically 8 or 9 degrees) at the first accelerator module (ACC1), a correlation between the longitudinal position and the beam energy is induced.

Between the second and the third dipole of the first bunch compressor (D_x = -346 mm), the horizontal transverse position correlates linearly to the beam energy. Therefore, with additional vertical dispersion, the beam is tilted in the x-y plane in the region between the second and the third dipole of BC2 (see Figure 6.4). Due to this effect, the projected vertical emittance is increased.

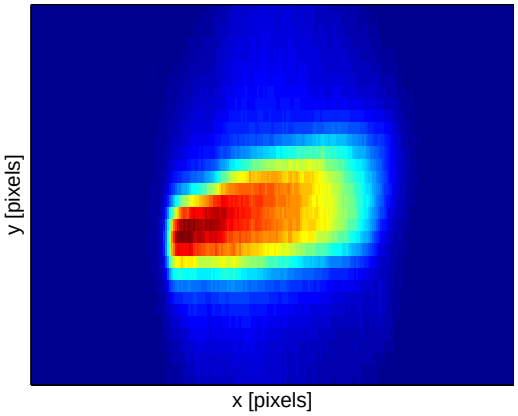

Figure 6.4: Example of beam with an x-y tilt. The image is taken with the SR (Synchrotron Radiation) camera of BC2.

This section studies in a systematic way how vertical dispersion tilts the beam at BC2 and causes an increase of the vertical emittance. The dispersion is generated by applying vertical trajectory bumps through ACC1.

6.3.1 Measurements

Six different vertical trajectory bumps were applied through ACC1, which was running 9 degrees off from on-crest acceleration. Two vertical steerers upstream of ACC1 were used to set the bump (V1GUN and V2GUN) and two correctors downstream of ACC1 to close the bump (V10ACC1 and V1UBC2). The beam charge was 0.62 nC. Figure 6.5 shows a sketch of the experiment.

Table 6.1 shows the amplitudes of the bumps at BPM9ACC1, which were derived from the current of the steerers. For the reference case (no bump, zero current of the gun steerers) the absolute BPM reading at 9ACC1 was

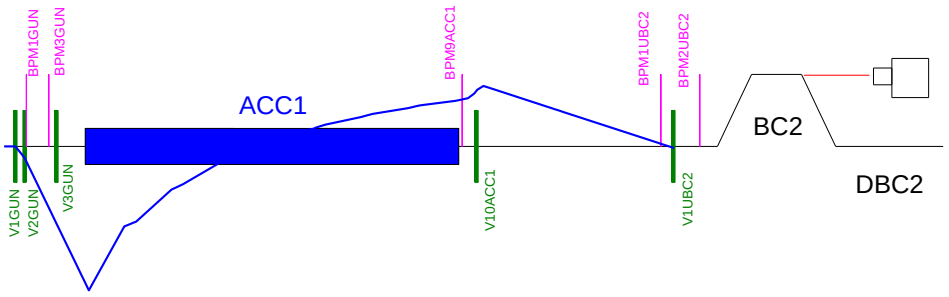

Figure 6.5: Sketch of the beam tilt experiment. Trajectory bumps are excited with gun steerers V1/2GUN and closed with V10ACC1 and V1DBC2. It should be noted the strong focusing effect in the first cavity of ACC1.

-2.8 mm. Maximum bump amplitudes (about 5 mm in each direction) were limited by steerer current and focusing in ACC1.

Table 6.1: Amplitude at BPM9ACC1 for all the bumps for the beam tilt experiment. The absolute reading of BPM9ACC1 for the reference case was -2.8 mm.

Bump	Relative Bump Amplitude [mm]
ref.	0.0
1	-5.3
2	-3.1
3	-2.0
4	1.7
5	3.5
6	4.6

For each bump, the following beam parameters were measured:

1. The **dispersion** from ACC1 (for five out of the six applied bumps). The results are shown in Figure 6.6.

   The horizontal dispersion (upper plot) was small and constant for the different bumps. On the other hand, the measured vertical dispersion for the reference case was not zero, which indicates that the beam traveled off-axis through the module for the reference case.

2. The **beam tilt** at the first bunch compressor using the SR monitor installed behind the third dipole magnet. Per each point, the beam image was obtained by averaging twenty images of consecutive shots

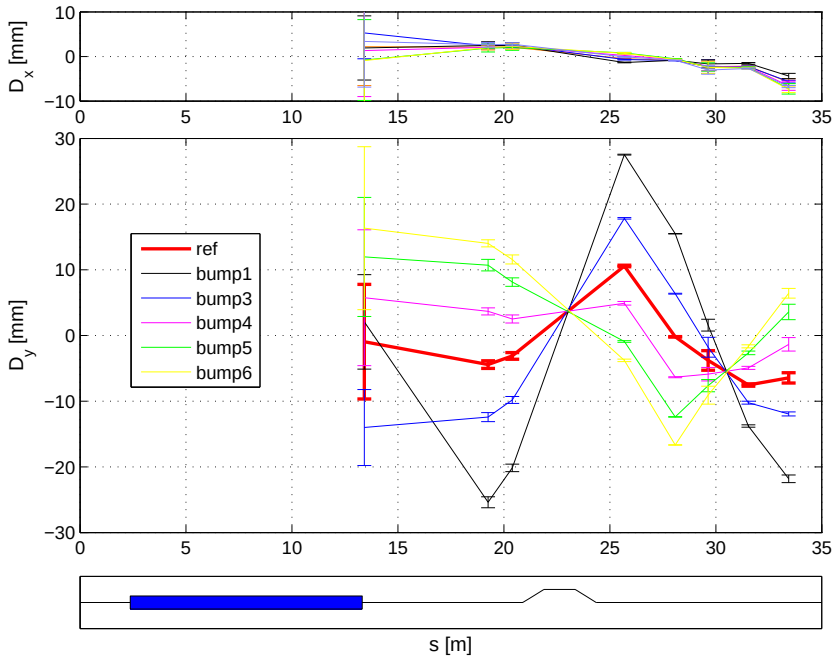

Figure 6.6: Dispersion measurements for the beam tilt experiment. Upper plot: horizontal dispersion. Middle plot: vertical dispersion.

and subtracting the background. To obtain the beam tilt, the image of the region of interest was divided into slices and the center of each slice was determined. Finally, a linear fit to the slice centers gave the beam tilt.

Figure 6.7 shows the measured beam tilts. For the reference case, the measured tilt was 0.6 degrees. Measurements give a slope of -0.24 deg/mm [tilt/bump amplitude].

3. The transverse projected **emittance** downstream of BC2 (see Figure 6.8). The emittance was generally bigger in the horizontal plane due to collective effects in the horizontal bunch compressor (i.e. due to CSR effects). Horizontal emittance remained approximately constant for the different bumps - about 4 µm for the 90 % emittance. Vertical emittance increased for negative bump amplitudes at BPM9ACC1 (from 2.3 µm for the 90 % emittance up to 3.7 µm) and decreased for positive bump amplitudes (down to 1.8 µm).

In the reference situation (without steering in the gun section) the dispersion and the beam tilt were not zero and the emittance was not optimal. This indicates that the beam exited the gun with a non-optimal vertical trajectory.

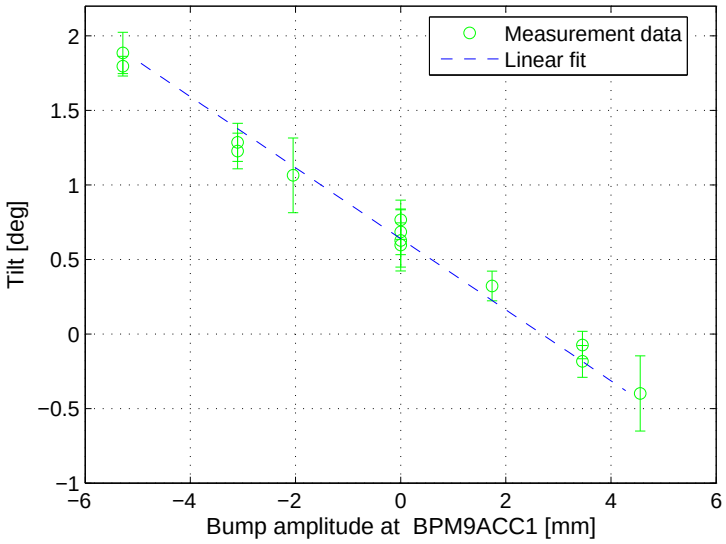

Figure 6.7: Measured beam tilts for the beam tilt experiment.

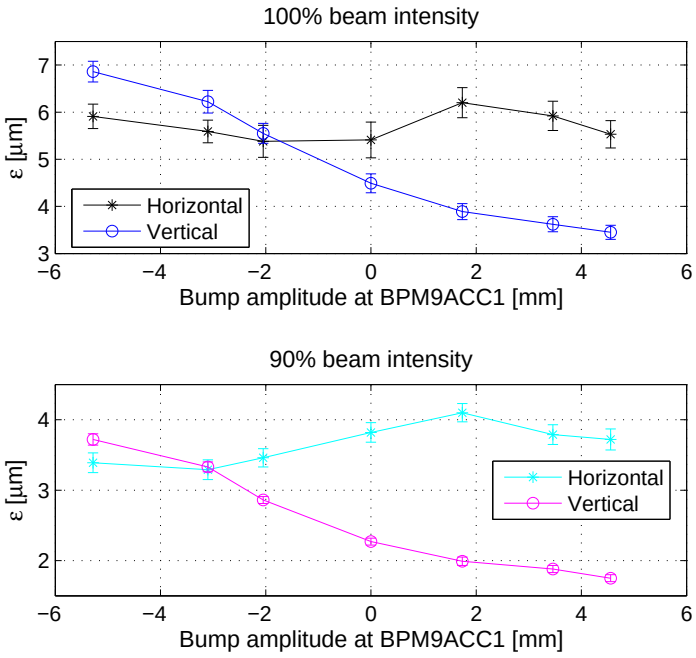

Figure 6.8: Measured horizontal and vertical emittances for the beam tilt experiment. Upper part: values corresponding to the 100 % beam intensity. Lower part: emittances corresponding to the 90 % of beam intensity.

6.3.2 Simulations

Simulations were done with the program *elegant*. The settings for the steerers V1/2GUN were taken from the measurements and the currents for V10ACC1 and V1UBC2 were chosen to close the bump. A 10^5 particle distribution obtained from ASTRA [AST] for standard conditions was used as an input for *elegant*. Wakefields and coupler kicks of the accelerator module ACC1 were taken into account. The effects of the wakefields and coupler kicks on the simulation results were almost negligible.

Two different initial conditions have been considered in the simulations:

1. Ideal on-axis trajectory coming from the gun.
2. An initial vertical trajectory offset of 3.0 mm at the exit of the gun.

Comparison between Measurements and Simulations

- **Trajectory**. The simulations with an initial vertical offset of 3 mm reproduce the absolute orbit at BPM9ACC1 for the reference case (for the simulations without initial offset, the trajectory at BPM9ACC1 for the reference case is obviously zero).

  Figure 6.9 shows the comparison between the measured and the simulated difference orbit for all the bumps. A good agreement is observed except for the biggest negative bumps (bump 2 and specially bump 1), where the saturation of the BPM explains the disagreement.

- **Dispersion**. Figure 6.10 shows the measured and the simulated dispersion for the different bumps. A good agreement between measurements and simulations is observed. Concerning the absolute dispersion for the reference case, the simulations with the initial offset of 3 mm reproduce well the measurements (the simulations without initial offset give zero dispersion).

- **Beam tilt**. Figure 6.11 shows a comparison between the simulated and the measured beam tilt as a function of the bump amplitude. Measurements and both simulations have the same slope *tilt/bump amplitude*. Simulations without initial trajectory offset give no tilt when there is no bump. In the simulations with the initial offset, the tilt is 0.84 degrees - a value which reproduces well the measurement results.

- **Projected emittance**. Figure 6.12 shows a comparison between measured and simulated emittance increase for all the bumps. The simulations with the initial trajectory offset reproduce well the measurements (i.e. emittance increase for negative bumps and decrease for positive bumps). Simulations without an initial offset give optimal emittance for a zero bump amplitude.

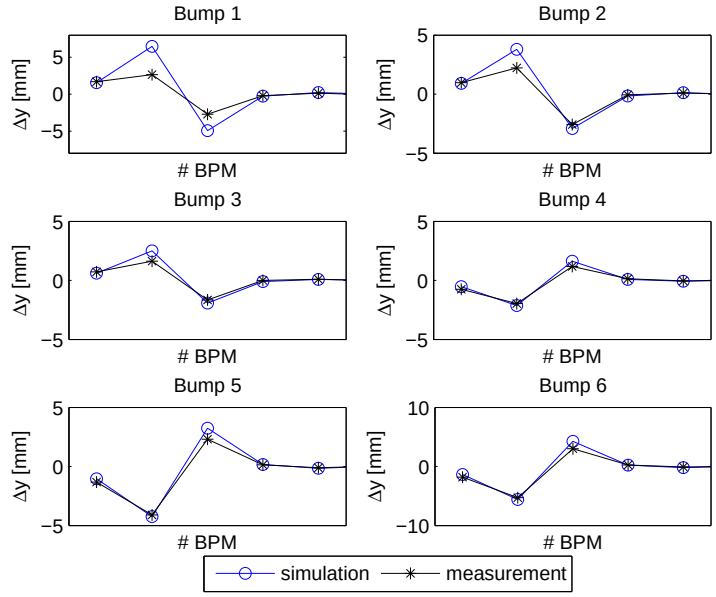

Figure 6.9: Simulated and measured orbit differences for the beam tilt experiment. The third monitor is BPM9ACC1.

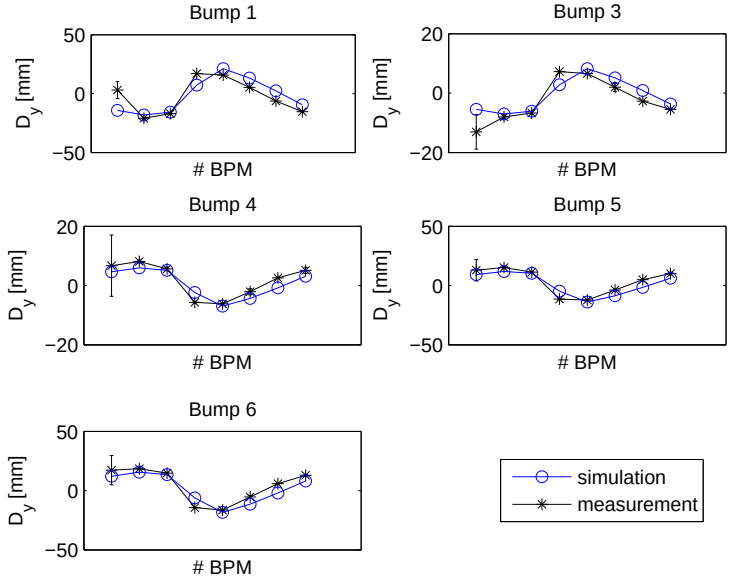

Figure 6.10: Simulated and measured dispersions for the beam tilt experiment. The first monitor is BPM9ACC1.

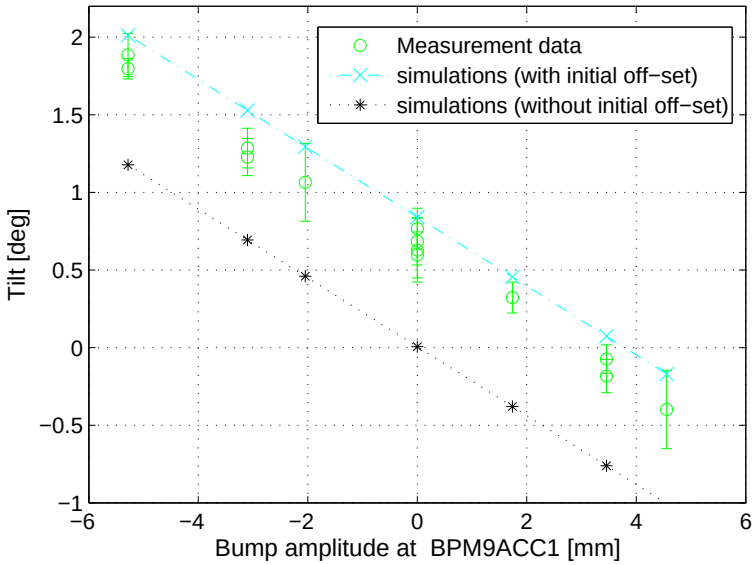

Figure 6.11: Simulated and measured beam tilts for the beam tilt experiment.

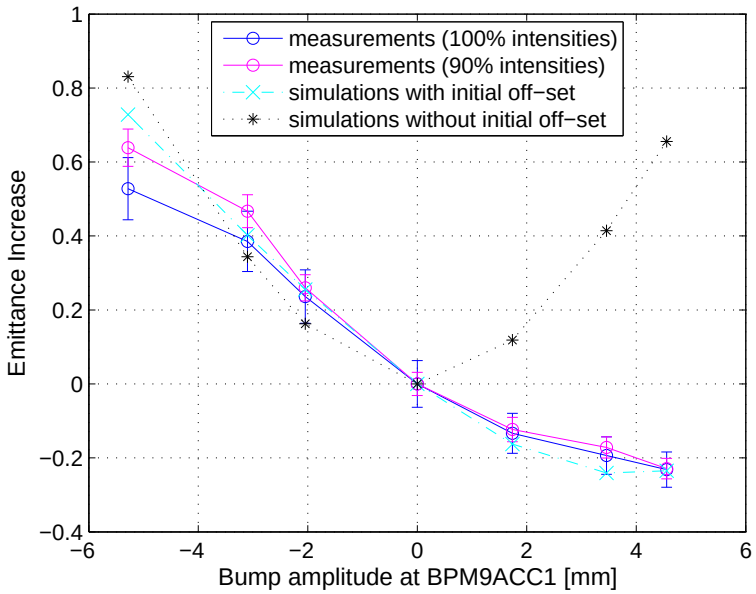

Figure 6.12: Simulated and measured vertical emittance increases for the beam tilt experiment.

- **Beam images**. Figure 6.13 shows the images at BC2 measured during the experiment and the corresponding images of the simulations with the initial vertical offset. A qualitative agreement is observed.

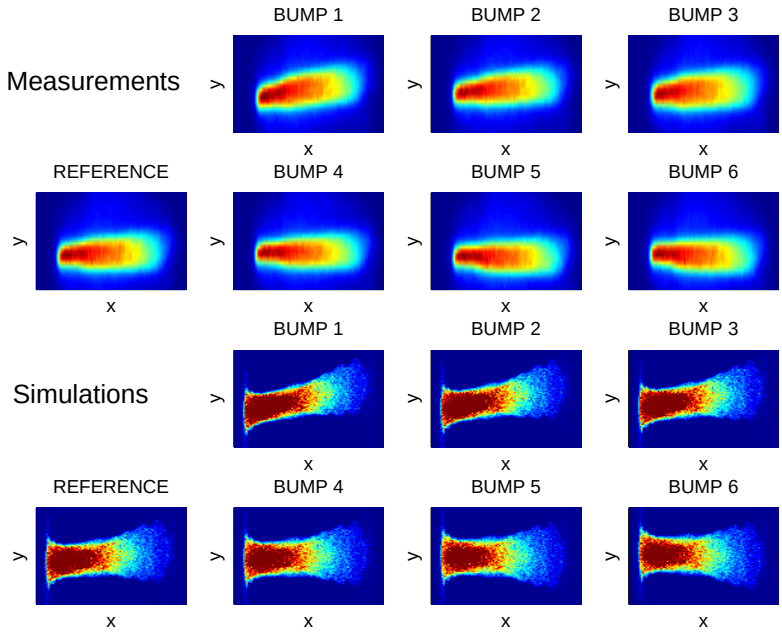

Figure 6.13: Simulated and measured images for the beam tilt experiment.

6.3.3 Discussion

Vertical dispersion degrades the beam quality in the injector section of FLASH when the first accelerator module is running off-crest (as during FEL operation): the beam is observed tilted between the second and the third magnets of the bunch compressor and the projected vertical emittance is increased.

One would expect no beam tilt and minimum vertical emittance without steering through the accelerator module. However, in this case the beam had a tilt of 0.6 degrees and suboptimal emittance. Negative orbit bumps deteriorated even more the beam, while the best beam conditions were fulfilled for the biggest positive bumps (for instance, for the bump number 5: tilt = -0.2 deg., ε_y = 1.9 µm). These results were reproduced in simulations assuming a vertical trajectory offset downstream of the gun (i.e. after the solenoid field) of 3 mm. The required steering in the gun section to improve the beam quality was counteracting a vertical kick which is in accordance with a relative solenoid misalignment of about 300 µm.

Beam tilt measurements with the SR camera can be done parasitically and fast (a measurement averaged over 100 shots and posterior analysis takes about half a minute). Therefore, the SR camera can be used in a convenient way to check and optimize the beam quality at the injector section of FLASH. Moreover, dispersion measurement from ACC1 can be used as a fast indicator for the alignment of the beam within the module.

6.4 Dispersion Effects in the Undulator

6.4.1 Dispersion Generation

As described in Chapter 5, dispersion can be generated by dipole fields along the accelerator. In addition, horizontal dispersion can be created changing the field of the quadrupoles in the collimator section of FLASH (Q3ECOL and Q5ECOL).

In the experiment presented in this subsection, the current of Q3/5ECOL was decreased by 10 %. This resulted in an horizontal dispersion of 140 mm RMS in the undulator section. Figure 6.14 shows the measured and the simulated horizontal dispersion in the undulator. The dispersion measurement was performed by scanning the gradient of the last accelerator modules (ACC456). A good agreement is observed.

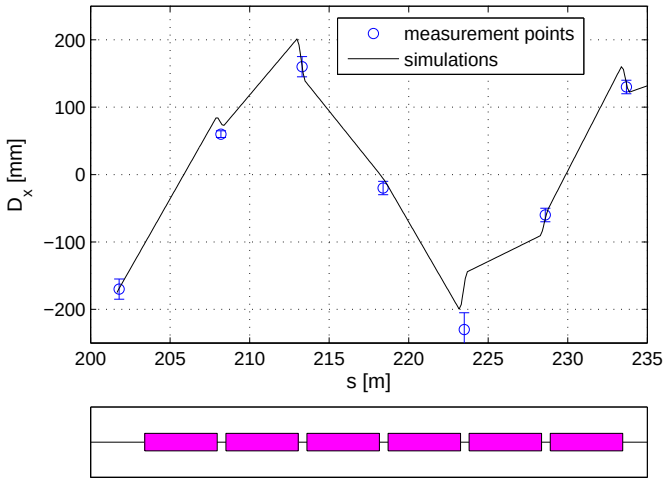

Figure 6.14: Measured and simulated horizontal dispersion in the undulator for the dispersion generation experiment.

In general, an increase of the transverse beam size proportional to the dispersion increase was observed. For instance, while the beam size was strongly increased at 5UND2, 5UND4 and 5UND6 - where dispersion was

large; the beam size remained approximately constant at 5UND3 - where the dispersion did not increase.

Figure 6.15 shows the measured and simulated beam profiles at the wirescanner 5UND6 for three different conditions: on-crest at all the accelerator modules, 20 degrees off-crest at ACC45 and 20 degrees off-crest at ACC45 with the extra dispersion generated. The measured profiles have been shifted in order to remove steering effects which were not completely compensated. Measurements were performed with the 50 µm tungsten wire. Simulations were done from the exit of the first accelerator module to the end of the undulator using *elegant*. A distribution of 10^5 particles obtained from ASTRA for standard conditions was used as an input beam.

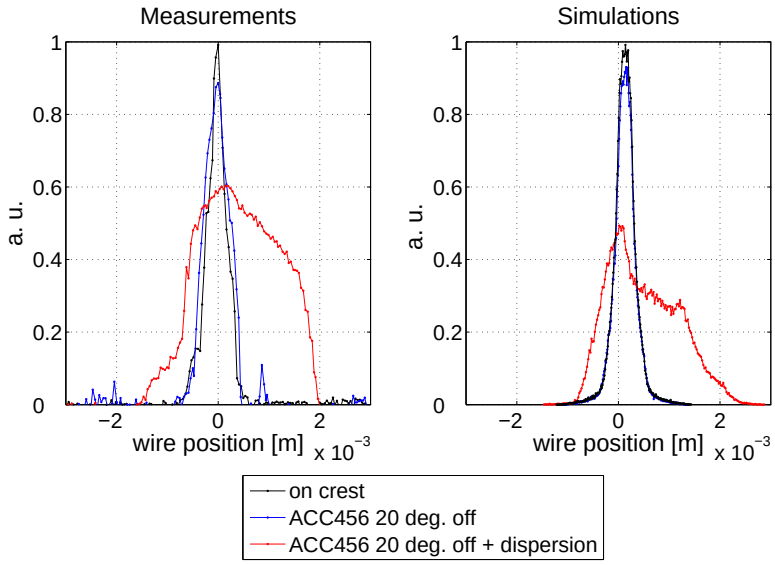

Figure 6.15: Measured (left) and simulated (right) beam profiles at the wirescanner 5UND6 for the dispersion generation experiment.

In both the measurements and the simulations, there are no significant differences between on-crest and off-crest conditions and there is a strong increase of the beam size when the additional dispersion is generated. A qualitative agreement between measurement and simulations of the beam shapes is observed. Since these measurements were done with the 50 µm tungsten wire and without attenuation filters, the measured beam sizes were artificially increased due to non-linear effects of the photo-multipliers (see Section 6.2.4). As a consequence, no perfect agreement between measured and simulated beam profiles can be expected.

6.4.2 Dispersion Correction

In the experiment presented in this subsection, the initial horizontal dispersion in the undulator section was 22 mm (RMS). To perform the correction, the currents of the quadrupole magnets in the collimator section were adjusted. Final compensation using corrector magnets between the collimator and the undulator sections resulted in an RMS dispersion of 4 mm inside the undulator. Figure 6.16 shows the horizontal dispersion measured from accelerator module ACC456 before and after applying the correction.

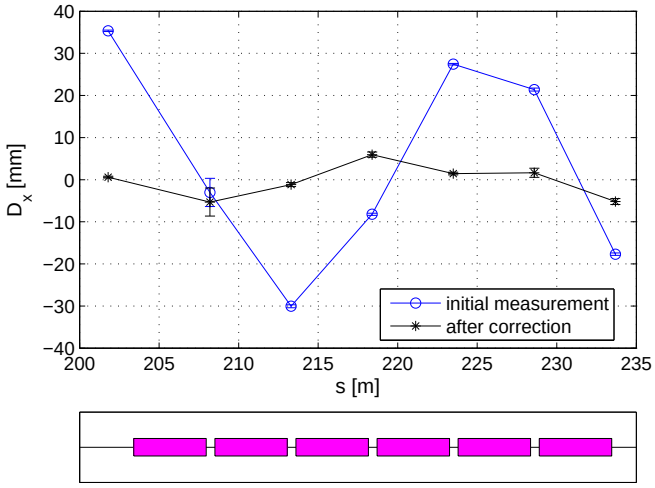

Figure 6.16: Horizontal dispersion in the undulator before and after dispersion correction. The markers correspond to measurement points and the lines between them are only to guide the eye.

Emittance was measured in the undulator section before and after the dispersion compensation. Beam sizes were measured at four different wirescanners: 21SEED, 5UND1, 5UND2 and 5UND3. A significant decrease of the beam size was observed at the points were D_x was reduced (i.e. 21SEED and 5UND2) while the beam size remained approximately constant where the horizontal dispersion was not reduced (i.e. the points where initial D_x was already small: 5UND1 and 5UND3).

The normalized projected emittance was reduced by approximately 20 %, decreasing from 5.8 µm to 4.7 µm. All the accelerator modules were operating on-crest. When FEL radiation is produced, the electron beam is accelerated off-crest leading to a larger energy spread. Therefore, in lasing conditions a larger impact of the dispersion correction on the projected emittance is expected.

Figure 6.17 shows the beam profile measured at the wirescanner 5UND2 before and after correcting the horizontal dispersion. Due to the correction,

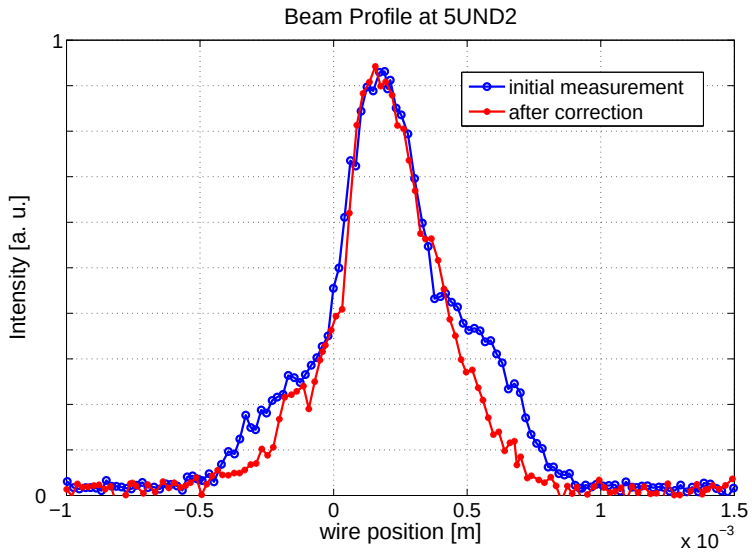

Figure 6.17: Beam profile measurement at wirescanner 5UND2 before and after dispersion correction.

the shoulders created by off-momentum particles of the beam distribution vanished. The RMS beam size was decreased from 252 µm down to 183 µm (i.e. a reduction of 27 %).

6.5 Electromagnetic Fields in TESLA Modules

A TESLA module consists of eight superconducting 1.3 GHz 9-cell RF cavities. Each of these standing wave cavities include one RF input coupler and two high-order mode (HOM) couplers. The HOM couplers are placed one at each side of the cavity and they absorb the energy associated with the HOM field that is excited when the beam travels through the module. Figure 6.18 shows a sketch of a TESLA cavity, indicating the coupler locations.

6.5.1 Coupler Kicks

Both power and HOM couplers induce transverse kicks. The kick produced by the main coupler is horizontal and depends on the cavity field and the coupler configuration. The HOM-couplers induce kicks in both horizontal and vertical directions and depend only on the cavity field. The distortions on the electromagnetic field induced by coupler regions have been calculated with MAFIA [MAF]. The voltage induced by the upstream coupler region

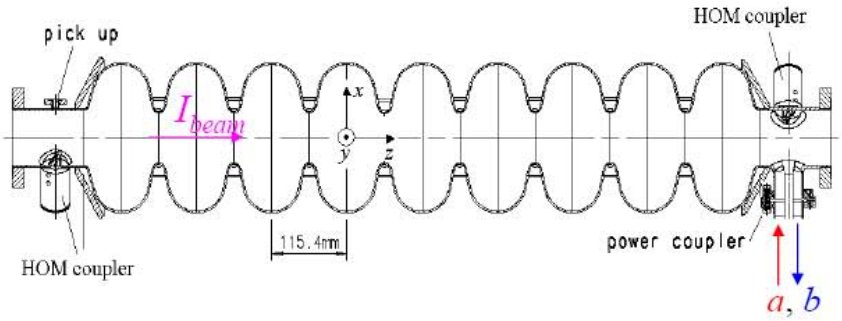

Figure 6.18: Overview of a TESLA 9-cell RF cavity. The total length is about 1.2 m. The upstream region (left) includes a HOM coupler and the downstream region (right) the main and a HOM coupler. The iris radius is 35 mm.

at the center of the cavity for a typical configuration is [Pra08]:

$$\begin{aligned} \frac{V_x}{V_z} \cdot 10^6 &= -59.1 + 9.4i \\ \frac{V_y}{V_z} \cdot 10^6 &= -43.2 - 1.8i \end{aligned} \tag{6.5}$$

The transverse voltage induced by the downstream coupler is:

$$\begin{aligned} \frac{V_x}{V_z} \cdot 10^6 &= 11.4 + 48.6i \\ \frac{V_y}{V_z} \cdot 10^6 &= 45.5 - 2.8i \end{aligned} \tag{6.6}$$

The real part of the above equations corresponds to a net kick experienced by the whole bunch which produces a trajectory deviation. For instance, assuming an RF field of 20 MV/m and taking into account that a TESLA cavity is 1.0362 m of length, the horizontal voltage induced for the upstream couplers is about 1.2 kV. This is equivalent to a kick of 12 µrad for an electron beam of 100 MeV. The imaginary part corresponds to a kick which depends on the phase experienced by each particle. This kick distorts the trajectory of the longitudinal slices of the beam by different amounts, which results in an increase of the projected emittance.

The coupler kicks depend also on the transverse position of the beam with respect to the cavity axis. Figure 6.19 shows a map of the electric field induced by the coupler regions; i.e. the fields for different horizontal and vertical beam positions [Pra08]. Left and right maps correspond to the real and the imaginary part of the kick respectively. The field at the center of the map correspond to the kick induced on-axis (equations 6.5 and 6.6).

The off-axis dependence of the coupler kicks causes an increase of the slice emittance.

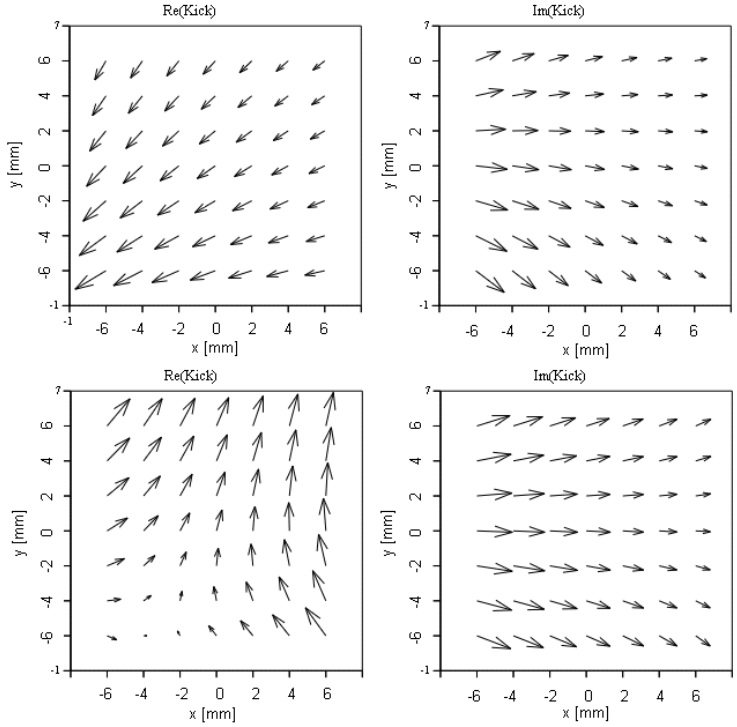

Figure 6.19: Induced voltage map for the upstream and downstream coupler regions of a TESLA cavity.

6.5.2 Transverse Wakefields

A charged particle beam generates EM fields at any cross-section variation of the vacuum vessel. These electromagnetic fields act on the electrons arriving later and produce distortions in the longitudinal and transverse directions. A transverse wakefield can be generally characterized by a *transverse wake function*, which in this thesis is defined as the integral over the transverse EM forces along a straight path at the distance ζ behind an exciting point charge traveling with constant velocity $v \approx c$ and divided by the value of the charge [Zot98]:

$$\vec{w}_\perp = \frac{1}{q} \int_{-\infty}^{\infty} (\vec{E} + \vec{v} \times \vec{B})_\perp dz \tag{6.7}$$

If the transverse wake function for a particular geometry is known, the *transverse wake potential* can be calculated as its convolution with the par-

ticle distribution $\lambda(\tau)$:

$$W_{\perp}(\tau) = \int_0^{\infty} w_{\perp}(t)\lambda(\tau - t)dt \tag{6.8}$$

The transverse impulse received by an electron with charge e which accompanies the bunch at the longitudinal position ξ can be calculated from the wake potential as follows [Ban87]:

$$p_x(\xi) = x'(\xi)p = \frac{eQW_x(\xi)}{v} \tag{6.9}$$

where Q is the total charge of the bunch and v is the longitudinal velocity of the particle.

One can distinguish between the wakes generated by the TESLA module itself (rotationally symmetric structure) and the wakefields created by the input and HOM couplers (non-symmetric elements). The transverse wake functions per TESLA cavity have been obtained by fitting numerical data to analytic expressions [Wei03]:

$$\begin{aligned} \vec{w}_{\perp_T} = H(\zeta) \cdot \frac{10^{15}}{8}\left[1 - (1+\Omega)e^{-\Omega}\right] \cdot \begin{pmatrix} x[\mathrm{m}] \\ y[\mathrm{m}] \end{pmatrix} \left[\frac{\mathrm{V}}{\mathrm{C}}\right] \\ \text{with} \quad \Omega = \left[\frac{\zeta}{0.92 \cdot 10^{-3}}\right]^{1/2} \end{aligned} \tag{6.10}$$

where ζ is the distance between the test and source particle, $H(\zeta)$ is the Heaviside step function[5], and x and y are the transverse offsets of the source with respect to the cavity axis. The kick produced by the wake of a TESLA module is proportional to the transverse deviation of the beam and is zero if the bunch travels on-axis.

The wake function induced by the couplers of a TESLA cavity is [Zag07]:

$$\vec{w}_{\perp_C} = H(\zeta) \cdot 10^{12}\left[\begin{pmatrix} -0.042 \\ -0.038 \end{pmatrix} + \begin{pmatrix} 8.6 & 0.14 \\ 0.06 & -1.8 \end{pmatrix} \cdot \begin{pmatrix} x[\mathrm{m}] \\ y[\mathrm{m}] \end{pmatrix}\right]\left[\frac{\mathrm{V}}{\mathrm{C}}\right] \tag{6.11}$$

The coupler wake has two components - one independent of its transverse coordinates and one which depends on the position of the source. The wake function of the couplers is constant and the resulting kick factor does not depend on the bunch length. However, it has been shown that the constant wake function given by equation 6.11 overestimates the kick factor for short bunches [Doh08a].

[5]The value of $H(\zeta)$ is zero for negative argument ($\zeta < 0$) and one for positive argument ($\zeta > 0$).

Comparison between Structure and Coupler Wakes

For a Gaussian beam with an RMS length of 300 µm the effect of the coupler wake on-axis is equivalent to the impact of the module wake with a horizontal and vertical beam offset of 2.9 and 2.6 mm respectively. In both cases the resulting kick factor (i.e. the integrated kick over the bunch) is 0.021 V/pC for the horizontal plane and 0.019 V/pC for the vertical one. Figure 6.20 shows the horizontal and the vertical kick along the bunch due to module and coupler wake effects for this particular example.

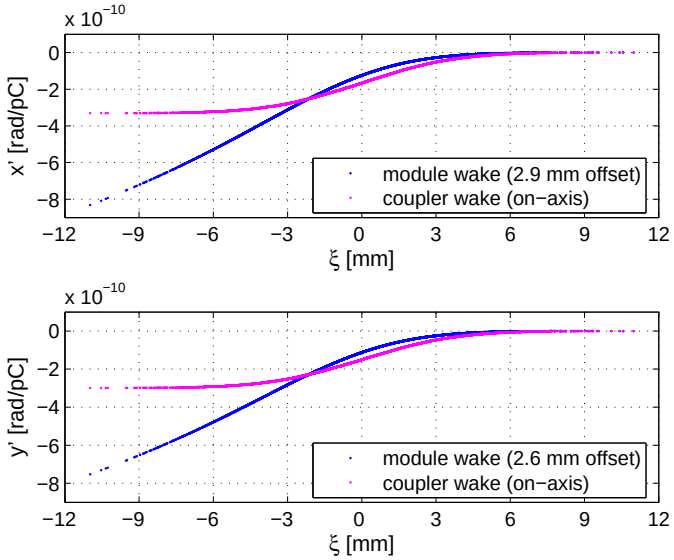

Figure 6.20: Comparison between transverse kicks generated by structure wake (with the indicated offsets) and coupler wakes (on-axis) for a Gaussian beam of 300 µm length. Both wakes induce the same kick.

6.5.3 Modeling in *elegant*

Coupler kicks are implemented in *elegant* as transverse deflecting cavities with the same frequency as the accelerator structure (1.3 GHz). The coupler kick is modeled as two independent cavities - one with a zero degree phase (net kick given to the bunch) and one with ninety degrees off-crest (phase-dependent part of the kick).

The orbit dependence of the coupler kick is solved iteratively. First, the beam is tracked assuming on-axis coupler kicks for all the cavities. This gives a trajectory deviation which is used to determine the new values of the coupler kicks. Then the beam is tracked again and this procedure is repeated until the result converges. Usually between two and four iterations are required to get an orbit convergence better than 1 µm.

In addition, both structure and coupler wakefields are implemented by supplying the program with the corresponding wake functions.

6.5.4 Impact of Orbit Bumps Through TESLA modules

The degradation of the beam quality due to wakes and coupler kicks of the TESLA modules was analyzed at FLASH. For this purpose the emittance was measured as a function of the trajectory through the accelerator modules ACC23 and ACC456.

Figure 6.21 shows a sketch of a particular experiment where horizontal bumps were applied through ACC23. The amplitude of the bump refers to the trajectory at BPM11DBC2 - a beam position monitor placed just upstream of ACC2. The bumps were closed downstream of ACC3 before the second bunch compressor (BC3). All the accelerator modules were working on-crest. Electron beam charge was 0.6 nC. Final electron energy was 700 MeV.

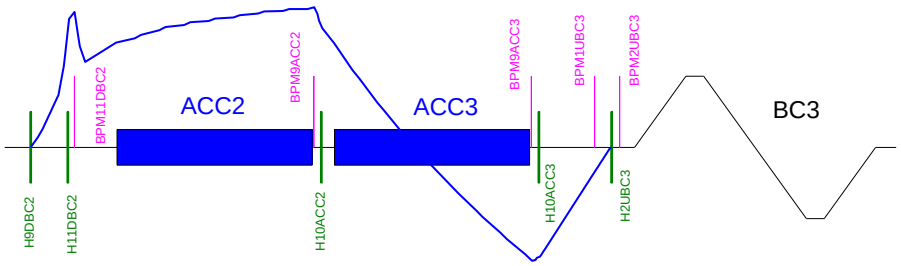

Figure 6.21: Sketch of the experiment on the impact of horizontal bumps through ACC23. Bumps were set with H9DBC2 and H11DBC2 and closed with H10ACC2, H1UBC3 and H2UBC3.

Figure 6.22 shows the measured and the simulated emittance increase for the different bumps. For each bump the emittance was measured using the OTR screens in the seed section. A reference measurement was taken before and after the bumps were applied. Emittance values for the initial and final references were similar (3.2 and 2.8 µm). The vertical emittance did not change in any case. The error bars of the plots are based only on the statistical error of the beam size measurements required for the emittance calculation. The beam was not matched for the different emittance measurements - the mismatch parameter M_x is shown in Figure 6.22.

Simulations were done from the exit of the first accelerator module to the entrance of the undulator using *elegant*. A Gaussian distribution of 10^5 particles was used as an input beam. Module and coupler wakefields as well as coupler RF kick effects were taken into account.

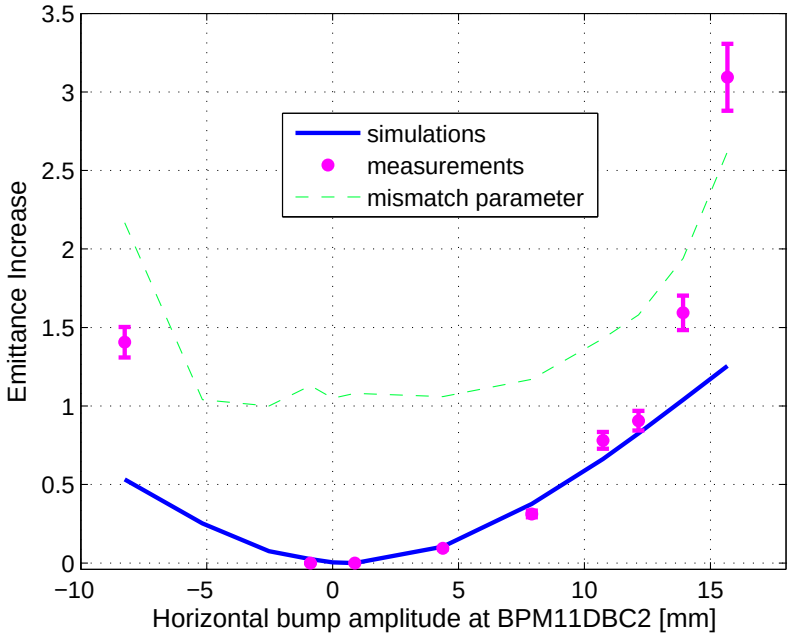

Figure 6.22: Measurements and simulations of emittance increase for different bumps through ACC23.

There is a qualitative agreement between measurements and simulations. For moderate bumps the simulations fit well with the measurements. However, for the extreme cases simulations predict a much weaker effect than the measured one. On one hand, the measured mismatch parameter for these cases was big (> 1.5) - a fact which increases the systematic error of the measured emittances. On the other hand, the kicks induced by the couplers are calculated in a limited area of ± 6 mm around the cavity center (see Figure 6.19). The model used in these simulations extrapolates linearly the kicks outside this limited area. This extrapolation underestimates the effects of the couplers when the beam travels out of this $\pm$ 6x6 mm region.

Further measurements done at ACC1, ACC23, and ACC456 with moderate bumps (in both planes) confirmed the good agreement with the simulations. There is an insignificant increase of the transverse emittance (below 10 %) when the trajectory is kept below the 2 mm level.

6.6 Conclusion

Two main effects which deteriorate the transverse beam quality were studied in this chapter: dispersion and RF fields of accelerator modules. Both effects are closely related to the electron trajectory. On one hand, spu-

rious dispersion is created whenever the beam travels off-axis through a quadrupole magnet or an accelerator module. On the other hand, orbit deviations through the modules, apart from generating dispersion, enhance the wakefield and the coupler kick effects of these structures.

Dispersion compensation along the whole linac is a necessary condition for the emittance conservation. The measured dispersion from all the accelerator modules must be corrected below 10 mm to maintain a decent beam quality. As it has been exemplified in Section 5.1.4, dispersion depends on several parameters which change very frequently, so dispersion must be controlled often.

Moreover, the electron trajectory through the modules must be controlled to avoid a significant increase of the transverse emittance due to wakefield and coupler kick effects. Studies presented in this chapter show that the orbit through all the modules should be corrected below the 2 mm level to keep the emittance increase below 10 %.

In the beam tilt measurements it was shown that moderate vertical bumps through ACC1 can cause a significant increase of the emittance. This increase is due to dispersion, the effect of which becomes specially important because ACC1 runs off-crest.

Table 6.2 shows the results of emittance measurements performed along the FLASH linac on two different days. In both cases, linac optimization, i.e. dispersion and orbit correction, was carried out prior to the measurements. The measurements at BC and seed section were done using OTR screens. The shown emittance values correspond to the 90 and the 100 % of the beam intensity. In the first day, the emittances corresponding to the entire beam intensity were also measured with the wirescanners in the undulator. In all the cases the electron beam charge was 1 nC and the beam traveled on-crest through all the accelerator modules. The final beam energy was around 500 MeV in the first measurement day and around 700 MeV in the second one.

Since the focus was on the transport of the emittance through the machine, not much time was spent on optimizing the initial emittance. In well optimized conditions, a projected emittance below 2 µm in the BC section has been measured [Loe05] [Loe06]. As indicated in Table 2.1, the design normalized projected emittance for FLASH is 2 µm.

An analysis taking into account errors in the beam size, in the energy and in the transfer matrices leads to an error estimation of the measured emittance of about 0.5 µm. As indicated in Table 6.2, similar normalized emittances were obtained along FLASH on the two measurement days. It can be concluded that there is no substantial change in emittance along the linac when the trajectory and dispersion are corrected.

Table 6.2: Results of projected emittance measurements at FLASH. The values shown are normalized RMS emittances for 90 % and 100 % (in brackets) beam intensities.

Day	17-02-2007		08-09-2007	
Section	ε_x[µm]	ε_y[µm]	ε_x[µm]	ε_y[µm]
BC	**2.4** (3.7)	**2.5** (3.8)	**2.2** (3.7)	**2.1** (3.6)
Seed	**2.0** (2.7)	**2.2** (3.0)	**1.8** (2.9)	**2.3** (3.8)
Undulator	(3.6)	(3.6)	-	-

It should be noted that emittances in the undulator presented in Table 6.2 (done before the installation of the filters) correspond to measurements using the 10 µm carbon wire. In former measurements using the 50 µm tungsten wires (without filters) emittances between 20 and 40 µm were typically measured.

Chapter 7

Dispersion Effects on FEL Performance at FLASH

This chapter studies the impact of dispersion on the FEL performance in two main aspects: radiation power sensitivity to electron energy offset and radiation wavelength spectrum. Since these issues are related to electron trajectories, studies on the FEL power dependence to the beam orbit are also presented. The first section contains a description of the code used for FEL simulations and presents electron beam properties obtained from start-to-end simulations at the undulator entrance.

7.1 FEL Simulations with *Genesis 1.3*

To study the impact of transverse effects on the FEL performance, it is necessary to use a three-dimensional time-dependent FEL program. From the different available programs, *Genesis 1.3* has been selected for the simulations presented in this chapter.

Genesis 1.3 has been benchmarked successfully with FEL experiments like FLASH [Gol07] and other codes such as *Medusa* [Fre05] and *Ginger* [Gol07]. Moreover, it has been used to design and optimize FEL projects like the XFEL [Agh07]. *Genesis 1.3* was first released in 1999 and is written in FORTRAN. Version 2.0 (released in April 2008) was used for the simulations presented in this chapter. More detailed information about *Genesis 1.3* can be found in [Rei99]. The manual is in [GEN].

Genesis 1.3 is controlled by approximately 100 parameters which characterize the undulator, the focusing, the electron and radiation beams, the mesh used for the calculations, and the type of simulation. The program allows the usage of a file containing a lookup table for the electron beam parameters at different longitudinal position along the bunch. A file with the properties shown in Figure 7.1 was used for the simulations presented in this chapter. This file was obtained from start-to-end simulations done

for FLASH at 495 MeV and 0.85 nC using CSRtrack [CSR] for the bunch compressors and the collimator section and ASTRA for the remainder of the lattice.

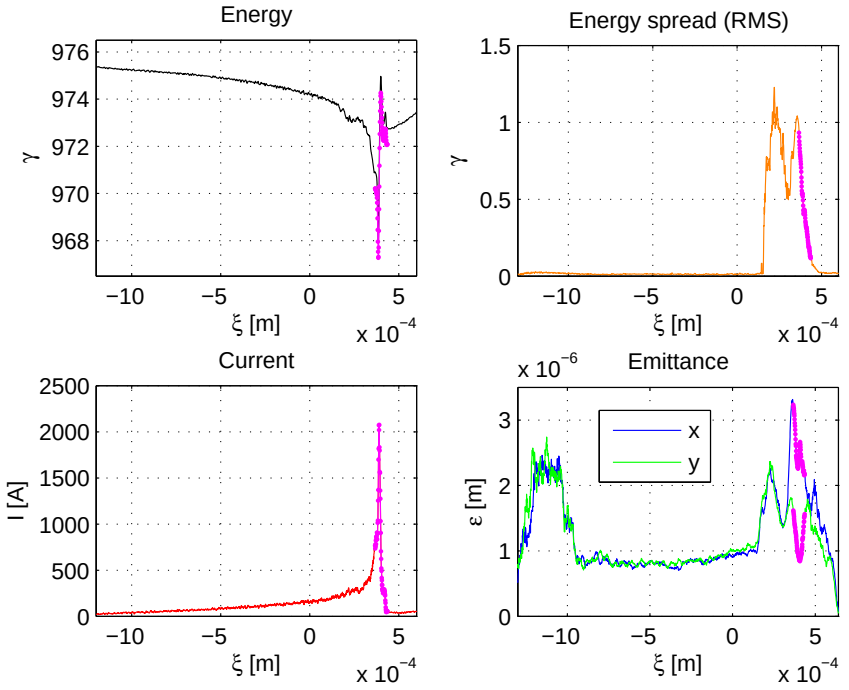

Figure 7.1: Electron beam properties at the undulator entrance obtained from start-to-end simulations. Only the part marked by the magenta dots produces FEL radiation and is used as an input for *Genesis 1.3*.

7.2 SASE Sensitivity to Transverse Trajectory

The FEL power sensitivity to the incoming electron beam trajectory was measured at FLASH. For this purpose, the closest steerers in front of the undulator were scanned: H19SEED and V19SEED (horizontal and vertical kick respectively). The beam charge was 0.80 nC and the beam energy was 450 MeV. Measurements for H19SEED were repeated on another day when the beam energy was 495 MeV and the charge was 0.85 nC. Figure 7.2 shows an sketch of the experiment.

Figure 7.3 shows the results of the measurements and the corresponding simulations. The relative FEL power for the different kicks is indicated. Each measurement is the result of averaging over 100 shots. The maximum SASE energy was about 20 µJ on the first measurement day and 50 µJ on the second measurement day measured by a MCP(micro-channel plate)-based

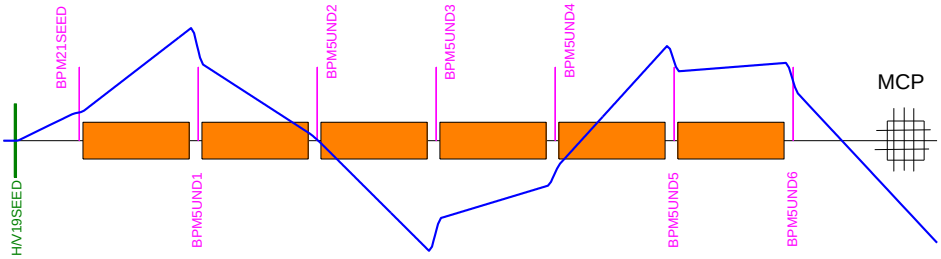

Figure 7.2: Sketch of the experiment on SASE sensitivity to electron trajectory. The FEL energy is recorded with a MCP detector as a function of the orbit deviations produced by the steerers H19SEED and V19SEED.

photon detector [Byt04] [Bit07]. As it can be seen in the figure, measurements for the horizontal plane done on the two different days show a good reproducibility.

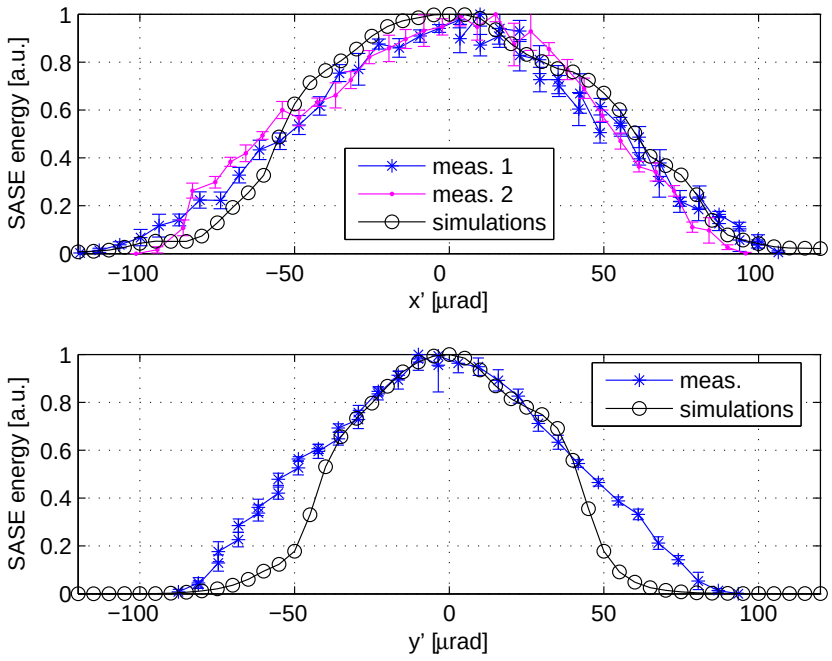

Figure 7.3: Measurements and simulations of SASE sensitivity to the incoming trajectory.

Simulations were done using the electron beam properties plotted in Figure 7.1 as an input. In the simulations maximum SASE macropulse energy is about 30 µJ. There is a good agreement between measurements and simulations in the horizontal plane. In the vertical plane, there is a good agreement for moderate kicks (i.e. in the range of ±30 µrad) while for bigger kicks the simulation predicts a bigger SASE sensitivity to the orbit than the measured one.

As it can be seen in Figure 7.3, FEL energy is more sensitive to the vertical trajectory than to the horizontal one in both the measurements and the simulations: measured Full Width Half Maximum (FWHM) of the curve is 100–105 µrad for the horizontal plane and 90 µrad for the vertical one. This is because the wiggling movement of the electrons in the undulator takes place in the horizontal plane. Moreover, the additional natural focusing of the undulator in the vertical plane contributes to this bigger sensitivity of SASE energy to the vertical trajectory.

7.3 SASE Sensitivity to Electron Energy Offset

7.3.1 Measurements

In order to show the reduction of the FEL power sensitivity to the electron beam energy when dispersion is corrected, the SASE macropulse energy was measured for four different dispersion scenarios as a function of the beam electron energy offset:

- **Initial situation.** RMS dispersion in the undulator was 22 mm in the horizontal plane and 30 mm in the vertical one.
- **Extra horizontal dispersion.** Additional horizontal dispersion was introduced by changing the current of the quadrupole magnets in the collimator section (Q3/5ECOL), resulting in an RMS value in the undulator of 48 mm. Vertical dispersion remained almost the same (28 mm).
- **Horizontal dispersion corrected.** The collimator quadrupole currents were adjusted to reduce the horizontal dispersion. Final value was 12 mm, and 31 mm in the vertical plane.
- **Horizontal and vertical dispersion corrected.** Starting from the previous conditions, vertical steerers from upstream of the dogleg up to the seed section were adjusted to correct vertical dispersion. Final RMS values in the undulator were 11 mm in the horizontal direction and 5 mm in the vertical one.

Figure 7.4 shows measured dispersion from ACC456 in the undulator BPMs for the different dispersion conditions.

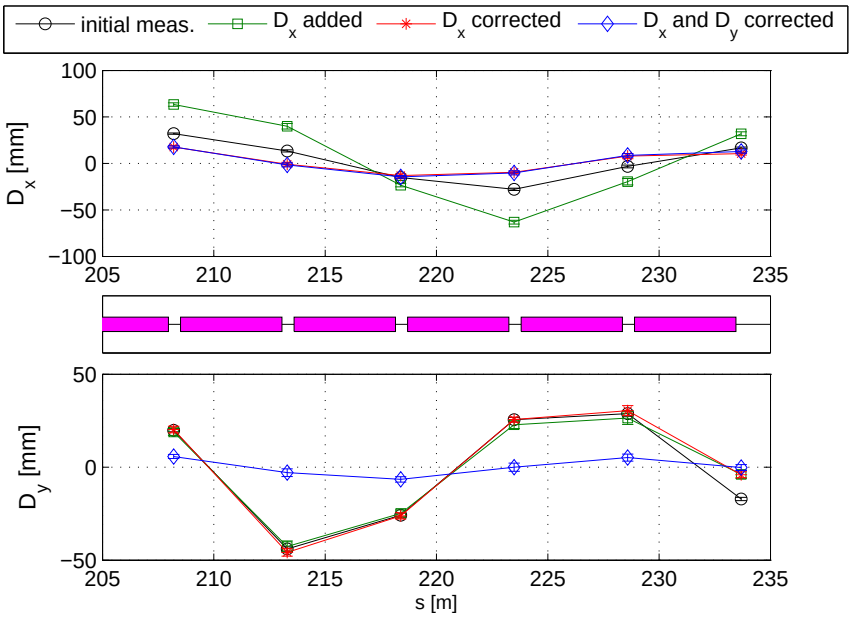

Figure 7.4: Measured dispersion in the undulator for the different conditions of the experiment on SASE sensitivity to electron energy offset. The markers correspond to measurement points and the lines between them are only to guide the eye.

Figure 7.5 shows the results of the experiment. The initial electron energy was 495 MeV and the electron charge was 0.85 nC. The plotted SASE energies are averaged over 100 shots. Although units were chosen arbitrarily to make the comparison easier, maximum SASE macropulse energy was similar in both cases: 49 µJ before dispersion correction and 40 µJ afterwards (measured by the MCP detector). The different electron energies were obtained by changing the gradient of the accelerator modules ACC456.

Initially, the FWHM of the SASE energy distribution in terms of relative electron energy deviation was 0.82 %. Adding horizontal dispersion reduced the FWHM down to 0.74 %, and correcting it increased the value up to 1.06 %. After correcting the dispersion in both planes, the final FWHM was 1.72 %. This means that after dispersion correction, the SASE sensitivity to electron energy offset was improved by more than a factor of two compared to the initial conditions. Table 7.1 shows a summary of the experimental results.

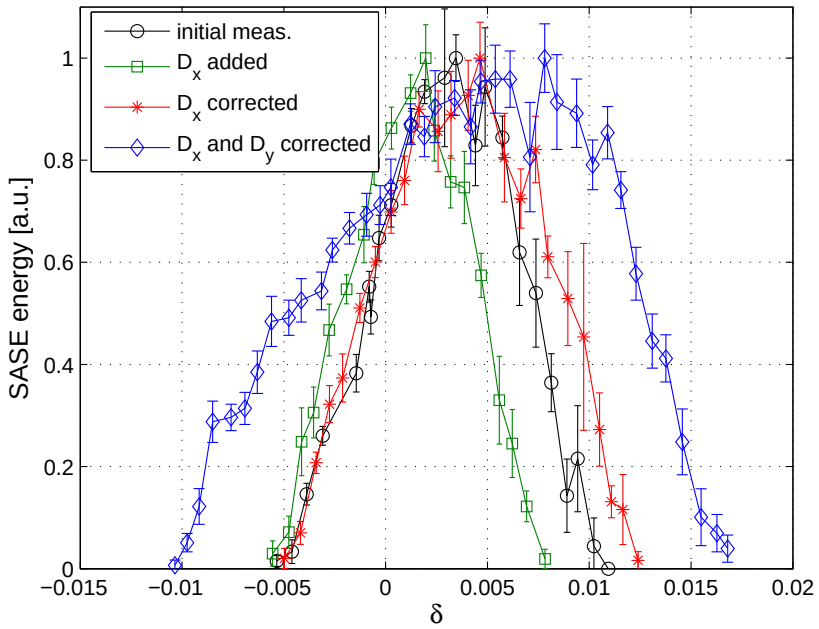

Figure 7.5: Measured SASE energy as a function of electron energy offset ($\delta = \Delta p/p_0$) for the different conditions of the experiment on SASE sensitivity to electron energy offset.

Table 7.1: Summary of measurements on SASE energy sensitivity to relative electron energy offset. For the different conditions, RMS values of the dispersion functions in the undulator and the corresponding FWHM of the SASE energy distribution in terms of relative electron energy deviation are indicated.

Condition	D_x	D_y	FWHM in δ
Initial measurement	22 mm	30 mm	0.82 %
D_x generated	48 mm	28 mm	0.74 %
D_x corrected	12 mm	31 mm	1.06 %
D_x and D_y corrected	11 mm	5 mm	1.72 %

7.3.2 Simulations

Time-dependent simulations of these measurements were performed with *Genesis 1.3*. Only the initial case and the situation after dispersion correction in both planes were considered. The input electron beam used in the simulations for the reference point has the characteristics shown in Figure

7.1. The rest of the conditions are characterized by the following differences with respect to the reference beam:

1. **Centroid energy change**. *Genesis 1.3* calculates only the FEL power in a certain bandwidth around the resonant radiation wavelength. Due to that, the resonant wavelength should be changed together with the electron energy to avoid an artificial decrease of the output radiation power. An equivalent but easier solution was adopted instead: neither the electron energy nor the resonant radiation wavelength were modified, but all the external parameters (trajectory, optics, undulator field and focusing) were scaled accordingly.

2. **Trajectory deviation** according to energy variation and dispersion: $\Delta u = D_u \cdot \delta$ and $\Delta u' = D'_u \cdot \delta$, where u refers both to x and y.
D_u and D'_u have been obtained at the entrance of the undulator using equation 4.19 and the measurements of D_u in the first two undulator BPMs (from measurements shown at Figure 7.4). For that it has been assumed that no dispersion is generated between the first two undulator BPMs. The values are indicated in the following table.

	Initial situation	After correction
D_x	12.12 mm	14.47 mm
D'_x	5.97 mrad	1.91 mrad
D_y	46.68 mm	4.94 mm
D'_y	-2.89 mrad	0.39 mrad

Assuming that no dispersion is created inside the undulator section, the dispersion in all the undulator BPMs can be reconstructed using equation 4.19. Figure 7.6 shows measured and reconstructed dispersion values for both scenarios (initial case and after correction). A good agreement is observed, which means that no dispersion is created inside the undulator section.

3. **Optics variation** Since the magnet currents were not scaled, the optics at the entrance of the undulator have been re-calculated according to the energy variation.

Figure 7.7 shows measured and simulated SASE energy versus electron beam energy deviation. A good agreement between measurements and simulations is observed, showing the increase of the FWHM of the SASE energy distribution in terms of δ when the dispersion is corrected.

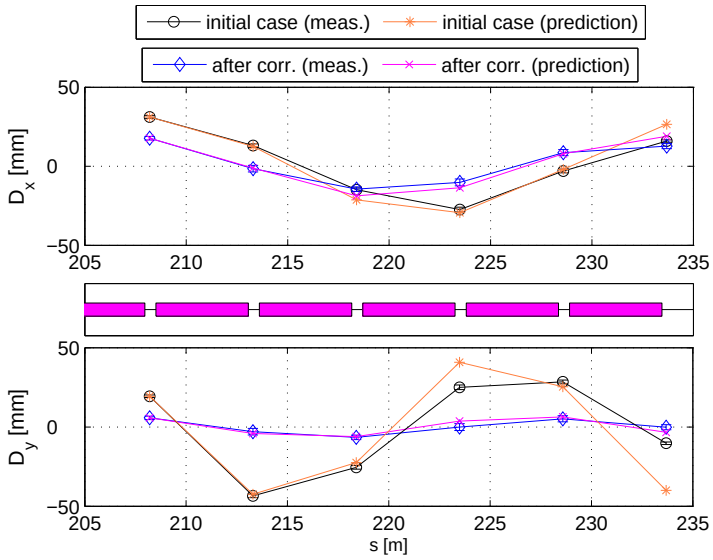

Figure 7.6: Measured and reconstructed dispersion along the undulator before and after correction for the experiment on SASE sensitivity to electron energy offset.

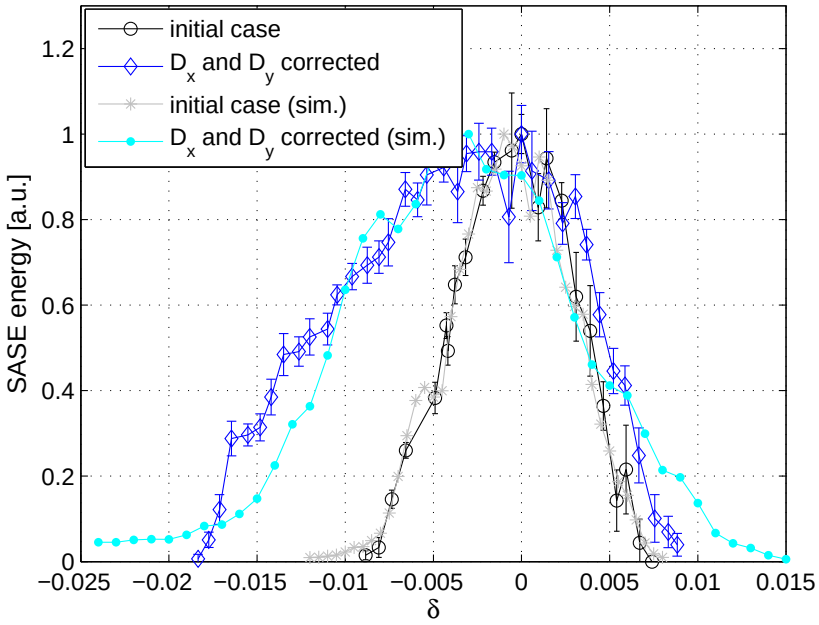

Figure 7.7: Measurements and simulations of SASE energy as a function of electron energy offset before and after dispersion correction.

7.4 Dispersion Impact on the SASE Spectrum

Figure 7.8 shows the energy and the current along the bunch obtained from start-to-end simulations for the electron slices that produce FEL radiation (see also Figure 7.1). As illustrated in the figure, there is an energy variation along the bunch of about 3 MeV which causes the beam slices to produce FEL radiation with different wavelengths. Without dispersion, the trajectory is the same for all the particles, so all the slices produce FEL radiation. Dispersion causes trajectory deviations of the slices depending on their energy. As a consequence, dispersion can prevent some of the beam slices from radiating (depending on the dispersion magnitude and on the nominal energy). In general, dispersion reduces the total FEL power (less beam slices radiate), makes the radiation spectrum narrower, and *chooses* its central wavelength (only the slices with certain energy radiate).

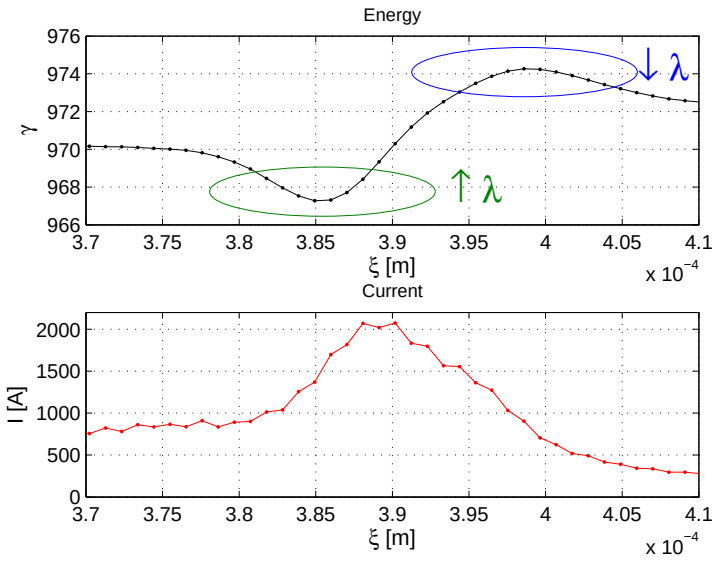

Figure 7.8: Energy and current distribution along the bunch of the electron slices which produce FEL radiation. Electrons with higher energy radiate at shorter wavelengths, while electrons with lower energy produce radiation at longer wavelengths.

As presented later in this chapter, measurements showed that the impact on the spectrum can be different depending on the dispersion sign. The effect of the dispersion depends on the initial transverse coordinates along the bunch. In order to understand this, the results of simulations with an artificial beam under different initial conditions are discussed in the following subsection.

7.4.1 Simulations with a Gaussian Electron Beam

The input beam used in the simulations has the following characteristics:

- Bunch length of 300 µm (RMS).
- Gaussian current profile with a maximum current of 1.5 kA and cut at both sides at 500 A.
- Energy variation with a positive slope of ±1 % along the bunch, with the center of the beam with a design energy of 495 MeV.
- Constant values along the bunch for the rest of the parameters: transverse emittance of 2.0 µrad, slice energy spread of 0.5 MeV (RMS), matched optics corresponding to 495 MeV and 11.5 T/m of gradient for the quadrupoles in the undulator.

The study is restricted to the impact of D_x together with a horizontal offset x. The analysis can be easily generalized to the other transverse coordinates (i.e. D'_x and x', D_y and y, D'_y and y'). Three dispersion scenarios are analyzed: no dispersion and positive and negative linear dispersion of 50 mm. All the shown simulated spectra are averaged over 40 shots. The impact of introducing dispersion is analyzed for different initial horizontal offset distributions along the bunch: initial constant offset along the bunch (zero and non-zero), initial linear correlation between x and *energy*, and initial quadratic correlation between x and *energy*.

Initial Constant Offset along the Bunch

The impact of the dispersion depends on the value of the initial transverse positions. For zero transverse offset (see Figure 7.9) without dispersion the whole beam radiates. Introducing dispersion prevents the lasing of the slices with more energy deviation (head and tail of the bunch) resulting in a narrowing of the wavelength spectrum. Because of the symmetry in this case, the central wavelength does not change after adding the dispersion.

If the initial offset of the beam is non-zero, the final central wavelength depends on the dispersion sign. In the example shown in Figure 7.10 the initial offset is +100 µm. Positive dispersion results in an increase of central wavelength and negative dispersion in its reduction. The total radiation power decreases in both cases.

If the initial offset of the beam is big enough, the introduction of dispersion can increase the FEL power. In the example in Figure 7.11 (in which the initial offset is 250 µm) the initial beam almost does not radiate. The introduction of positive dispersion improves the trajectories for the tail of the bunch (lower energy, longer λ), so that it generates more FEL radiation. Negative dispersion leads to a stronger radiation of the head (higher energy, shorter λ).

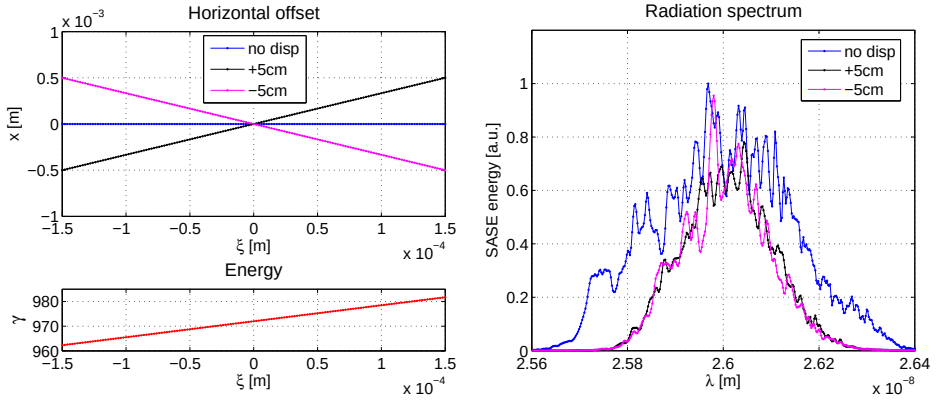

Figure 7.9: Dispersion effects on the wavelength spectrum for an initial zero offset along the bunch.

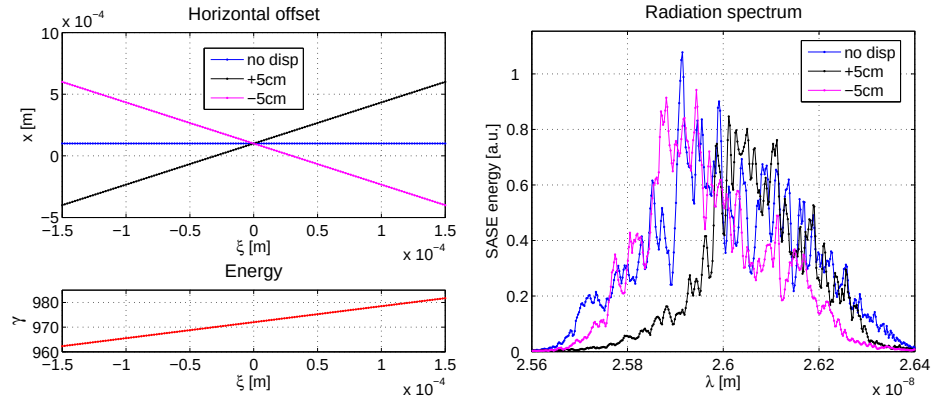

Figure 7.10: Dispersion effects on the wavelength spectrum for an initial offset of 100 µm along the bunch.

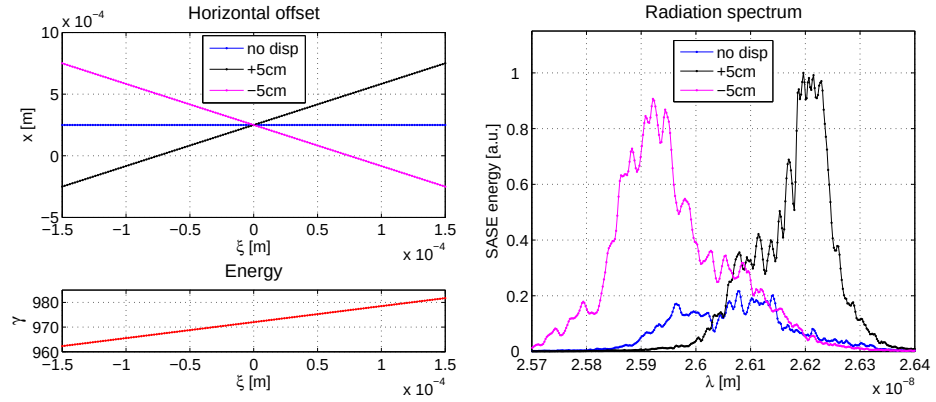

Figure 7.11: Dispersion effects on the wavelength spectrum for an initial offset of 250 µm along the bunch.

Initial Linear *x-energy* Correlation

Assuming that the centroid offset is corrected, the central wavelength is not affected when dispersion is introduced. Positive and negative dispersion will have a different impact depending on the slope of the initial *x-energy* correlation. In the particular example of Figure 7.12, there is a positive initial correlation of 2 cm. The introduction of 5 cm of dispersion adds up to a final value of 7 cm. As a consequence, the head and the tail generate less FEL radiation and the final spectrum becomes narrower.

On the other hand, subtracting 5 cm of dispersion implies that the beam has a final correlation of -3 cm, which slightly decreases the FEL power and narrows the spectrum in comparison to the initial situation. A subtraction of 2 cm exactly counteracts the initial correlation, which results in an increase of the FEL power and in a widening of the wavelength spectrum (not shown in Figure 7.12).

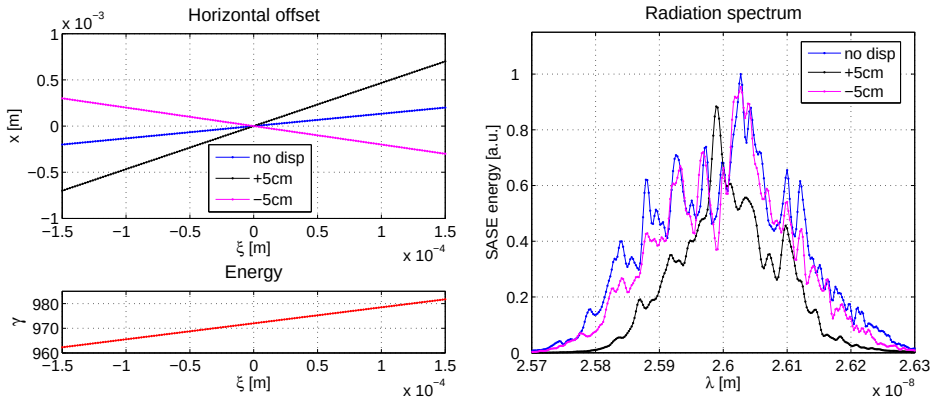

Figure 7.12: Dispersion effects on the wavelength spectrum for an initial linear *x-energy* correlation.

Initial Quadratic *x-energy* Correlation

In a situation with initial quadratic *x-energy* correlation the introduction of additional dispersion narrows the spectrum and changes the central wavelength which gets bigger or smaller depending on the dispersion sign (see Figure 7.13). In this particular example of a negative parabola, positive dispersion decreases the central wavelength, while negative dispersion increases it. Both positive and negative dispersion reduce the radiation power.

Summary

The introduction of (linear) dispersion adds a (linear) correlation between transverse coordinates and energy to the bunch. The effect of the disper-

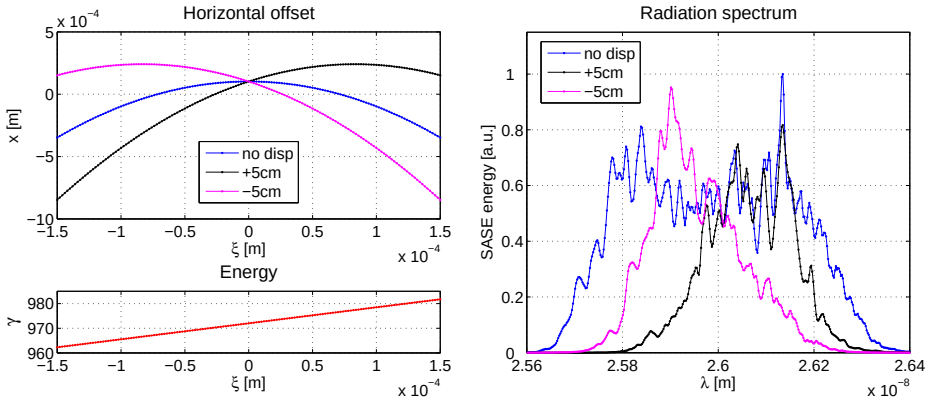

Figure 7.13: Dispersion effects on the wavelength spectrum for an initial quadratic *x-energy* correlation.

sion will be different depending on the initial transverse coordinates of the slices along the bunch. Table 7.2 summarizes the results presented in this subsection.

Table 7.2: Dispersion impact on the wavelength spectrum for different initial transverse offsets.

Initial condition	FEL power and spectrum width	Central wavelength
Zero offset	↓	=
Moderate offset	↓	↑ or ↓ (**)
Big offset	↑	↑ or ↓ (**)
Linear correlation	↑ or ↓ (*)	=
Quadratic correlation	↓	↑ or ↓ (**)
	(*) depending on the final correlation	(**) depending on the dispersion sign

7.4.2 Measurements

The SASE radiation spectrum was measured with the FLASH spectrometer for different horizontal dispersions scenarios. The current of the quadrupoles in the collimator section (Q3/5ECOL) was modified for this purpose. The beam charge was 0.85 nC and the electron energy was 495 MeV. The trajectory was kept constant in all cases, for which small displacements of the quadrupoles were sometimes necessary.

According to simulations done with the measurement optics, a 1 % increase of the Q3/5ECOL current generates the following dispersion functions

at the entrance of the undulator:

$$D_x = -7.48 \text{ mm}$$
$$D'_x = 4.49 \text{ mrad}$$

This is equivalent to a 10 mm RMS dispersion in the undulator section.

Figure 7.14 shows the measured spectra for the different dispersion conditions. Every measurement is the result of averaging the spectrum over 200 shots. The radiation power is maximum when the dispersion is zero (33 µJ measured by the MCP detector). The introduction of dispersion results into a decrease of the FEL power. The central wavelength depends on the sign of the generated dispersion: it becomes longer for an increase of the Q3/5ECOL current and shorter when the current of Q3/5ECOL is reduced. According to the analysis of subsection 7.4.1 a trajectory offset or angle, or a second-order correlation between x (or x') and energy at the undulator entrance is necessary to explain these results.

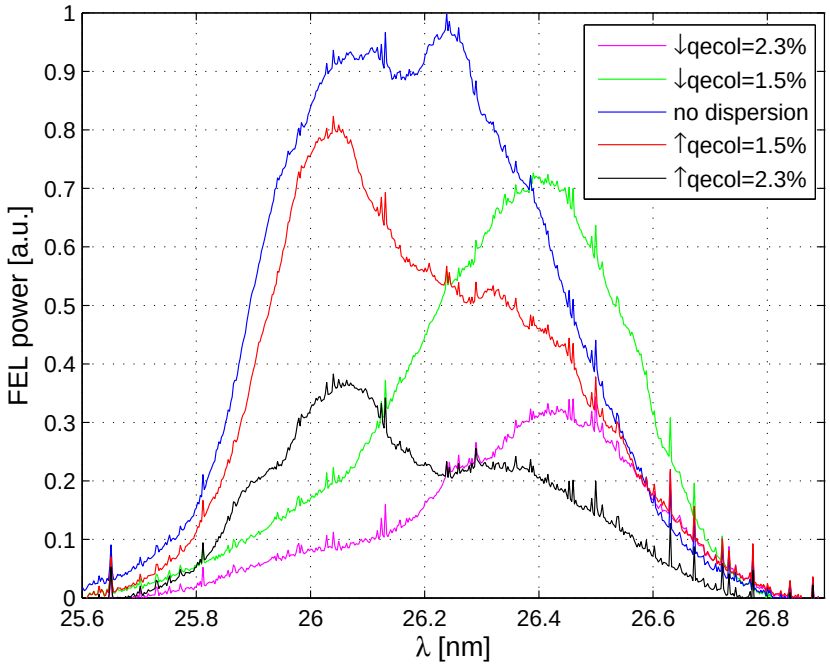

Figure 7.14: Radiation spectrum measurements for different dispersion scenarios. Each spectrum is averaged over 200 shots.

Simulations

The cases without dispersion and with changes of Q3/5ECOL of ±1.5 % were simulated. Electron beam properties obtained at the entrance of the

undulator from start-to-end simulations were used as an input for *Genesis 1.3* (see Figure 7.1). For the different simulation conditions, the trajectory changes due to dispersion were added to the initial coordinates. For each slice i:

$$\begin{aligned} x(i) &= x_0(i) + D_x \cdot \delta(i) \\ x'(i) &= x'_0(i) + D'_x \cdot \delta(i) \end{aligned} \tag{7.1}$$

Optics changes were taken into account, assuming that the beam was perfectly matched in the initial case. Possible electron intensity changes due to the modification of Q3/5ECOL current were not considered.

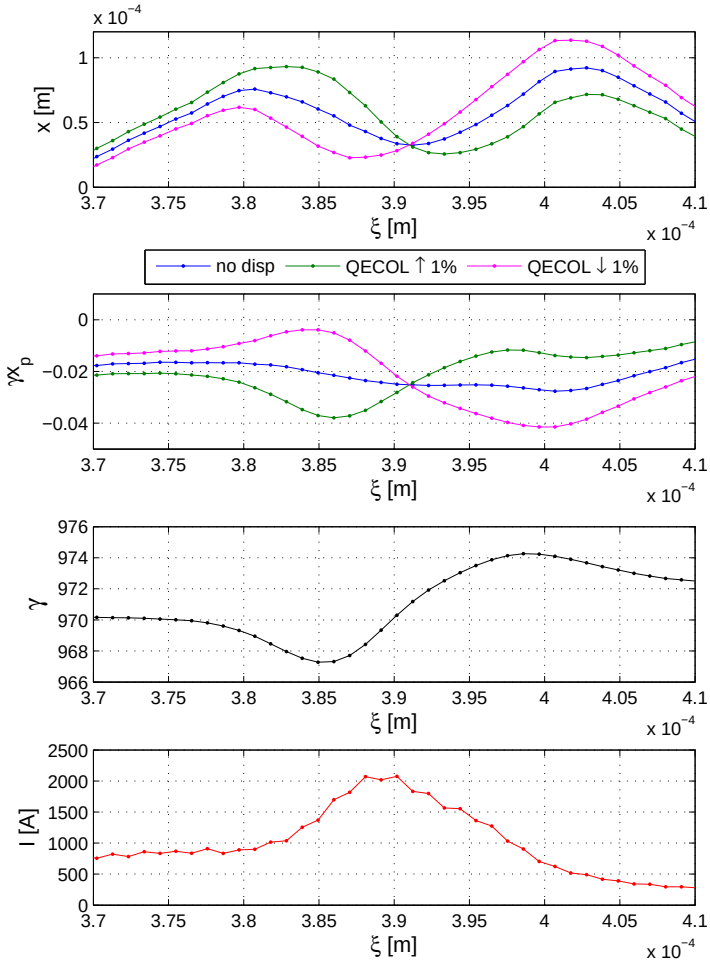

Figure 7.15: Trajectory offset (first plot) and angle (second plot) along the longitudinal position of the bunch for the different dispersion conditions at the entrance of the undulator. The energy and current distribution are also plotted (third and fourth plots).

Figure 7.15 shows the horizontal offset and angle along the bunch with and without dispersion (for ± 1 % of change in the Q3/5ECOL current).

As it can be seen from the figure, the initial horizontal offset is quadratically correlated to the energy between $\xi = 385$ µm and $\xi = 400$ µm. This contributes to explaining (according to Section 7.4.1) why the central wavelength depends on the dispersion sign. In addition, an initial centroid trajectory offset of 50 µm and an angle of -20 µrad at the entrance of the undulator were assumed.

Figure 7.16 shows the simulation results. The simulated spectra are the average results over 100 seeds.

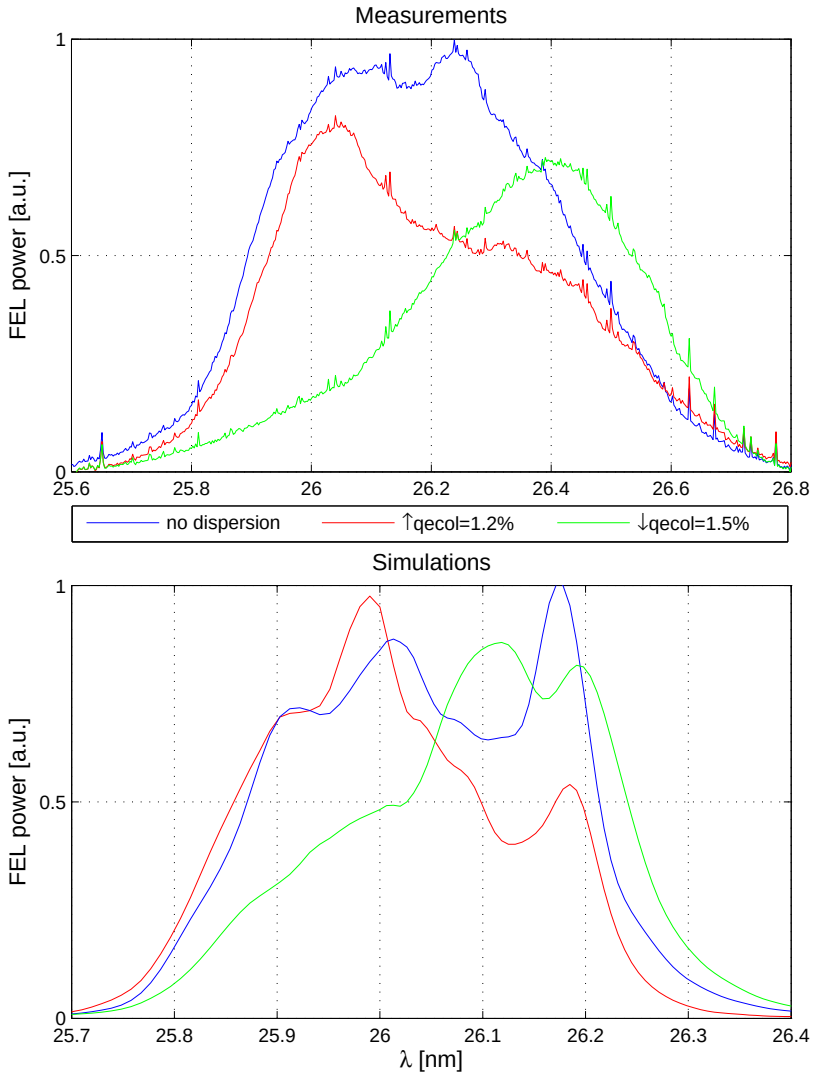

Figure 7.16: Measurements and simulations of dispersion effects to the radiation wavelength spectrum.

A qualitative agreement between measurements and simulations is observed. An increase of the Q3/5ECOL field decreases the FEL power for longer wavelengths and a decrease of the Q3/5ECOL field decreases the radiation intensity for shorter wavelengths. In any case, the introduction of dispersion reduces the total SASE power. The main difference between measurements and simulations is the spectrum width which was bigger during the measurements. This can only be explained if the real electron beam distribution had more energy chirp than the obtained in the start-to-end simulations.

7.5 Conclusion

In this chapter it has been shown that dispersion correction improves the SASE energy sensitivity to the electron beam energy offset. In other words, when dispersion is corrected there is a reduction of the undulator orbit launch sensitivity to the energy jitter. As a consequence, the beam operation is more stable and the tolerances for the RF amplitude and the phase jitter can be more relaxed.

In Section 7.4 it has been proven that dispersion correction allows having a broader radiation spectrum and avoids a reduction of the FEL power due to the off-axis trajectories of the slices with an energy deviation with respect to the nominal one. Thus, removing dispersion is not always desired (e.g. if very small bandwidth is required).

Moreover, it has been shown that dispersion can be used to tune the central wavelength of the FEL spectrum, the shift of which depends on the energy chirp of the electron beam distribution. However, it is advisable to correct all the dispersion and to tune the wavelength by simply modifying the electron energy. This way, lasing will be more stable and the radiation power will be higher.

Chapter 8

Conclusion

In this thesis the concept of dispersion for linacs is discussed, which is essentially different from dispersion in storage rings: in linacs the energy distribution of the particles can considerably change along the lattice, and only the sources downstream of the energy change contribute to the dispersion and therefore can be detected in a measurement.

Spurious dispersion is created by various machine imperfections. Among all the spurious dispersion sources, quadrupole misalignments (equivalent to trajectory offsets) are most important for both FLASH and the XFEL.

Dispersion must be corrected because it produces an increase of the effective electron beam size and emittance, thus degrading the FEL process. Moreover, dispersion needs to be compensated because it causes the off-energy slices of the beam not to produce FEL radiation due to their trajectories offsets. Different errors change the spurious dispersion depending on the actual operating conditions of the accelerator, so dispersion must be measured and controlled frequently.

A method to measure and correct the dispersion has been presented. It consists of measuring the orbit for different energies and correcting simultaneously the orbit and the dispersion using corrector magnets and quadrupole movers. A tool based on this method has been implemented at FLASH. This application is able to correct the dispersion down to 5 mm in both horizontal and vertical planes. This lower limit comes from the BPM jitter and the optics errors. This tool can be potentially used in the future to perform beam-based alignment at FLASH and the XFEL.

Dispersion correction is a key issue for the optimization of the transverse beam quality at the FLASH linac. It has been shown that correcting the dispersion in the injector is necessary to guarantee a good initial transverse beam quality. Moreover, correcting the dispersion along the whole linac is mandatory for ensuring a good beam quality in the FLASH undulator.

By correcting the spurious dispersion inside the undulator region, the SASE power jitter due to electron energy fluctuations is decreased. It has

been proven that the presence of dispersion reduces the FEL power and makes the radiation spectrum narrower because the off-energy slices of the bunch do not radiate. In conclusion, the FEL process is more stable and the output radiation power is higher when the dispersion is corrected. In addition, it has been shown that dispersion can be used to shift the central wavelength of the FEL radiation spectrum.

Appendix A

C-shape at the First Bunch Compressor of FLASH

As introduced in Section 3.2, when the first accelerator module (ACC1) runs at on-crest, the beam can present a *c-shape* in the $x-y$ plane between the second and the third magnet of the first bunch compressor of FLASH (BC2). Since the beam has a longitudinal energy chirp coming from the gun up to ACC1 (see Figure 3.3), a spurious vertical dispersion source between the gun and ACC1 can explain this effect. This will cause the head and the tail being in a different vertical positions between the second and the third magnet of BC2 but at the same horizontal positions - since their energy at this horizontal dispersive position ($D_x \approx -35$ cm) is approximately the same. Figure A.1 shows an example of an electron beam with a c-shape - both measurement and simulation results.

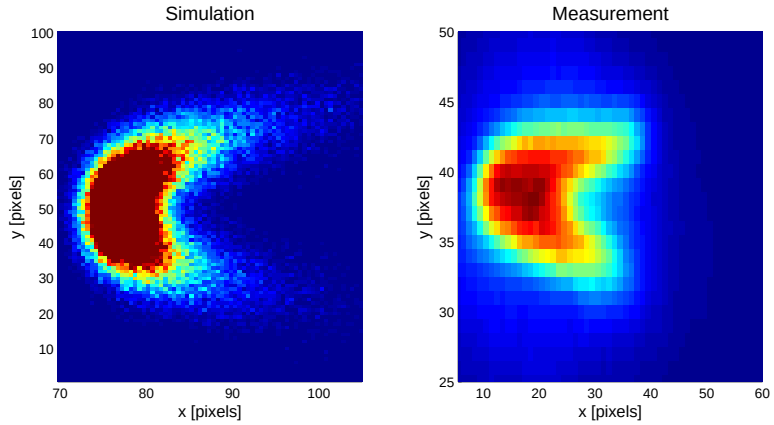

Figure A.1: Simulated (left) and measured (right) c-shaped beam.

Simulations were done from the exit of the gun up to BC2 with *elegant*. A beam distribution obtained with ASTRA for standard parameters has

been used as an input. The dispersion source is generated by a horizontal magnetic field of $3{\cdot}10^{-4}$ Tm (equivalent to a vertical kick of 18 mrad for an energy of 5 MeV) at the exit of the gun section. This initial kick is later compensated by the gun steerers V2GUN and V3GUN. Figure A.2 shows an sketch of the simulations.

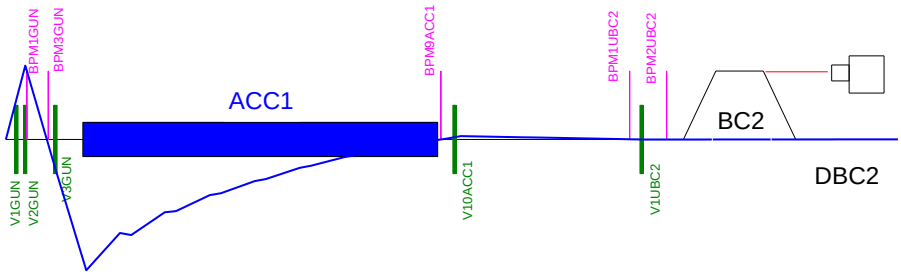

Figure A.2: Sketch of the simulations on the c-shape experiment. An initial vertical kick later corrected by V2/3GUN generates a vertical dispersion which causes the c-shape effect.

Figure A.3 shows simulation results of the generated dispersion from ACC1 (i.e. the dispersion that would be measured changing the ACC1 gradient) and from the gun.

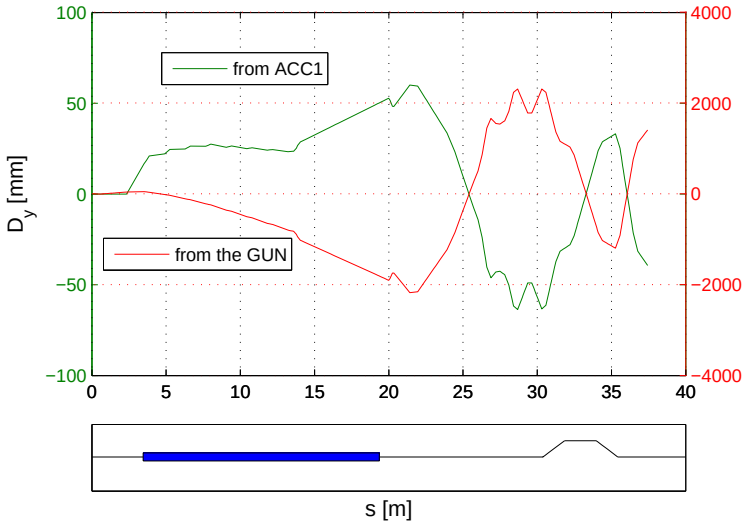

Figure A.3: Simulated dispersion from ACC1 (green, left scale) and from the GUN (red, right scale) for the c-shape experiment.

A.1 Effects of ACC1 phase

When ACC1 runs on-crest, the head and the tail of the bunch have approximately the same energy downstream of the accelerator module. Therefore, between the second and the third magnet of BC2 ($D_x \approx -35$ cm) the head and the tail are approximately in the same horizontal position. If the ACC1 phase is changed, the head will get more (or less) energy than the tail and, as a consequence, the head and the tail will be horizontally separated.

Figure A.4 shows in both measurements and simulations how changing the ACC1 phase moves back and forth the head and the tail in the horizontal direction: increasing the phase moves the head to the right and the tail to the left, while for negative off-crest values the head moves to the left and the tail to the right.

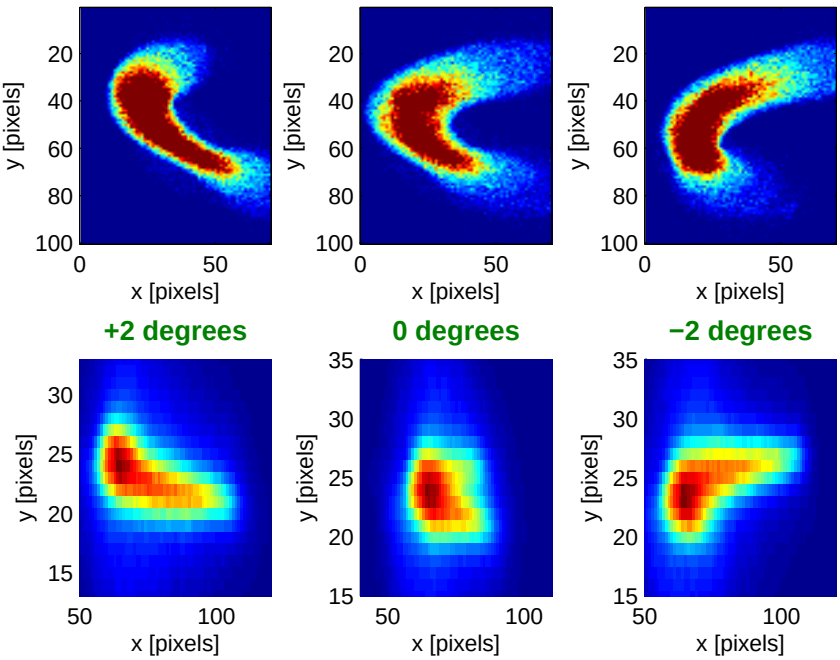

Figure A.4: Simulations (upper plot) and measurements (lower plot) of the c-shape effect for different ACC1 phases. Center: on-crest acceleration; left: +2 degrees off-crest; right: -2 degree off-crest.

A.2 A Possible Explanation: A Horizontal Solenoid Misalignment

If the beam is horizontally misaligned with respect to the solenoid, it will experience mainly a vertical kick, while if the misalignment is in the vertical direction the kick will be in the horizontal plane. Therefore, the required vertical kick to generate the c-shape effect can be produced if the beam travels horizontally off-axis with respect to the solenoid.

In order to prove this hypothesis, the position of the iris and the mirror were changed together. In this way, the beam was misaligned with respect to the gun solenoid. It should be noted that during the measurements it was not possible to move the solenoid for security reasons. As shown in Figure A.5, a movement to the right enhanced the c-shape effect while a movement to the left reduced the effect. In the vertical direction, the c-shape did not change significantly when moving up and down.

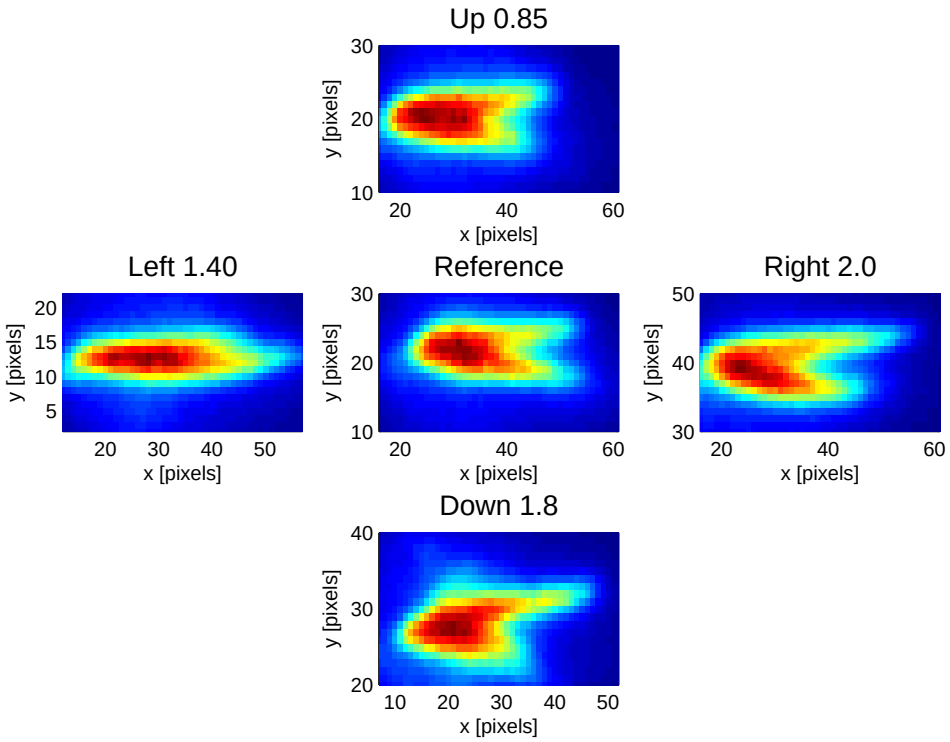

Figure A.5: Measured effects on the c-shape of moving horizontally and vertically both iris and mirror positions (i.e. equivalent to a solenoid misalignment).

As expected, moving the iris and the mirror in the horizontal position had an impact to the trajectory mainly in the vertical direction. Later, another experiment was done: the iris and the mirror positions were set to their original values but the trajectory was corrected with the gun steerers to the one that the beam had when the iris and the mirror were moved. The results are shown in Figure A.6. As it can be seen from the figure, by correcting the vertical trajectory, the c-shape effect can be enhanced (right plot) or mitigated (left plot).

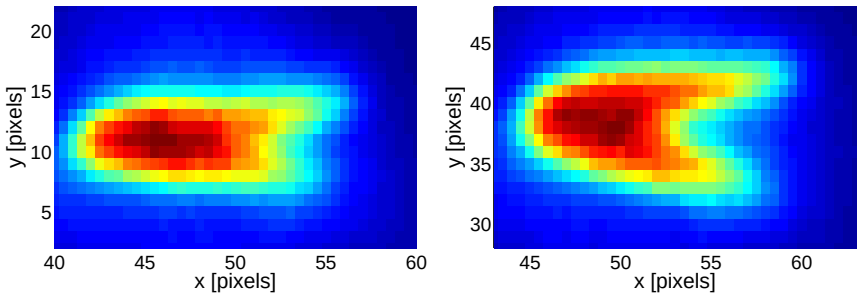

Figure A.6: Measured effects on the c-shape of manipulating the vertical trajectory.

A.3 Conclusion

It has been shown in simulations that the c-shape effect can be generated by a vertical dispersion source upstream of the ACC1 module. The required kick to generate the dispersion can be produced by a horizontal offset between the electron beam and the solenoid. Measurements in which the iris and the mirror were moved and others in which the vertical trajectory was corrected go in favor of these hypotheses.

Appendix B

Second-Order Dispersion Terms for a Dipole Magnet

The non-zero second-order dispersion terms for a pure dipole sector magnet can be obtained as follows:

$$
\begin{aligned}
T_{116} &= 2\frac{1}{\rho^2}I_{11} - 2\frac{1}{\rho^3}I_{116} - \frac{1}{\rho^4}I_{122} \\
T_{126} &= 2\frac{1}{\rho^2}I_{12} - 2\frac{1}{\rho^3}I_{126} + \frac{1}{\rho^2}I_{112} \\
T_{166} &= -\frac{1}{\rho}I_{10} + 2\frac{1}{\rho^2}I_{16} - \frac{1}{\rho^3}I_{166} + \frac{1}{2}\frac{1}{\rho^3}I_{122} \\
T_{216} &= 2\frac{1}{\rho^2}I_{21} - 2\frac{1}{\rho^3}I_{216} - \frac{1}{\rho^4}I_{222} - \frac{1}{\rho}(R_{11}R_{26} + R_{21}R_{16}) \\
T_{226} &= 2\frac{1}{\rho^2}I_{22} - 2\frac{1}{\rho^3}I_{226} + \frac{1}{\rho^2}I_{212} - \frac{1}{\rho}(R_{12}R_{26} + R_{22}R_{16}) \\
T_{266} &= -\frac{1}{\rho}I_{20} + 2\frac{1}{\rho^2}I_{26} - \frac{1}{\rho^3}I_{266} + \frac{1}{2}\frac{1}{\rho^3}I_{222} - \frac{1}{\rho}R_{16}R_{26}
\end{aligned}
\tag{B.1}
$$

The expressions for the key field integrals I_{ij} and I_{ijk} corresponding to

a horizontal bending magnet are:

$$
\begin{aligned}
I_{10} &= \rho R_{16} \\
I_{11} &= \frac{1}{2} l R_{12} \\
I_{12} &= \frac{\rho^2}{2}(R_{12} - l R_{11}) \\
I_{16} &= \rho(\rho R_{16} - \frac{l}{2} R_{12}) \\
I_{112} &= \frac{\rho}{3} R_{12} R_{16} \\
I_{116} &= \rho\left[\frac{l}{2} R_{12} - \frac{1}{3}(R_{12}^2 + \rho R_{16})\right] \\
I_{122} &= \frac{\rho^2}{3}(2\rho R_{16} - R_{12}^2) \\
I_{126} &= \rho\left[\frac{\rho^2}{2}(R_{12} - l R_{11}) - \frac{1}{3}\rho R_{12} R_{16}\right] \\
I_{166} &= \rho^2\left[\frac{4}{3}\rho R_{16} + \frac{1}{3} R_{12}^2 - l R_{12}\right] \\
I_{20} &= R_{12} \\
I_{21} &= \frac{1}{2}(R_{12} - l R_{11}) \\
I_{22} &= I_{11} \\
I_{26} &= \frac{\rho}{2}(R_{12} - l R_{11}) \\
I_{212} &= \frac{1}{3}(2R_{12}^2 - \rho R16) \\
I_{216} &= \rho\left[\frac{l}{2} R_{11} + \frac{1}{6} R_{12} - \frac{2}{3} R_{11} R_{12}\right] \\
I_{222} &= \frac{2}{3}\rho R_{12} R_{16} \\
I_{226} &= \rho\left[\frac{l}{2} R_{12} - \frac{2}{3} R_{12}^2 + \frac{1}{3}\rho R_{16}\right] \\
I_{266} &= \rho^2\left[\frac{1}{3} R_{12} + \frac{2}{3} R_{12} R_{11} - l R_{11}\right]
\end{aligned}
\tag{B.2}
$$

where R_{16} and R_{26} can be obtained using the equation 4.2 and:

$$
\begin{aligned}
R_{11} &= \cos(l/\rho) \\
R_{12} &= \frac{1}{\rho}\sin(1/\rho)
\end{aligned}
\tag{B.3}
$$

It should be noted that the equations from this appendix have been adapted from the expressions of a general ideal magnet [Bro82] to a pure dipole magnet.

Appendix C

Orbit and Dispersion Tool at FLASH

The *Orbit and dispersion tool* is a Matlab [MAT] application used to measure and correct both the orbit and the dispersion at FLASH. It is based on the procedure described in Chapter 5. The response matrices (which are required for the correction algorithm) are calculated using the machine model obtained from the *Optics Toolbox* [OPT], which contains at the current time the most accurate optics model and the transfer coefficients between power supply currents and steerer deflection angles.

The *Orbit and dispersion tool* was developed during the first half of 2006 and first released in August 2006. Last version 3.0 was released in June 2008. Figure C.1 shows the main GUI (Graphical User Interface) of the application.

C.1 User Interface

This section presents the interface between the user and the application in terms of input data, action buttons, output results, and other available options.

C.1.1 Input Data

First of all, the user is asked to provide the initial values of the electron energy after the gun (the default value is 5 MeV) and of the off-crest phases (the default values are zero degrees off-crest for all the accelerator modules). These values are required to obtain the energy profile and the optics along the accelerator, which are used to obtain the response matrices.

The rest of the input data can be defined in the main GUI and under the menu *Input Options*.

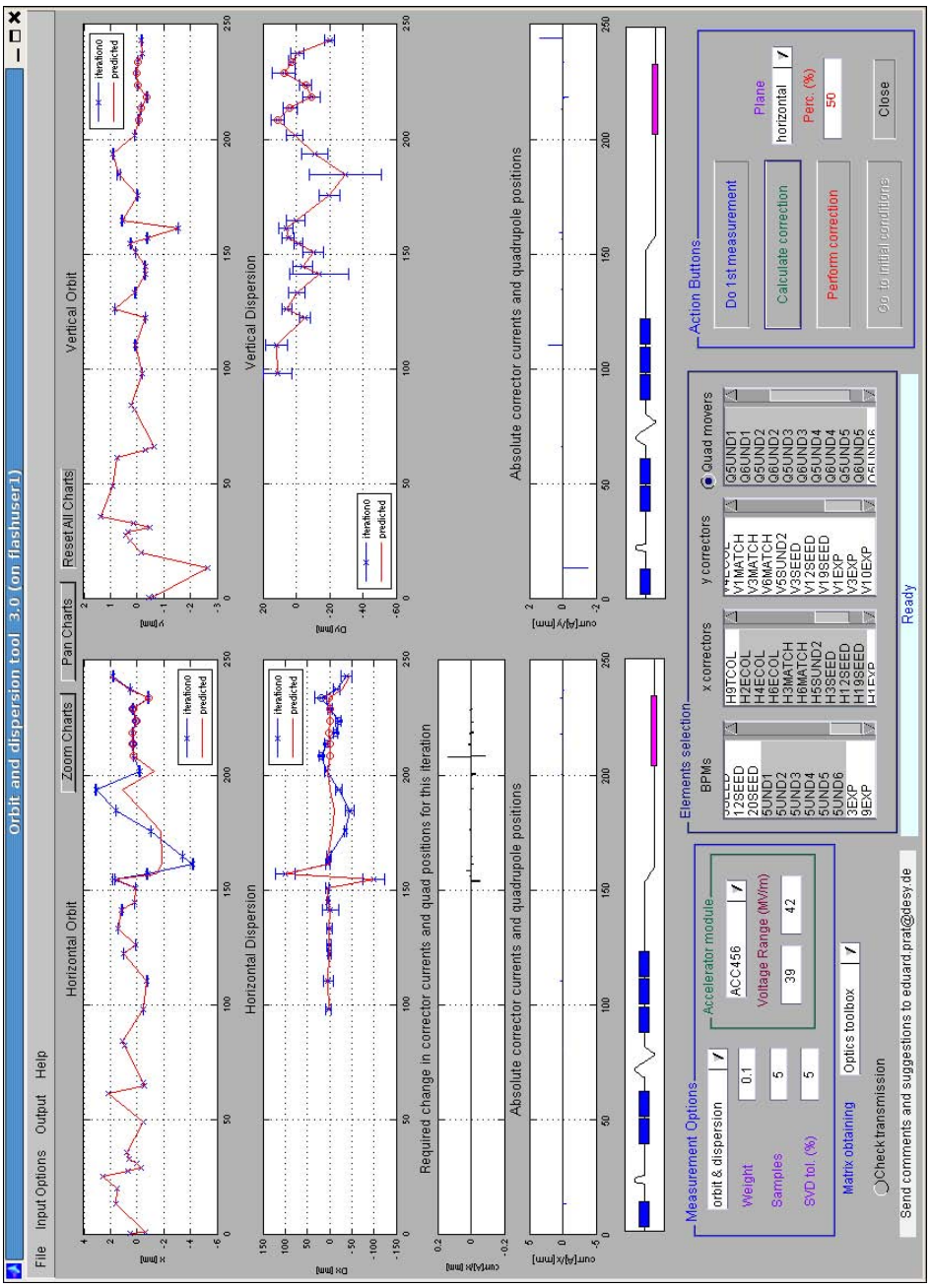

Figure C.1: Main GUI of the *Orbit and dispersion tool*. The plots show from the top to the bottom: trajectory, dispersion, change in steerer currents and quadrupole positions required for a correction, and absolute value of corrector currents and quadrupole positions. Left plots correspond to the horizontal plane and right plots to the vertical one. All the plots are as a function of the longitudinal position of the accelerator s. The lower part of the GUI is used to define the input data and to perform the tool actions.

Input Data in the Main GUI

The fields for the input data are mainly located in the left and center of bottom of the GUI (see Figure C.1).

- **Type of measurement**. There are two options: *only orbit* and *orbit & dispersion*.
- **Weighting factor**. The weighting factor goes from 0 to 1 and defines the relative weight for orbit and dispersion correction (0 corresponds to only orbit correction, 1 corresponds to only dispersion correction). The default value is 0.1.
- **Samples**. This parameter defines the number of BPM readings per each orbit measurement (the default value is 20 samples).
- **SVD tolerance** (%). This parameter is used to determine the number of eigenvalues taken for the SVD algorithm when the correction is calculated. The recommended (and default) value is 5 %. Less SVD tolerance allows for more corrector changes to improve the final resulting orbit and dispersion.
- **Accelerator module**. The user defines here the accelerator module from which the energy will be changed and the gradient limits in MV/m.
- **Matrix obtaining**. The user can choose to use the response matrices from the real machine parameters (default) or from the design optics.
- **Elements selection**. The user has to define which correctors (and quadrupole movers) will be used for the correction as well as the BPMs where the correction will be done.
- **Plane**. It defines the dimension in which the correction is applied - horizontal or vertical.

Input Data Under *Input Options*

For each of the different options, a new GUI pops up.

- **Golden orbit and dispersion** (see Figure C.2). For each BPM, the desired orbit and dispersion can be specified for both horizontal and vertical planes. Zero orbit and design dispersion are defined by default. There is the option to define as the golden orbit the same trajectory that has just been measured. The user has also the option to load and define as the golden orbit a trajectory which has been previously saved with this tool. Finally, it is possible to load and define as the golden orbit a trajectory which has been automatically saved when the

main parameters have been saved and printed to the FLASH logbook [TTF08].

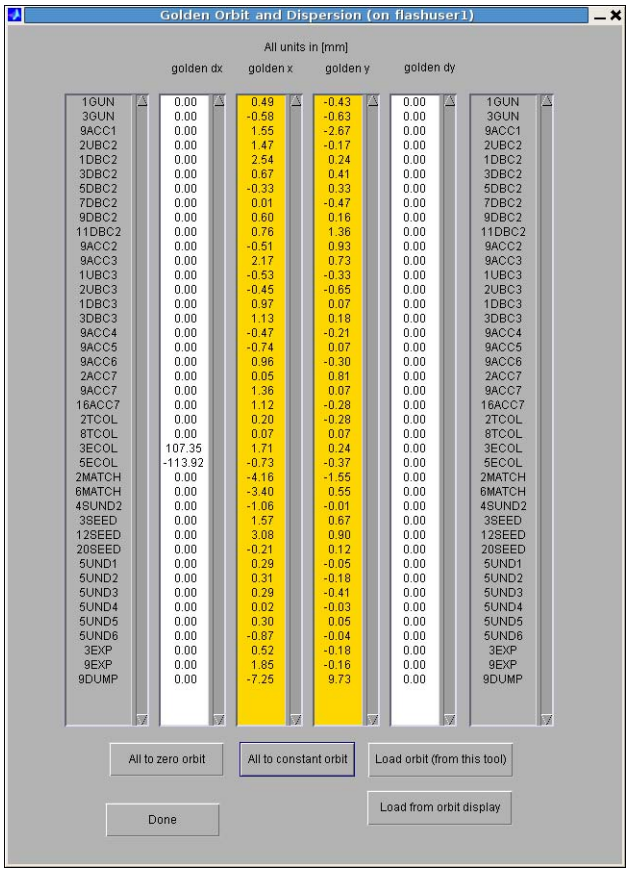

Figure C.2: *Golden orbit and dispersion* GUI of the *Orbit and dispersion tool*.

- **RF settings** (see Figure C.3). The user can define in this GUI the accelerator module from which the energy is changed and how many steps will be done for the dispersion measurement (#steps +1 = #orbits). In addition, the user chooses whether RF steering correction will be done. By default, three steps are used for dispersion measurement and no RF steering correction is performed.

  If RF steering correction is selected, the two closest steerers downstream of the module are chosen by default to perform the compensation in two downstream BPMs. However, the user can select any steerers and BPMs to apply the RF steering correction. The user also selects the correction percentage that is applied per each iteration (the default value is 85 %), and the maximum number of correction iterations (four iterations are defined by default).

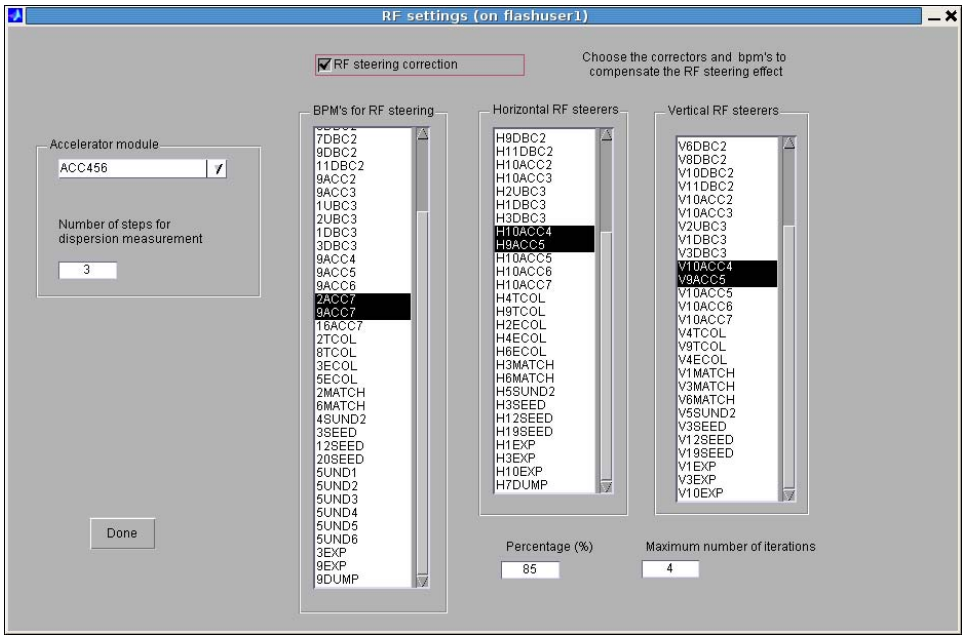

Figure C.3: *RF settings* GUI of the *Orbit and dispersion tool*.

- **Weighting factor details**. This option allows defining a specific weighting factor for each of the BPMs along the machine.

C.1.2 Action Buttons

The action buttons are used to perform the measurements and to calculate and apply corrections. They are located in the bottom-right part of the main GUI of the tool (see Figure C.1).

1. **Do 1st Measurement**. To perform an initial measurement.

2. **Calculate Correction**. The program finds a setting of correctors to make the best possible compensation based on the elements selection, the measured and golden orbit and dispersion, and the SVD tolerance. The prediction for the orbit and dispersion as well as the required corrector strength for the iteration are shown. Neither the steerer currents nor the quadrupole positions are changed with this action.

3. **Do Correction**. The correction calculated by the *Calculate Correction* action button is applied. Next to this button, the user can define the correction percentage that will be applied. The recommended and default value for this parameter is 50 %. After setting the new currents for the steerers (and the new positions for the quadrupoles), a new measurement will be performed and displayed in the main GUI.

4. **Go to initial conditions**. The initial steerer currents and quadrupole positions will be set back. This option is useful in general if the correction is not successful - and particularly when after a correction there is significant loss of the electron beam.

5. **Close**. To close the application.

C.1.3 Output Results

Some of the output results can be seen in the main GUI (see Figure C.1) and some of them can be seen under the menu *Output*.

Output Data in the Main GUI

The orbit and the dispersion along the accelerator for the different correction iterations are displayed in the four top plots of the GUI (the first pair for the orbit and the second pair for the dispersion). The left plots correspond to the horizontal plane and the right ones to the vertical one. When a correction is calculated, the predictions for the orbit and the dispersion are also shown.

Present corrector strengths and quadrupole positions are shown in the bottom plots. Finally, when a correction is calculated the required changes in steerer strengths and quadrupole positions are also displayed.

Output Menu

- **Plot goodness**. It opens a new figure with the peak and RMS of the trajectory, the dispersion and the combined function for the different iterations.

- **BPM details** (see Figure C.4). In the case of a dispersion measurement, this option allows seeing the orbit as a function of the energy for a single BPM.

C.1.4 Other Available Options

- **File → Print orbit (and dispersion)**. Creates figures which show the orbit and the dispersion for the different iterations and for both planes.

- **File → Save data**. To save all the data for the present measurement - starting when the *Do 1st measurement* action button is pressed. It should be noted that no data is saved if the user does not request it.

- **File → Save current orbit**. This options saves the current trajectory. It is useful to set the future golden orbit to the present one (from the *Golden Orbit and Dispersion* GUI).

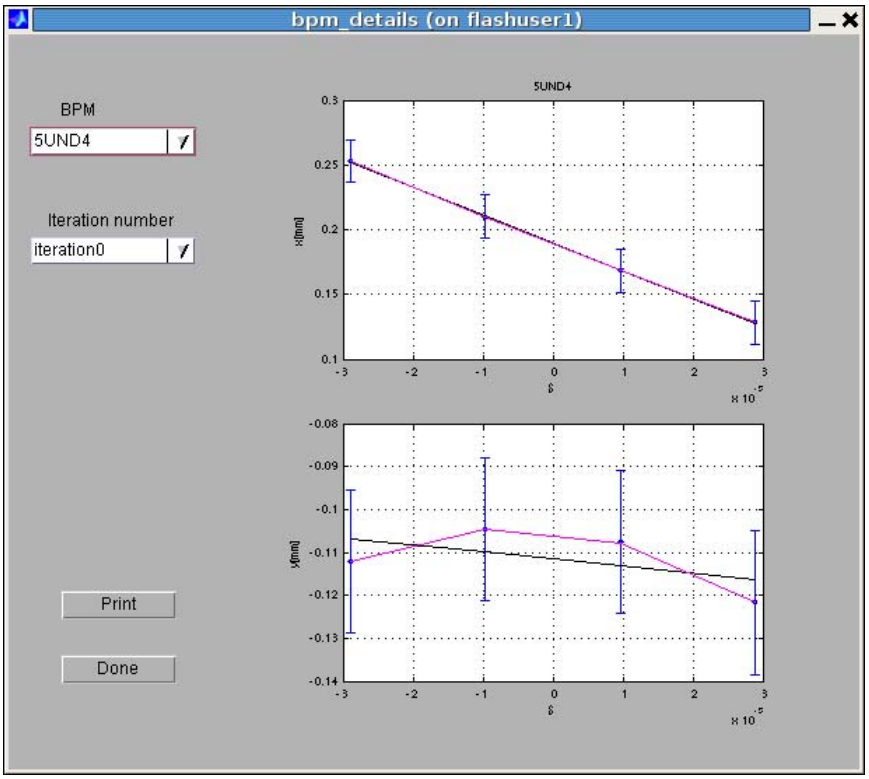

Figure C.4: *BPM details* GUI of the *Orbit and dispersion tool*.

- **File → Save Model**. With this option, the information of the optics model is saved in a file, which can be useful for performing off-line analysis.
- **Help → Orbit and dispersion tool manual**. To access the manual of the application.

C.2 ODCA

The *Orbit and Dispersion Correction Application* (ODCA) is a Java application based on the *Orbit and dispersion tool*. The ODCA is meant to improve the former tool in terms of robustness, responsiveness, flexibility, and production quality, so that it can be used on a regular (daily) basis by the operators in the FLASH control room. It is presently being developed by COSYLAB [1] and the FLASH control group. It is expected to be available for the FLASH operators by the end of 2009.

The ODCA relies on the FLASH optics server, which provides not only the response matrices required for correction algorithms but also the most

[1] Laboratorij za kontrolne sisteme, D. D., Ljubljana, Slovenia

recent information on the currently available number and locations of corrector magnets and beam position monitors. The optics server in its turn is always compiled from the last version of the online Matlab optics toolbox [OPT].

Figure C.5 shows the GUI for the present version of the ODCA. The main application area contains the chart region on its upper half. The data for the different orbits is visualized in the upper plot. The lower plot shows the corrector values and the different changes applied during the corrections. All the displayed elements can be selected or deselected for the correction by clicking on the charts or on the synoptics chart placed below the plot area. Below the charts, all the plotted data is also displayed in tabbed tables. The GUI control part supplied optionally by the modules is also displayed here. The main application controls are displayed below the tables. Beside the main area, the application contains a menu bar where the other application functions can be found. This includes local saving and loading of orbit data, customization of GUI display, configuration of other non-visual application parameters, etc. Finally, at the bottom of the GUI there is a status bar where the local application log and error histories can be accessed.

More information about the ODCA and its first successful tests can be found in [Pra08a].

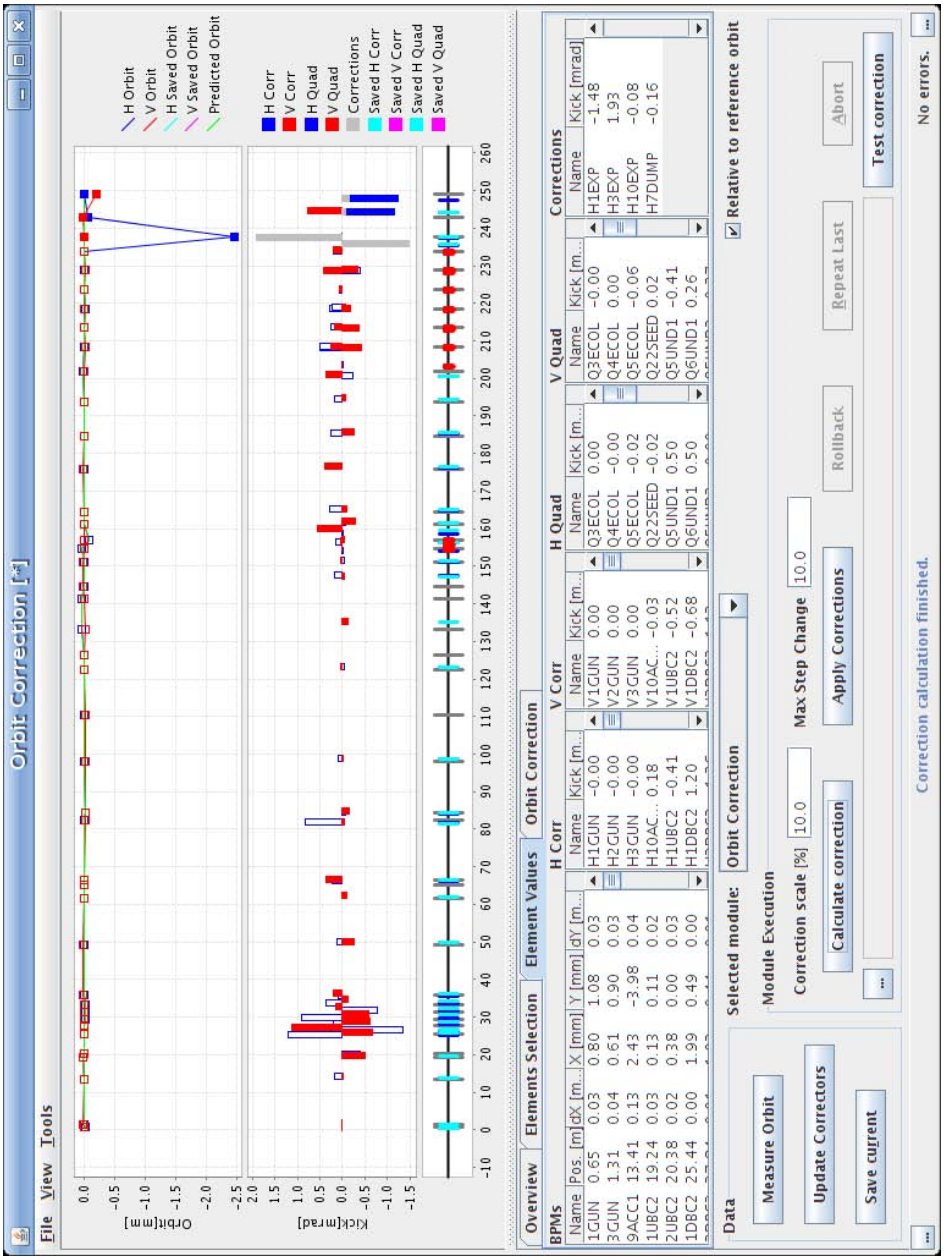

Figure C.5: ODCA GUI.

Bibliography

[Ack07] W. Ackermann et al., "Operation of a free-electron laser from the extreme ultraviolet to the water window." *Nature Photonics* 1, 336–342, 2007.

[Agh07] A. Aghababyan et al., *The European X-Ray Free-Electron Laser Technical Design Report*. Report DESY 2006-097, DESY, Hamburg, Germany, 2007.

[Art02] J. Arthur et al., *Linac Coherent Light Source (LCLS) Conceptual Design Report*. SLAC-R-593, SLAC, Menlo Park, USA, 2002.

[AST] K. Flötmann, *ASTRA - A Space Charge Tracking Algorithm*. DESY, Hamburg, Germany.

[Avy02] V. Ayzazyan et al., "Generation of GW Radiation Pulses from a VUV Free-Electron Laser Operating in the Femtosecond Regime." *Physical Review Letters* 88(10), 104 802/1–104 802/4, 2002.

[Ayv06] V. Ayvazyan et al., "First operation of a free-electron laser generating GW power radiation at 32 nm wavelength." *The European Physical Journal D* 37, 297–303, 2006.

[Bab06] N. Baboi et al., "Resolution Studies at Beam Position Monitors at the FLASH Facility at DESY." *12th Beam Instrumentation Workshop*, Batavia, USA, 2006. Also published in the Proceedings of AIP Conference 2006.

[Bab07] N. Baboi et al., "Beam Position Monitor Calibration at the FLASH Linac at DESY." *Proceedings of PAC'07*, Albuquerque, New Mexico, USA.

[Bab09] N. Baboi. Personal communication.

[Bab09a] N. Baboi. Personal communication.

[Bal03] V. Balandin et al., *Studies of the collimator system for the TTF phase2*. Report TESLA 2003-17, DESY, Hamburg, Germany, 2003.

[Bal05] V.Balandin and N.Golubeva, "Commissioning 445-MeV optics for the TTF2 linac: Dispersion suppression in the Dogleg of the TTF2 collimator section.", 2005. DESY internal document.

[Bal07] V. Balandin. Personal communication.

[Ban87] K. Bane and M. Sands, *Wakefields of very short bunches in an accelerating cavity.* SLAC-PUB-4441, SLAC, Menlo Park, USA, 1987.

[Beu07] B. Beutner, *Measurement and Analysis of Coherent Synchrotron Radiation Effects at FLASH.* Ph.D. thesis, University of Hamburg, 2007.

[Bit07] L. Bittner et al., "MCP-based Photon Detector with Extended Wavelength Range for FLASH." *Proceedings of FEL'07*, Novosibirsk, Russia, 2007.

[Bon84] R. Bonifacio, C. Pellegrini, and L. M. Narducci, "Collective instabilities and high-gain regime free electron laser." *Optics Communications* 50(6), 373–378, 1984.

[Bro82] K. L. Brown, *A First- and Second-Order Matrix Theory for the Design of Beam Transport Systems and Charged Particle Spectrometers.* SLAC Report-75, SLAC, Menlo Park, USA, 1982.

[Byt04] A. Bytchkov et al., "Development of MCP-based photon diagnostics at the TESLA Test Facility at DESY." *Nuclear Instruments and Methods in Physics Research Section A* 528, 254–257, 2004.

[Cas07] P. Castro, E. Prat, and M. Sachwitz. Unpublished Measurement Data.

[Cas98] P. Castro, "Orbit Correction by Dispersion Minimization in an Undulator with Superimposed FODO Lattice." *Proceedings of EPAC'98*, Stockholm, Sweden, 1998.

[Cat05] L. Catani et al., "A large distributed digital camera system for accelerator beam diagnostics." *The Review of Scientific Instruments* 76, 073 303/1–073 303/6, 2005.

[Cha99] A. W. Chao and M. Tigner (eds.), *Handbook of Accelerator Physics and Engineering.* World Scientific, 1999.

[Clo78] E. Close et al., *A Proposed Orbit and Vertical Dispersion Correction System for PEP.* PEP Note 271, SLAC, Menlo Park, USA, 1978.

[Cor93] W. Corbett, M. Lee, and V. Ziemann, *A fast model calibration procedure for storage rings.* SLAC-PUB-6111, SLAC, Menlo Park, USA, 1993.

[CSR] M. Dohlus and T. Limberg, *CSRtrack Version 1.2 Users Manual.* DESY, Hamburg, Germany.

[Doh08] M. Dohlus, J. Rossbach, and P. Schmüser, *Ultraviolet and soft X-ray free-electron lasers.* Springer, 2008.

[Doh08a] M. Dohlus et al., "Coupler Kick for Very Short Bunches and its Compensation." *Proceedings of EPAC'08*, Genoa, Italy, 2008.

[Doh09] M. Dohlus. Personal communication.

[ELE] M. Borland, "elegant : A fexible SDDS-Compilant Code for Accelerator Simulation." APS LS-287, September 2000.

[Emm07] P. Emma et al., "Measurements of Compression and Emittance Growth after the First LCLS Bunch Compressor Chicane." *Proceedings of PAC'07*, Albuquerque, USA, 2007.

[Fre05] H. Freund et al., "Comparative Design Studies for the BESSY FEL Program using the MEDUSA and GENESIS Simulation Codes." *Proceedings of FEL'05*, Stanford, USA, 2005.

[GEN] S. Reiche, *GENESIS 1.3 User Manual*, 2004.

[Ger07] C. Gerth, "Synchrotron Radiation Monitor for Energy Spectrum Measurements in the Bunch Compressor at FLASH." *Proceedings of DIPAC'07*, Venice, Italy, 2007.

[Gol07] K. Goldammer, *Studies of Harmonic Generation in Free Electron Lasers.* Ph.D. thesis, University of Berlin, 2007.

[Hah08] U. Hahn et al., "Wire scanner system for FLASH at DESY." *Nuclear Instruments and Methods in Physics Research Section A* 592(3), 189–196, 2008.

[Hof02] G. H. Hoffstaetter and J. Keil, "Orbit-Response Matrix Analysis at HERA." *Proceedings of EPAC'02*, Paris, France, 2002.

[Hon03] K. Honkavaara et al., "Design of OTR Beam Profile Monitors for the TESLA Test Facility, Phase 2 (TTF2)." *Proceedings of PAC'03*, Portland, USA, 2003.

[Hua01] Z. Huang et al., "Tapered undulators for SASE FELs." *Nuclear Instruments and Methods in Physics Research Section A* 483, 537541, 2001.

[Hua07] Z. Huang and K.-J. Kim, "Review of x-ray free-electron laser theory." *Physical Review Special Topics - Accelerator and Beams* 10, 034 801/1–034 801/38, 2007.

[Kam09] R. Kammering, "Energy Server Calibration in the Dogleg.", 2009. DESY internal document.

[Kei04] J. Keil and W. Decking, "Dispersion Correction in HERA." *Proceedings of EPAC'04*, Lucerne, Switzerland, 2004.

[Kon81] A. M. Kondratenko and E. L. Saldin, "Generation of coherent radiation by a beam of relativistic electrons in an undulator." *Zhurnal Tecknicheskoi Fiziki* 51, 1633–1642, 1981.

[Lim96] T. Limberg et al., "The bunch compression system at the TESLA test facility FEL." *Nuclear Instruments and Methods in Physics Research Section A* 375, 322–324, 1996.

[Loe05] F. Löhl, *Measurement of the Transverse Emittance at the VUV-FEL*. Master's thesis, University of Hamburg, 2005.

[Loe06] F. Löhl et al., "Measurements of the transverse emittance at the FLASH injector at DESY." *Physical Review Special Topics - Accelerators and Beams* 9, 092 802/1–092 802/6, 2006.

[Lor97] R. Lorenz et al., "First Operating Experiences of Beam Position Monitors in the TESLA Test Facility Linac." *Proceedings of PAC'97*, Vancouver, Canada, 1997.

[Lun07] J. Lund-Nielsen and N. Baboi, "Button Beam Position Monitors for FLASH." *Proceedings of DIPAC'07*, Venice, Italy, 2007.

[MAF] The MAFIA collaboration, *Users Guide MAFIA Version 4.00*. CST AG, Bad Nauheimer Str. 19, 64289 Darmstadt, Germany.

[Mas99] M. Maslov, A. Lokhovitskii, and M. Schmitz, *Design of a Beam Dump for the TTF-FEL Phase II (TTF2) Project*. Report TESLA-FEL 1999-06, DESY, Hamburg, Germany, 1999.

[MAT] "MATLAB, The Language of Technical Computing." The Mathworks Inc., 3 Apple Hill Drive, Natick, MA 01760-2098.

[Min03] M. Minty and F. Zimmermann, *Measurement and control of charged particle beams*. Springer, 2003.

[Nic05] P. Nicolosi et al., "Grazing-incidence spectrometer for the monitoring of the VUV FEL beam at DESY." *Journal of Electron*

Spectroscopy and Related Phenomena 144-147, 1055–1058, 2005. Also published in the SPIE Proceedings, Fourth Generation X-Ray Sources and Optics II, vol. 5534, 2004.

[Noe04] D. Nölle and M. Wendt, "TTF II Beam Monitors for Beam Position, Bunch Charge and Phase Measurements." *Proceedings of LINAC'04*, Lübeck, Germany, 2004.

[OPT] V. Balandin and N. Golubeva, *Matlab Functions for Calculations of the Linear Beam Optics of FLASH Linac, Version 1.4*. DESY, Hamburg, Germany, 2008.

[Pan54] W. K. H. Panofsky and J. A. McIntyre, "Achromatic Beam Translation Systems for Use with Linear Accelerator." *The Review of Scientific Instruments* 25 (3), 287–290, 1954.

[Pfl03] J. Plfüeger et al., "Undulator system for the VUV FEL at the TESLA test facility phase-2." *Nuclear Instruments and Methods in Physics Research Section A* 507, 228–233, 2003.

[Pra08] E. Prat et al., "Impact of Electromagnetic Fields in TESLA RF Modules on Transverse Beam Dynamics." *Proceedings of EPAC'08*, Genoa, Italy, 2008.

[Pra08a] E. Prat et al., "Orbit and Dispersion Tool at FLASH." *Proceedings of EPAC'08*, Genoa, Italy, 2008.

[Pre92] W. H. Press et al., *Numerical Recipes in FORTRAN. The art of Scientific Computing*. 2nd edn., Cambridge University Press, 1992.

[Rau91] T. Raubenheimer and R. Ruth, "A dispersion-free trajectory correction technique for linear colliders." *Nuclear Instruments and Methods in Physics Research Section A* 302(2), 191–208, 1991.

[Rei99] S. Reiche, *Numerical Studies for a Single Pass High Gain Free-Electron Laser*. Ph.D. thesis, University of Hamburg, 1999.

[Ros06] J. Rossbach, "Results from FLASH." *Proceedings of EPAC'06*, Edinburgh, Scotland, 2006.

[Ros92] J. Rossbach and P. Schmüser, "Basic course on accelerator optics." *Proceedings of the 1992 Cern Accelerator School*, Jyväskylä, Finland, 1992.

[Ros93] S. H. J. Rosenzweig and J. Stevens, "RF Focusing Effects and Multi-bunch Beam Breakup in Superconducting Linear Colliders." *Proceedings of PAC'93*, Washington, USA, 1993.

[Ros94] J. Rosenzweig and L. Serafini, "Transverse Particle Motion in Radio-Frequency Linear Accelerators." *Physical Review E* 49(2), 1599–1602, 1994.

[Ros96] J. Rossbach, "A VUV free electron laser at the TESLA test facility at DESY." *Nuclear Instruments and Methods in Physics Research Section A* 375, 269–273, 1996.

[Saf97] J. Safranek, "Experimental determination of storage ring optics using orbit response measurements." *Nuclear Instruments and Methods in Physics Research Section A* 388, 27–36, 1997.

[Sal99] E. L. Saldin, E. A. Schneidmiller, and M. V. Yurkov., *The physics of Free Electron Lasers*. Springer, 1999.

[Sch08] S. Schreiber, B. Faatz, and K. Honkavaara, "Operation of FLASH at 6.5 nm Wavelength." *Proceedings of EPAC'08*, Genoa, Italy, 2008.

[Sim08] C. Simon et al., "Performance of a reentrant cavity beam position monitor." *Physical Review Special Topics - Accelerators and Beams* 11, 082 802/1–082 802/10, 2008.

[Ste04] C. Steier et al., "Orbit Response Matrix Analysis Applied at PEP-II." *Proceedings of EPAC'04*, Lucerne, Switzerland, 2004.

[Stu04] F. Stulle, *A Bunch Compressor for small Emittances and high Peak Currents at the VUV Free-Electron Laser*. Ph.D. thesis, University of Hamburg, 2004.

[TTF02] The TESLA Test Facility FEL team, *SASE FEL at the TESLA Facility, phase 2.* Report TESLA-FEL 2002-01, DESY, Hamburg, Germany, 2002.

[TTF08] "Electronic logbook of the TESLA Test Facility.", 2008. URL https://ttfinfo.desy.de/TTFelog-secure/.

[Wal92] R. P. Walker, "Quantum excitation and equilibrium beam properties." *Proceedings of the 1992 Cern Accelerator School*, Jyväskylä, Finland, 1992.

[Wei03] T. Weiland and I. Zagorodnov, *The short-range transverse wake function for TESLA accelerating structure*. Report TESLA 2003-19, DESY, Hamburg, Germany, 2003.

[Xie95] M. Xie, "Design Optimization for an X-Ray Free Electron Laser Driven by SLAC Linac." *Proceedings of PAC'95*, Dallas, USA, 1995.

[Zag07] I. Zagorodnov and M. Dohlus, "Short Range Wakefields of the Couplers." *Mini-Workshop on Higher Order Mode Measurements in Superconducting Accelerating Cavities*, Hamburg, Germany, 2007.

[Zot98] B. W. Zotter and S. Kheifets, *Impedances and Wakes in High-Energy Particle Accelerators*. World Scientific, 1998.

Acknowledgements

First of all, I would like to thank Jörg Roßbach for giving me the opportunity to prepare my thesis at DESY. I value the helpful criticism and support he provided me with. I thank Shaukat Khan for taking the time out of his busy schedule to review this thesis.

More than anyone else, I have to thank my supervisors Winni Decking and Torsten Limberg. From my arrival at DESY until the writing of these words they were always there to support and help me with my work. My sincere thanks.

Coming back to the origins, I would like to thank Yuri Kubishin for introducing me to the field of accelerator physics. Special thanks go to Joel Le Duff for giving me the opportunity to attend JUAS, and to Montse Pont and Dieter Einfeld for allowing me to gain some experience at ALBA, the *Catalan* synchrotron.

I am indebted to all the members of the *FEL Beam Dynamics Group*. In particular, I want to express my gratitude to Igor Zagorodnov for his suggestions and discussions about wakefields and the program *Genesis 1.3*, to Martin Dohlus for his help in the understanding of the coupler kicks, the FEL theory and the start-to-end simulations at FLASH, and to Vladimir Balandin and Nina Golubeva for their aid concerning optics and matching issues.

I am grateful for the collaboration with Christopher Gerth and Kirsten Hacker during the beam tilt and c-shape experiments. I would like to thank Florian Löhl and Katja Honkavaara for their help in the emittance measurements presented in this thesis. Thanks go to Pedro Castro and Martin Sachwitz for their collaboration in the measurements with the wirescanners in the FLASH undulator.

Thanks go to Siggi Schreiber, Bart Faatz and Katja Honkavaara for their support and all they taught me about FLASH. I thank Nicoleta Baboi for her aid related to the BPMs system at FLASH. I am indebted to the whole FLASH team and to all the operators who were on shift with me during the last years.

Special gratitude goes to Paul Emma and the entire LCLS team for their great hospitality and the chance to gain insight into their work during the commissioning of the LCLS injector.

Furthermore, I am indebted to Lars Fröhlich and Bolko Beutner for letting me keep them from work with those discussions on various physical and non-physical topics.

Very special thanks goes to Winni Decking, Torsten Limberg and Diana Boudinova for reading my manuscript and helping to improve it, both in content and language.

Finally, I would like to thank my family, my friends (from Catalunya and Germany) and Diana for their moral support. This thesis is dedicated to the memory of my father. Gràcies per tot, papa.